

1 LEVERAGING MULTI-MESSENGER ASTROPHYSICS FOR DARK MATTER SEARCHES

By

Daniel Nicholas Salazar-Gallegos

A DISSERTATION

Submitted to  
Michigan State University  
in partial fulfillment of the requirements  
for the degree of

Physics—Doctor of Philosophy  
Computational Mathematics in Science and Engineering—Dual Major

Today

**ABSTRACT**

3 I did Dark Matter with HAWC and IceCube. I also used Graph Neural Networks

<sup>4</sup> Copyright by

<sup>5</sup> DANIEL NICHOLAS SALAZAR-GALLEGOS

<sup>6</sup> Today

## ACKNOWLEDGMENTS

8 I love my friends. Thanks to everyone that helped me figure this out. Amazing thanks to the people  
9 at LANL who supported me. Eames, etc Dinner Parties Jenny and her child Kaydince Kirsten, Pat,  
10 Andrea Family. You're so far but so critical to my formation. Unconditional love. Roommate

## TABLE OF CONTENTS

12	LIST OF TABLES . . . . .	vii
13	LIST OF FIGURES . . . . .	viii
14	LIST OF ABBREVIATIONS . . . . .	xv
15	CHAPTER 1 INTRODUCTION . . . . .	1
16	CHAPTER 2 DARK MATTER IN THE COSMOS . . . . .	2
17	2.1 Introduction . . . . .	2
18	2.2 Dark Matter Basics . . . . .	3
19	2.3 Evidence for Dark Matter . . . . .	4
20	2.4 Searching for Dark Matter: Particle DM . . . . .	11
21	2.5 Sources for Indirect Dark Matter Searches . . . . .	16
22	2.6 Multi-Messenger Dark Matter . . . . .	18
23	CHAPTER 3 HIGH ALTITUDE WATER CHERENKOV (HAWC) OBSERVATORY . . . . .	21
24	3.1 The Detector . . . . .	21
25	3.2 Events Reconstruction and Data Acquisition . . . . .	21
26	3.3 Remote Monitoring . . . . .	21
27	CHAPTER 4 ICECUBE NEUTRINO OBSERVATORY . . . . .	22
28	4.1 The Detector . . . . .	22
29	4.2 Events Reconstruction and Data Acquisition . . . . .	22
30	4.3 Northern Test Site . . . . .	22
31	CHAPTER 5 GLORY DUCK: MULTI-WAVELENGTH SEARCH FOR DARK MATTER ANNIHILATION TOWARDS DWARF SPHEROIDAL GALAXIES . . . . .	23
32	5.1 Introduction . . . . .	23
33	5.2 Dataset and Background . . . . .	25
34	5.3 Analysis . . . . .	26
35	5.4 Likelihood Methods . . . . .	31
36	5.5 HAWC Results . . . . .	37
37	5.6 Glory Duck Combined Results . . . . .	40
38	5.7 HAWC Systematics . . . . .	45
39	5.8 $J$ -factor distributions . . . . .	46
40	5.9 Discussion and Conclusions . . . . .	52
43	CHAPTER 6 MULTITHREADING HAWC ANALYSES FOR DARK MATTER SEARCHES . . . . .	56
44	6.1 Introduction . . . . .	56
45	6.2 Dataset and Background . . . . .	56
46	6.3 Analysis . . . . .	58

48	6.4	Likelihood Methods . . . . .	61
49	6.5	Computational Methods: Multithreading . . . . .	62
50	6.6	Analysis Results . . . . .	68
51	6.7	Systematics . . . . .	73
52	6.8	Conclusion and Discussion . . . . .	73
53	<b>CHAPTER 7</b>	<b>HEAVY DARK MATTER ANNIHILATION SEARCH WITH ICE-</b>	
54		<b>CUBE'S NORTH SKY TRACK DATA</b> . . . . .	75
55	7.1	Introduction . . . . .	75
56	7.2	Dataset and Background . . . . .	76
57	7.3	Analysis . . . . .	77
58	<b>CHAPTER 8</b>	<b>NU DUCK</b> . . . . .	83
59	<b>APPENDIX A</b>	<b>MULTI-EXPERIMENT SUPPLEMENTARY FIGURES</b> . . . . .	84
60	<b>APPENDIX B</b>	<b>MULTITHREADING DARK MATTER ANALYSES SUPPLEMEN-</b>	
61		<b>TARY MATERIAL</b> . . . . .	85
62	B.1	Remaining Spectral Models . . . . .	85
63	B.2	<code>mpu_analysis.py</code> . . . . .	86
64	B.3	Comparison with Glory Duck . . . . .	95
65	<b>APPENDIX C</b>	<b>ICECUBE HEAVY DARK MATTER ANALYSIS SUPPLEMEN-</b>	
66		<b>TARY MATERIAL</b> . . . . .	98
67	C.1	Docker Image for Oscillating Neutrino Spectra . . . . .	98
68	<b>BIBLIOGRAPHY</b> . . . . .		101

## LIST OF TABLES

70	Table 5.1	Summary of the relevant properties of the dSphs used in the present work. Column 1 lists the dSphs. Columns 2 and 3 present their heliocentric distance and galactic coordinates, respectively. Columns 4 and 5 report the $J$ -factors of each source given from the $\mathcal{GS}$ and $\mathcal{B}$ independent studies and their estimated $\pm 1\sigma$ uncertainties. The values $\log_{10} J$ ( $\mathcal{GS}$ set) [45] correspond to the mean $J$ -factor values for a source extension truncated at the outermost observed star. The values $\log_{10} J$ ( $\mathcal{B}$ set) [47] are provided for a source extension at the tidal radius of each dSph. <b>Bolded sources are within HAWC's field of view and provided to the Glory Duck analysis.</b>	31
79	Table 5.2	Summary of dSph observations by each experiment used in this work. A '-' indicates the experiment did not observe the dSph for this study. For Fermi-LAT, the exposure at 1 GeV is given. For HAWC, $ \Delta\theta $ is the absolute difference between the source declination and HAWC latitude. HAWC is more sensitive to sources with smaller $ \Delta\theta $ . For IACTs, we show the zenith angle range, the total exposure, the energy range, the angular radius $\theta$ of the signal or ON region, the ratio of exposures between the background-control (OFF) and signal (ON) regions ( $\tau$ ), and the significance of gamma-ray excess in standard deviations, $\sigma$ .	32
88	Table 6.1	Summary of the relevant properties of the dSphs used in the present work. Column 1 lists the dSphs. Columns 2 and 3 present their heliocentric distance and galactic coordinates, respectively. Column 4 reports the $J$ -factors of each source given from the $\mathcal{LS}$ studies and estimated $\pm 1\sigma$ uncertainties. The values $\log_{10} J$ ( $\mathcal{LS}$ set) [65] correspond to the mean $J$ -factor values for a source extension truncated at $0.5^\circ$ .	62
94	Table 6.2	Timing summaries for analyses for serial and multithreaded processes. $M$ tasks is the number of functional-parallel tasks ran for the computation. $T_{p,c}$ is a single run time in hours:minutes:seconds for runs utilizing $p$ nodes and $c$ threads. Runs are run interactively on the same computer to maximize consistency. Empty entries are indicated with '-'. $(\cdot)$ entries are estimated entries extrapolated from data earlier in the column.	66
100	Table 6.3	Speed up summaries for analyses for serial and multithreaded processes. $M$ tasks is the number of functional-parallel tasks ran for the computation. $S_{p,c}$ is a single speedup comparison for runs utilizing $p$ nodes and $c$ threads. $[\cdot]$ are the estimated speedups calculated from Tab. 6.2, Eq. (6.10), and Eq. (6.5). Empty entries are indicated with '-'.	68
105	Proof I know how to include		

## LIST OF FIGURES

107	Figure 2.1	Rotation curve fit to NGC 6503 from [7]. Dashed line is the contribution 108 from visible matter. Dotted curves are from gas. Dash-dot curves are from 109 dark matter (DM). Solid line is the composite contribution from all matter 110 and DM sources. Data are indicated with bold dots with error bars. Data 111 agree strongly with a matter + DM composite prediction. . . . .	5
112	Figure 2.2	Light from distant galaxy is bent in unique ways depending on the distribution 113 of mass between the galaxy and Earth. Yellow dashed lines indicate where 114 the light would have gone if the matter were not present [8]. . . . .	7
115	Figure 2.3	(left) Optical image of galactic cluster 1E0657-558. (right) X-ray image of the 116 cluster with redder meaning hotter and higher baryon density. (both) Green 117 contours are reconstruction of gravity contours from weak lensing. White 118 rings are the best fit mass maxima at 68.3%, 95.5%, and 99.7% confidence. 119 The matter maxima of the clusters are clearly separated from x-ray maxima. [9]	8
120	Figure 2.4	Plank CMB sky. Sky map features small variations in temperature in primor- 121 dial light. These anisotropies are used to make inferences about the universe's 122 energy budget and developmental history. [10] . . . . .	9
123	Figure 2.5	Observed Cosmic Microwave Background power spectrum as a function of 124 multipole moment from Plank [10]. Blue line is best fit model from $\Lambda$ CDM. 125 Red points and lines are data and error, respectively. . . . .	10
126	Figure 2.6	Predicted power spectra of CMB for different $\Omega_m h^2$ values for fixed baryon 127 density from [11]. (left) Low $\Omega_m h^2$ increases the prominence of first and 128 second peaks. (middle) $\Omega_m h^2$ is most similar to the observed power spectrum. 129 The second and third peaks are similar in height. (right) $\Omega_m h^2$ is large which 130 suppresses the first peak and raises the prominence of the third peak. . . . .	10
131	Figure 2.7	The Standard Model (SM) of particle physics. Figure taken from <a href="http://www.quantumdiaries.org/2014/03/14/the-standard-model-a-beautiful-but-flawed-theory/">http://www.quantumdiaries.org/2014/03/14/the-standard-model-a-beautiful-but-flawed-theory/</a> . . . . .	12
134	Figure 2.8	Simplified Feynman diagram demonstrating with different ways DM can 135 interact with SM particles. The 'X's refer to the DM particles whereas the 136 SM refer to fundamental particles in the SM. The large circle in the center 137 indicates the vertex of interaction and is purposely left vague. The colored 138 arrows refer to different directions of time as well as their respective labels. 139 The arrows indicate the initial and final state of the DM -SM interaction in time.	13

140	Figure 2.9 A single jet event in ATLAS detector from 2017 [16]. Jet momentum was 141 observed to be 1.9 TeV. Missing transverse momentum was observed to be 142 1.9 TeV compared to the initial transverse momentum of the event was 0. 143 Implied MET is traced by a red dashed line in event display. . . . .	14
144	Figure 2.10 More detailed pseudo-Feynman diagram of particle cascade from dark matter 145 annihilation into 2 quarks. The quarks hadronize and down to stable particles 146 like $\gamma$ or the anti-proton ( $p^-$ ). Diagram pulled from ICRC 2021 presentation 147 on DM annihilation search [17]. . . . .	15
148	Figure 2.11 Dark Matter (DM) decay spectrum for $b\bar{b}$ initial state and $\gamma$ final state. Redder 149 spectra are for larger DM masses. Bluer spectra are light DM masses. $x$ is a 150 unitless factor defined as the ratio of the mass of DM, $m_\chi$ , and the final state 151 particle energy $E_\gamma$ . Figure from [19]. . . . .	17
152	Figure 2.12 Different dark matter density profiles compared. Some models produce ex- 153 ceptionally large densities at small r [20]. . . . .	18
154	Figure 2.13 The Milky Way Galaxy in photons ( $\gamma$ ) and neutrinos ( $\nu$ ) [22]. The Galactic 155 center is at $l=0^\circ$ and is the brightest region in all panels. (top) An Optical 156 color image of the Milky Way galaxy seen from Earth. Clouds of gas and dust 157 obscure some light from stars. (2nd down) Integrated flux of $\gamma$ -rays observed 158 by the Fermi-LAT telescope [23]. (middle) Expected neutrino emission 159 that corresponds with Fermi-LAT observations. (2nd up) Expected neutrino 160 emission profile after considering detector systematics of IceCube. (bottom) 161 Observed neutrino emission from region of the galactic plane. Substantial 162 neutrino emission was detected. . . . .	19
163	Figure 2.14 Dark Matter annihilation spectra for different final state particle and standard 164 model annihilation channels [24]. Photons (red), $e^\pm$ (green), $\bar{p}$ (blue), $\nu$ (black). . . . .	20
165	Figure 5.1 Sensitivities of five gamma-ray experiments compared to percentages of the 166 Crab nebula's emission and dark matter annihilation. Solid lines present 167 estimated sensitivities to power law spectra [FACT CHECK THIS] for each 168 experiment. Green lines are Fermi-LAT sensitivities where lighter green is 169 the sensitivity to the galactic center and dark green is its sensitivity to higher 170 declinations. Orange, red, and purple solid lines represent the MAGIC, HESS, 171 and VERITAS 50 hour sensitivities respectively. The maroon and brown lines 172 are the HAWC 1 year and 5 year sensitivities. Across four decades of gamma- 173 ray energy, these experiments have similar sensitivities on the order $10^{-12}$ 174 erg cm $^{-2}$ s $^{-1}$ . The dotted lines are estimated dark matter fluxes assuming 175 $m_\chi = 5$ TeV DM annihilating to bottom quarks (red), tau leptons (blue), 176 and W bosons (green). Faded gray lines outline percentage flux of the Crab 177 nebula. Figure is an augmented version of [25] . . . . .	24

178	Figure 5.2	Effect of Electroweak (EW) corrections on expected DM annihilation spectrum for $\chi\chi \rightarrow W^-W^+$ . Solid lines are spectral models that consider EW corrections. Dash-dot lines are spectral models without EW corrections. Red lines are models for $M_\chi = 1$ TeV. Blue lines represent models for $M_\chi = 100$ TeV. All models are sourced from the PPPC4DMID [44]. . . . .	28
183	Figure 5.3	$\frac{dJ}{d\Omega}$ maps for Segue1 (top) and Coma Berenices (bottom). Origin is centered on the specific dwarf spheroidal galaxies (dSph). X and Y axes are the angular separation from the center of the dwarf. Plots of the remaining 11 dSph HAWC studied are linked in Fig. A.1. . . . .	30
187	Figure 5.4	Illustration of the combination technique showing a comparison between $-2 \ln \lambda$ provided by four instruments (colored lines) from the observation of the same dSph without any $J$ nuisance and their sum, <i>i.e.</i> the resulting combined likelihood (thin black line). According to the test statistics of Equation (5.6), the intersection of the likelihood profiles with the line $-2 \ln \lambda = 2.71$ indicates the 95% C.L. upper limit on $\langle \sigma v \rangle$ . The combined likelihood (thin black line) shows a smaller value of upper limit on $\langle \sigma v \rangle$ than those derived by individual instruments. We also show how the uncertainties on the $J$ factor effects the combined likelihood and degrade the upper limit on $\langle \sigma v \rangle$ (thick black line). All likelihood profiles are normalized so that the global minimum $\widehat{\langle \sigma v \rangle}$ is 0. We note that each profile depends on the observational conditions in which a target object was observed. The sensitivity of a given instrument can be degraded and the upper limits less constraining if the observations are performed in non-optimal conditions such as a high zenith angle or a short exposure time. . . . .	35
202	Figure 5.5	. . . . .	38
203	Figure 5.6	HAWC TS values for best fit $\langle \sigma v \rangle$ versus $m_\chi$ for seven SM annihilation channels with $J$ factors from $\mathcal{GS}$ . The solid black line shows the combined best fit TS values. The colored, dashed lines are the TS values for each of the 13 sources HAWC studied. . . . .	39
207	Figure 5.7	HAWC Brazil bands at 95% confidence level on $\langle \sigma v \rangle$ versus DM mass for seven annihilation channels with $J$ -factors from $\mathcal{GS}$ [53]. The solid line represents the combined limit from 13 dSphs. The dashed line is the expected limit. The green band is the 68% containment. The yellow band is the 95% containment. . . . .	40

212	Figure 5.8	Upper limits at 95% confidence level on $\langle \sigma v \rangle$ in function of the DM mass for 213 eight annihilation channels, using the set of $J$ factors from Ref. [53] ( $\mathcal{GS}$ set 214 in Table 5.1). The black solid line represents the observed combined limit, 215 the black dashed line is the median of the null hypothesis corresponding 216 to the expected limit, while the green and yellow bands show the 68% and 217 95% containment bands. Combined upper limits for each individual detector 218 are also indicated as solid, colored lines. The value of the thermal relic 219 cross-section in function of the DM mass is given as the red dotted-dashed 220 line [54]. . . . .	41
221	Figure 5.9	Same as Fig. 5.8, using the set of $J$ factors from Ref. [47, 55] ( $\mathcal{B}$ set in Table 5.1). . . . .	42
222	Figure 5.10	Comparisons of the combined limits at 95% confidence level for each of the 223 eight annihilation channels when using the $J$ factors from Ref. [53] ( $\mathcal{GS}$ set in 224 Table 5.1), plain lines, and the $J$ factor from Ref. [47, 55] ( $\mathcal{B}$ set in Table 5.1), 225 dashed lines. The cross-section given by the thermal relic is also indicated [54]. . . . .	44
226	Figure 5.11	Comparisons of the combined limits at 95% confidence level for a point source 227 analysis and extended source using [53] $\mathcal{GS}$ J-factor distributions and PPPC 228 [44] annihilation spectra. Shown are the limits for Segue1 which will have 229 the most significant impact on the combined limit. 6 of the 7 DM annihilation 230 channels are shown. Solid lines are extended source studies. Dashed lines 231 are point source studies. Overall, the extended source analysis improves the 232 limit by a factor of 2. . . . .	46
233	Figure 5.12	Same as Fig. 5.11 on Coma Berenices. This dSph also contributes signifi- 234 cantly to the limit. The limits are identical in this case. . . . .	47
235	Figure 5.13	Comparison of combined limits when correcting for HAWC's pointing sys- 236 tematic. All DM annihilation channels are shown. The solid black line is the 237 ratio between published limit to the declination corrected limit. The blue solid 238 line or "Combined_og" represented the limits computed for Glory Duck. The 239 solid orange line or "Combined_ad" represented the limits computed after 240 correcting for the pointing systematic. . . . .	48
241	Figure 5.14	Differential map of $dJ/\Omega$ from model built in Section 5.8.1 and profiles 242 provided directly from authors. (Top) Differential from Segue1. (bottom) 243 Differential from Coma Berenices. Note that their scales are not the same. 244 Segue1 shows the deepest discrepancies which is congruent with its large 245 uncertainties. Both models show anuli where unique models become apparent. . . . .	49

246	Figure 5.15 HAWC limits for Coma Berenices (top) and Segue1 (bottom) for two different 247 map sets. Blue lines are limits calculated on maps with poor model repre- 248 sentation. Orange lines are limits calculated on spatial profiles provided by 249 the authors of [45]. Black line is the ratio of the poor spatial model limits to 250 the corrected spatial models. The left y-axis measures $\langle \sigma v \rangle$ for the blue and 251 orange lines. The right y-axis measures the ratio and is unitless. . . . .	50
252	Figure 5.16 Comparisons between the $J$ -factors versus the angular radius for the com- 253 putation of $J$ factors from Ref. [53] ( $\mathcal{GS}$ set in Table 5.1) in blue and for 254 the computation from Ref. [47, 55] ( $\mathcal{B}$ set in Tab. 5.1) in orange. The solid 255 lines represent the central value of the $J$ -factors while the shaded regions 256 correspond to the $1\sigma$ standard deviation. . . . .	53
257	Figure 5.17 Comparisons between the $J$ -factors versus the angular radius for the computa- 258 tion of $J$ factors from Ref. [53] ( $\mathcal{GS}$ set in Tab. 5.1) in blue and for the 259 computation from Ref. [47, 55] ( $\mathcal{B}$ set in Tab. 5.1) in orange. The solid 260 lines represent the central value of the $J$ -factors while the shaded regions 261 correspond to the $1\sigma$ standard deviation. . . . .	54
262	Figure 6.1 Difference between spectral hypotheses from PPPC [44] and HDM [64]. 263 Shown is the expected DM annihilation spectrum for $\chi\chi \rightarrow W^-W^+$ . Solid 264 lines are spectral models with EW corrections from the PPPC. Dash-dot lines 265 are spectral models from HDM. Red lines are models for $M_\chi = 1$ TeV. Blue 266 lines represent models for $M_\chi = 100$ TeV. . . . .	59
267	Figure 6.2 Photon spectra for $\chi\chi \rightarrow \gamma\gamma$ (left) and $\chi\chi \rightarrow ZZ$ (right) after Gaussian 268 convolution of line features. Both spectra have $\delta$ -features at photon energies 269 equal to the DM mass. Bluer lines are annihilation spectra with lower DM 270 mass. Redder lines are spectra from larger DM mass. All Spectral models are 271 sourced from the Heavy Dark Matter models [64]. Axes are drawn roughly 272 according to the energy sensitivity of HAWC. . . . .	60
273	Figure 6.3 $\frac{dJ}{d\Omega}$ maps for Coma Berenices, Draco, Segue1, and Sextans. Columns are 274 divided for the $\pm 1\sigma$ uncertainties in $dJ/d\Omega$ around the mean value from $\mathcal{LS}$ 275 [65]. Origin is centered on the specific dwarf spheroidal galaxies (dSph). $\theta$ 276 and $\phi$ axes are the angular separation from the center of the dwarf . . . . .	61
277	Figure 6.4 Infographic on how jobs and DM computation was organized in Section 5.3. 278 Jobs were built for each permutation of CHANS and SOURCES shown by the 279 left block in the figure. Each job, which took on the order 2 hrs to compute, 280 had the following work flow: 1. Import HAWC analysis software, 2 min to 281 run. 2. Load HAWC count maps, 5 min to run. 3. Load HAWC energy and 282 spatial resolutions, 4 min. 5. Load DM spatial source templates and spectral 283 models, less than 1 s. 6. Perform likelihood fit on data and model, about 8 284 min per DM mass. 7. Write results to file, less than 1s. . . . .	63

285	Figure 6.5	Graphic of Gustafson parallel coding pattern. $f_s$ is the fraction of a program, in time, spent on serial computation. $f_p$ is the fraction of computing time that is parallelizable. $T_p$ is the total time for a parallel program to run. $T_1$ is the total time for a parallel program to run if only 1 processor is allocated. $P_N$ is the $N$ -th processor where it's row is the computation the processor performs. The Gustafson pattern is most similar to what is implemented for this analysis. Figure is pulled from [67]. . . . .	64
292	Figure 6.6	Task chart for one multithreaded job developed for this project. Green blocks indicate a shared resource across the threads AND computation performed serially. Red blocks indicate functional parallel processing within each thread. 3 threads are represented here, yet many more can be employed during the full analysis. Jobs are defined by the SOURCE as these require unique maps to be loaded into the likelihood estimator. The $m_\chi$ , CHAN, and $\langle\sigma v\rangle$ variables are entered into the thread pool and allocated as evenly as possible across the threads. . . . .	66
300	Figure 6.7	HAWC upper limits at 95% confidence level on $\langle\sigma v\rangle$ versus DM mass for $\chi\chi \rightarrow b\bar{b}, t\bar{t}, u\bar{u}, d\bar{d}, s\bar{s}, c\bar{c}, gg, W^+W^-$ , and $hh$ . Limits are with $\mathcal{LS}$ $J$ - factors [65]. The solid line represents the observed combined limit. Dashed lines represent limits from individual dSphs. . . . .	69
304	Figure 6.8	HAWC upper limits at 95% confidence level on $\langle\sigma v\rangle$ versus DM mass for $\chi\chi \rightarrow \nu_e\bar{\nu}_e, \nu_\mu\bar{\nu}_\mu, \nu_\tau\bar{\nu}_\tau, e\bar{e}, \mu\bar{\mu}, \tau\bar{\tau}, \gamma\gamma$ and $ZZ$ . Limits use $\mathcal{LS}$ $J$ factors [65]. The solid line represents the observed combined limit. Dashed lines represent limits from individual dSphs. . . . .	70
308	Figure 6.9	HAWC TS values for best fit $\langle\sigma v\rangle$ versus $m_\chi$ for SM annihilation channels: $\chi\chi \rightarrow b\bar{b}, t\bar{t}, u\bar{u}, d\bar{d}, s\bar{s}, c\bar{c}, gg, W^+W^-$ , and $hh$ . Limits use $\mathcal{LS}$ $J$ factors. The solid black line shows the combined best fit TS values. The colored, dashed lines are the TS values from each dSph. . . . .	71
312	Figure 6.10	HAWC TS values for best fit $\langle\sigma v\rangle$ versus $m_\chi$ for SM annihilation channels: $\chi\chi \rightarrow \nu_e\bar{\nu}_e, \nu_\mu\bar{\nu}_\mu, \nu_\tau\bar{\nu}_\tau, e\bar{e}, \mu\bar{\mu}, \tau\bar{\tau}, \gamma\gamma$ and $ZZ$ . Limits use $\mathcal{LS}$ $J$ factors. The solid black line shows the combined best fit TS values. The colored, dashed lines are the TS values from each dSph. . . . .	72
316	Figure 6.11	Comparison of HAWC limits from this analysis to Glory Duck (Fig. 5.5) for 3 dSphs and 3 SM annihilation channels: $b\bar{b}, \tau\bar{\tau}$ , and $e\bar{e}$ . Each sector shows the 95% confidence limit from Glory Duck (blue line) and this analysis (orange line) in the top plot. The lower plot features the ratio in log scale of Glory Duck to this analysis in a red solid line. Horizontal dashed lines are for ratios of 1.0 (black) and $\sqrt{2}$ (blue). Ratios larger than 1.0 are for limits smaller, or stricter, than Glory Duck. Ratios larger than $\sqrt{2}$ indicates limits are stricter than a simple doubling of the Glory Duck data. . . . .	74

324	Figure 7.1	Neutrino spectra at production (left panels) and after oscillation at Earth 325 (right panels). Blue, orange, and green lines are the $\nu_e$ , $\nu_\mu$ , and $\nu_\tau$ spectra 326 respectively. Top panels show the spectra in $\frac{dN}{dE}$ . Lower panels plot the flavor 327 ratio to $\nu_e + \nu_\mu + \nu_\tau$ . SM annihilation channels $b\bar{b}$ , $\tau\bar{\tau}$ , and $\nu_\mu\bar{\nu}_\mu$ are shown 328 for $M_\chi = 1$ PeV, TeV, and EeV. . . . .	79
329	Figure 7.2	Signal recovery for 100 TeV DM annihilation into $\nu_\mu\bar{\nu}_\mu$ for a source at Dec 330 = $16.06^\circ$ . $n_{\text{inj}}$ is the number of injected signal events in simulation. $n_s$ is 331 the number of reconstructed signal events from the simulation. Although 332 the uncertainties are small and tight, the reconstructed $n_s$ are systematically 333 underestimated. . . . .	80
334	Figure 7.3	Top left panel shows the two kernels overlayed the original spectrum from 335 Charon. delta I is the difference in the integral of the peaks with respect to the 336 original spectrum. The vertical red line indicated where the original neutrino 337 line is maximized. Lower right shows the signal recovers of the DM model 338 using the Gaussian kernel with parameters enumerated above. . . . .	81
339	Figure A.1	Sister figure to Figure 5.3. Sources in the first row from left to right: Bootes 340 I, Canes Venatici I, II. In second row: Draco, Hercules, Leo I. In the first row: 341 Leo II, Leo IV, Sextans. In the final row: Ursa Major I, Ursa Major II. . . . .	84
342	Figure B.1	Sister figure to Figure 6.2 for remaining SM primary annihilation channels 343 studied for this thesis. These did not require any post generation smoothing 344 and so are directly pulled from [64] with a binning scheme most helpful for a 345 HAWC analysis. . . . .	85
346	Figure B.2	<b>TODO: fill this out</b> . . . . .	95
347	Figure B.3	<b>TODO: fill this out</b> . . . . .	96
348	Figure B.4	<b>TODO: fill this out</b> . . . . .	97

**LIST OF ABBREVIATIONS**

- 350   **MSU**      Michigan State University  
351   **LANL**     Los Alamos National Laboratory  
352   **DM**       Dark Matter  
353   **SM**       Standard Model  
354   **HAWC**    High Altitude Water Cherenkov Observatory  
355   **dSph**     Dwarf Spheroidal Galaxy

356

## **CHAPTER 1**

### **INTRODUCTION**

357 Is the text not rendering right? Ah ok it knows im basically drafting the doc still

## CHAPTER 2

358

### DARK MATTER IN THE COSMOS

359 **2.1 Introduction**

360 The dark matter problem can be summarized in part by the following thought experiment.

361 Let us say you are the teacher for an elementary school classroom. You take them on a field  
362 trip to your local science museum and among the exhibits is one for mass and weight. The exhibit  
363 has a gigantic scale, and you come up with a fun problem for your class.

364 You ask your class, "What is the total weight of the classroom? Give your best estimation to  
365 me in 30 minutes, and then we'll check your guess on the scale. If your guess is within 10% of the  
366 right answer, we will stop for ice cream on the way back."

367 The students are ecstatic to hear this, and they get to work. The solution is some variation of  
368 the following strategy. The students should give each other their weight or best guess if they do  
369 not know. Then, all they must do is add each student's weight and get a grand total for the class.  
370 The measurement on the giant scale should show the true weight of the class. When comparing  
371 the measured weight to your estimation, multiply the measurement by  $1.0 \pm 0.1$  to get the  $\pm 10\%$   
372 tolerances for your estimation.

373 Two of your students, Sandra and Mario, return to you with a solution.

374 They say, "We weren't sure of everyone's weight. We used 65 lbs. for the people we didn't  
375 know and added everyone who does know. There are 30 of us, and we got 2,000 lbs.! That's a ton!"

376 You estimated 1,900 lbs. assuming the average weight of a student in your class was 60 lbs.  
377 So, you are pleased with Sandra's and Mario's answer. You instruct your students to all gather on  
378 the giant scale and read off the weight together. To all your surprise, the scale reads *10,000 lbs.*!  
379 10,000 is significantly more than a 10% error from 2,000. In fact, it is approximately 5 times more  
380 massive than either your or your students' estimates. You think to yourself and conclude there  
381 must be something wrong with the scale. You ask an employee to check the scale and verify it is  
382 well calibrated. They confirm that the scale is in working order. You weigh a couple of students  
383 individually to assess that the scale is well calibrated. Sandra weighs 59 lbs., and Mario weighs

384 62 lbs., typical weights for their age. You then weigh each student individually and see that their  
385 weights individually do not deviate greatly from 60 lbs. So, where does all the extra weight come  
386 from?

387 This thought experiment serves as an analogy to the Dark Matter problem. The important  
388 substitution to make however is to replace the students with stars and the classroom with a galaxy,  
389 say the Milky Way. Individually the mass of stars is well measured and defined with the Sun as our  
390 nearest test case. However, when we set out to measure the mass of a collection of stars as large as  
391 galaxies, our well-motivated estimation is wildly incorrect. There simply is no way to account for  
392 this discrepancy except without some unseen, or dark, contribution to mass and matter in galaxies.  
393 I set out in my thesis to narrow the possibilities of what this Dark Matter could be.

394 This chapter is organized like the following... **TODO: Text should look like ... Chapter x has**  
395 **blah blah blah.**

## 396 2.2 Dark Matter Basics

397 Presently, a more compelling theory of cosmology that includes Dark Matter (DM) in order  
398 to explain a variety of observations is  $\Lambda$  Cold Dark Matter, or  $\Lambda$ CDM. I present the evidence  
399 supporting  $\Lambda$ CDM in Section 2.3 yet discuss the conclusions of the  $\Lambda$ CDM model here. According  
400 to  $\Lambda$ CDM fit to observations on the Cosmic Microwave Background (CMB), DM is 26.8% of the  
401 universe's current energy budget. Baryonic matter, stuff like atoms, gas, and stars, contributes to  
402 4.9% of the universe's current energy budget [1, 2, 3].

403 DM is dark; it does not interact readily with light at any wavelength. DM also does not interact  
404 noticeably with the other standard model forces (Strong and Weak) at a rate that is readily observed  
405 [3]. DM is cold, which is to say that the average velocity of DM is below relativistic speeds [1].  
406 'Hot' DM would not likely manifest the dense structures we observe like galaxies, and instead  
407 would produce much more diffuse galaxies than what is observed [3, 1]. DM is old; it played a  
408 critical role in the formation of the universe and the structures within it [1, 2].

409 Observations of DM have so far been only gravitational. The parameter space available to what  
410 DM could be therefore is extremely broad. The broad DM parameter space is iteratively tested in

411 DM searches by supposing a hypothesis that has not yet been ruled out and performing observations  
412 to test them. When the observations yield a null result, the parameter space is constrained further.  
413 I present some approaches for DM searches in Section 2.4.

414 **2.3 Evidence for Dark Matter**

415 Dark Matter (DM) has been a looming problem in physics for almost 100 years. Anomalies  
416 have been observed by astrophysicists in galactic dynamics as early as 1933 when Fritz Zwicky  
417 noticed unusually large velocity dispersion in the Coma cluster. Zwicky's measurement was the  
418 first recorded to use the Virial theorem to measure the mass fraction of visible and invisible matter  
419 in celestial bodies [4]. From Zwicky in [5], "*If this would be confirmed, we would get the surprising*  
420 *result that dark matter is present in much greater amount than luminous matter.*" Zwicky's and  
421 others' observation did not instigate a crisis in astrophysics because the measurements did not  
422 entirely conflict with their understanding of galaxies [4]. In 1978, Rubin, Ford, and Norbert  
423 measured rotation curves for ten spiral galaxies [6]. Rubin et al.'s 1978 publication presented a  
424 major challenge to the conventional understanding of galaxies that could no longer be dismissed by  
425 measurement uncertainties. Evidence has been mounting ever since for this exotic form of matter.  
426 The following subsections provide three compelling pieces of evidence in support of the existence  
427 of DM.

428 **2.3.1 First Clues: Stellar Velocities**

429 Zwicky, and later Rubin, measured the stellar velocities of various galaxies to estimate their  
430 virial mass. The Virial Theorem upon which these observations are interpreted is written as

$$2T + V = 0. \quad (2.1)$$

431 Where  $T$  is the kinetic energy and  $V$  is the potential energy in a self-gravitating system. The  
432 classical Newton's law of gravity from stars and gas was used for gravitational potential modeled in  
433 the observed galaxies:

$$V = -\frac{1}{2} \sum_i \sum_{j \neq i} \frac{m_i m_j}{r_{ij}}. \quad (2.2)$$

434 Zwicky et al. measured just the velocities of stars apparent in optical wavelengths [5]. Rubin et al.  
 435 added by measuring the velocity of the hydrogen gas via the 21 cm emission line of Hydrogen [6].  
 436 The velocities of the stars and gas are used to infer the total mass of galaxies and galaxy clusters  
 437 via Equation (2.1). An inferred mass is obtained from the luminosity of the selected sources. The  
 438 two inferences are compared to each other as a luminosity to mass ratio which typically yielded [1]

$$\frac{M}{L} \sim 400 \frac{M_{\odot}}{L_{\odot}} \quad (2.3)$$

439  $M_{\odot}$  and  $L_{\odot}$  referring to stellar mass and stellar luminosity, respectively. These ratios clearly indicate  
 440 a discrepancy in apparent light and mass from stars and gas and their velocities.

441 Rubin et al. [6] demonstrated that the discrepancy was unlikely to be an underestimation of  
 442 the mass of the stars and gas. The inferred "dark" mass was up to 5 times more than the luminous  
 443 mass. This dark mass also needed to extend well beyond the extent of the luminous matter.

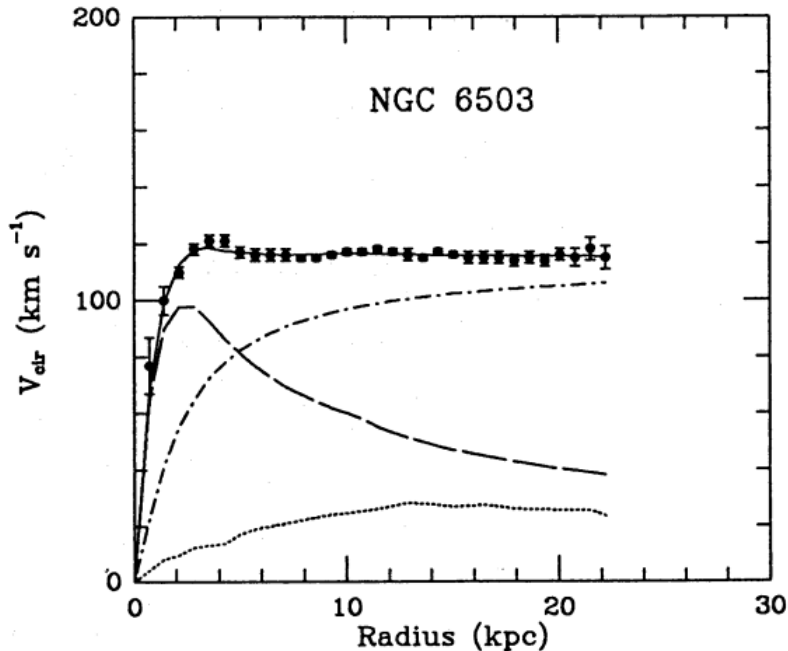


Figure 2.1 Rotation curve fit to NGC 6503 from [7]. Dashed line is the contribution from visible matter. Dotted curves are from gas. Dash-dot curves are from dark matter (DM). Solid line is the composite contribution from all matter and DM sources. Data are indicated with bold dots with error bars. Data agree strongly with a matter + DM composite prediction.

444 Figure 2.1 features one of many rotation curves plotted from the stellar velocities within galaxies.

445 The measured rotation curves mostly feature a flattening of velocities at higher radius which is not  
446 expected if the gravity was only coming from gas and luminous matter. The extension of the  
447 flat velocity region also indicates that the DM is distributed far from the center of the galaxy.  
448 Modern velocity measurements include significantly larger objects, galactic clusters, and smaller  
449 objects, dwarf galaxies. Yet, measurements along this regime are leveraging the Virial theorem  
450 with Newtonian potential energies. We know Newtonian gravity is not a comprehensive description  
451 of gravity. New observational techniques have been developed since 1978, and those are discussed  
452 in the following sections.

453 **2.3.2 Evidence for Dark Matter: Gravitational Lensing**

454 Modern evidence for dark matter comes from new avenues beyond stellar velocities. Grav-  
455 itational lensing from DM is a new channel from general relativity. General relativity predicts  
456 aberrations in light caused by massive objects. In recent decades we have been able to measure the  
457 lensing effects from compact objects and DM halos. Figure 2.2 shows how different massive ob-  
458 jects change the final image of a faraway galaxy resulting from gravitational lensing. Gravitational  
459 lensing developed our understanding of dark matter in two important ways.

460 Gravitational lensing provides additional compelling evidence for DM. The observation of two  
461 merging galactic clusters in 2006, shown in Figure 2.3, provided a compelling argument for DM  
462 outside the Standard Model. These clusters merged recently in astrophysical time scales. Galaxies  
463 and star cluster have mostly passed by each other as the likelihood of their collision is low. Therefore,  
464 these massive objects will mostly track the highest mass, dark and/or baryonic, density. Yet, the  
465 intergalactic gas is responsible for the majority of the baryonic mass in the systems [4]. These gas  
466 bodies will not phase through and will heat up as they collide together. The hot gas is located via  
467 x-ray emission from the cluster. Two observations of the clusters were performed independently of  
468 each other.

469 The first was the lensing of light around the galaxies due to their gravitational influences.  
470 When celestial bodies are large enough, the gravity they exert bends space and time itself. The  
471 warped space-time lenses light and will deflect in an analogous way to how glass lenses will bend

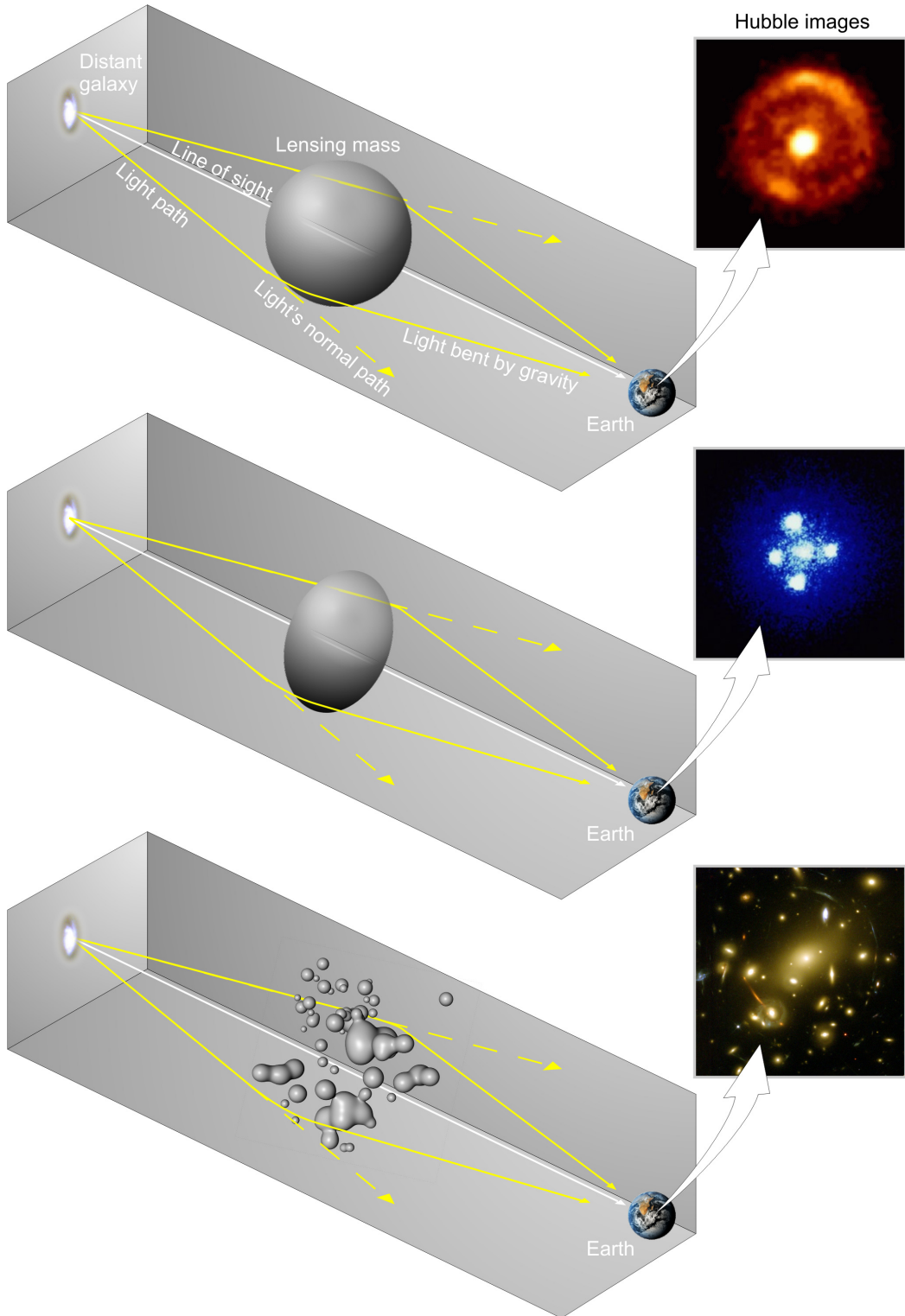


Figure 2.2 Light from distant galaxy is bent in unique ways depending on the distribution of mass between the galaxy and Earth. Yellow dashed lines indicate where the light would have gone if the matter were not present [8].

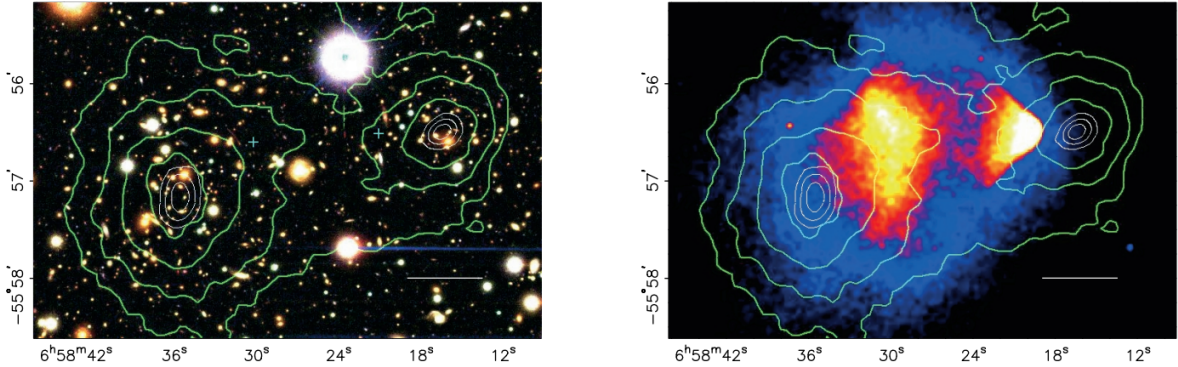


Figure 2.3 (left) Optical image of galactic cluster 1E0657-558. (right) X-ray image of the cluster with redder meaning hotter and higher baryon density. (both) Green contours are reconstruction of gravity contours from weak lensing. White rings are the best fit mass maxima at 68.3%, 95.5%, and 99.7% confidence. The matter maxima of the clusters are clearly separated from x-ray maxima. [9]

472 light, see Figure 2.2. With a sufficient understanding of light sources behind a massive object, we  
 473 can reconstruct the contours of the gravitational lenses. The gradient of the contours shown in  
 474 Figure 2.3 then indicates how dense the matter is and where it is.

475 The x-ray emission can then be observed from the clusters. Since these galaxies are mostly gas  
 476 and are merging, then the gas should be getting hotter. If they are merging, the x-ray emissions  
 477 should be the strongest where the gas is mostly moving through each other. Hence, X-ray emission  
 478 maps out where the gas is in the merging galaxy cluster.

479 The lensing and x-ray observations were done on the Bullet cluster featured on Figure 2.3.  
 480 The x-ray emissions do not align with the gravitational contours from lensing. The incongruence  
 481 in mass density and baryon density suggests that there is a lot of matter somewhere that does  
 482 not interact with light. Moreover, this dark matter cannot be baryonic [9]. The Bullet Cluster  
 483 measurement did not really tell us what DM is exactly, but it did give the clue that DM also does  
 484 not interact with itself very strongly. If DM did interact strongly with itself, then it would have been  
 485 more aligned with the x-ray emission [9]. There have been follow-up studies of galaxy clusters with  
 486 similar results. The Bullet Cluster and others like it provide a persuasive case against something  
 487 possibly amiss in our gravitational theories.

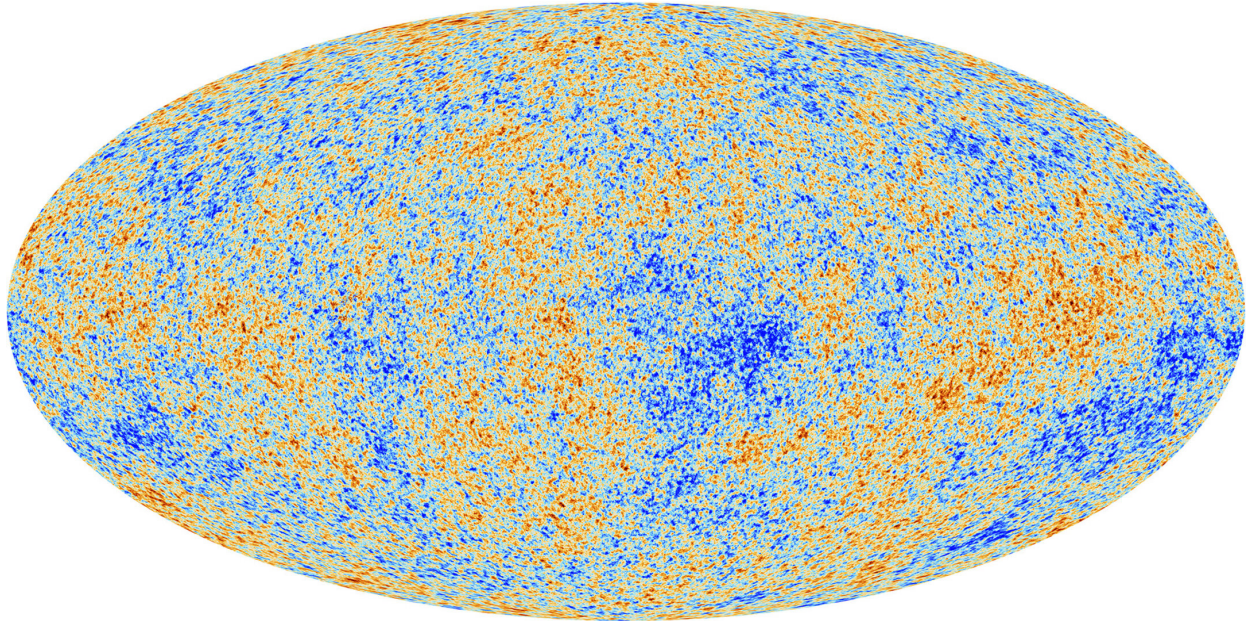


Figure 2.4 Plank CMB sky. Sky map features small variations in temperature in primordial light. These anisotropies are used to make inferences about the universe’s energy budget and developmental history. [10]

488     **2.3.3 Evidence for Dark Matter: Cosmic Microwave Background**

489     The Cosmic Microwave Background (CMB) is the primordial light from the early universe  
490     when Hydrogen atoms formed from the free electron and proton soup in the early universe. The  
491     CMB is the earliest light we can observe; released when the universe was about 380,000 years old.  
492     Then we look at how the simulated universes look like compared to what we see. Figure 2.4 is the  
493     most recent CMB image from the Plank satellite after subtracting the average value and masking the  
494     galactic plane [10]. Redder regions indicate a slightly hotter region in the CMB, and blue indicates  
495     colder. The intensity variations are on the order of 1 in 1000 with respect to the average value.

496     The Cosmic Microwave Background shows that the universe had DM in it from an incredibly  
497     early stage. To measure the DM, Dark Energy, and matter fractions of the universe from the CMB,  
498     the image is analyzed into a power spectrum, which shows the amplitude of the fluctuations as  
499     a function of spherical multipole moments.  $\Lambda$ CDM provides the best fit to the power spectra of  
500     the CMB as shown in Figure 2.5. The CMB power spectrum is quite sensitive to the fraction  
501     of each energy contribution in the early universe. Low  $l$  modes are dominated by variations  
502     in gravitational potential. Intermediate  $l$  emerge from oscillations in photon-baryon fluid from

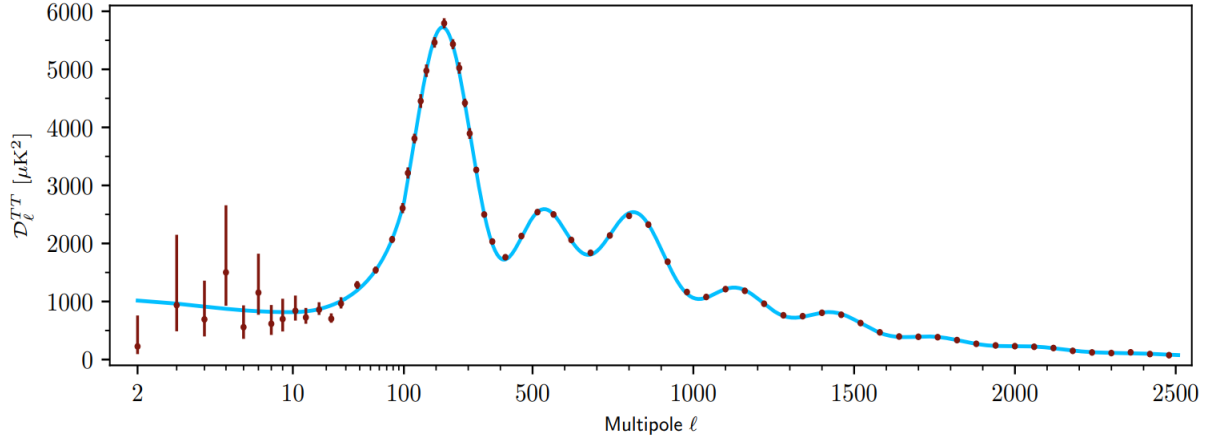


Figure 2.5 Observed Cosmic Microwave Background power spectrum as a function of multipole moment from Plank [10]. Blue line is best fit model from  $\Lambda$ CDM. Red points and lines are data and error, respectively.

503 competing baryon pressures and gravity. High  $l$  is a damped region from the diffusion of photons  
 504 during electron-proton recombination. [1]

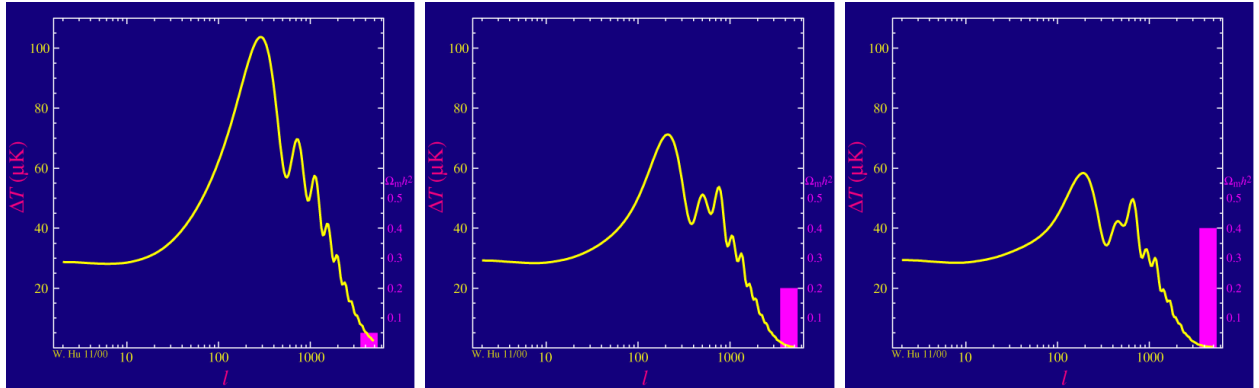


Figure 2.6 Predicted power spectra of CMB for different  $\Omega_m h^2$  values for fixed baryon density from [11]. (left) Low  $\Omega_m h^2$  increases the prominence of first and second peaks. (middle)  $\Omega_m h^2$  is most similar to the observed power spectrum. The second and third peaks are similar in height. (right)  $\Omega_m h^2$  is large which suppresses the first peak and raises the prominence of the third peak.

505 The harmonics would look quite different for a universe with less DM. Figure 2.6 demonstrates  
 506 the effect  $\Omega_m h^2$  has on the expected power spectrum for fixed baryon matter density. [11] Sweeping  
 507  $\Omega_m h^2$  in this way clearly shows the effect dark matter has on the CMB power spectrum. The  
 508 observations fit well with the  $\Lambda$ CDM model, and the derived fractions are as follows. The matter  
 509 fraction:  $\Omega_m = 0.3153$ ; and the baryon fraction:  $\Omega_b = 0.04936$  [10]. Plank's observations also  
 510 provide a measure of the Hubble constant,  $H_0$ .  $H_0$  especially has seen a growing tension in the

511 past decade that continues to deepened with observations from instruments like the James Webb  
512 Telescope [12, 13]. As Hubble tensions deepen, we may find that perhaps  $\Lambda$ **CDM**, despite its  
513 successes, is missing some critical physics.

514 Overall, the Newtonian motion of stars in galaxies, weak lensing from galactic clusters, and  
515 power spectra from primordial light form a compelling body of research in favor of dark matter.  
516 It takes another leap of theory and experimentation to make observations of DM that are non-  
517 gravitational in nature. In Section 2.3, the evidence for DM implies strongly that the DM is matter  
518 and not a lost parameter in the gravitational fields between massive objects. Finally, if we take one  
519 axiom: that this matter has quantum behavior, such as being described by some Bohr wavelength  
520 and abiding by some fermion or boson statistics; then we arrive at particle dark matter. One particle  
521 DM hypothesis is the Weakly Interacting Massive Particle (WIMP). This DM candidate theory is  
522 discussed further in the next section and is the focus of this thesis.

## 523 2.4 Searching for Dark Matter: Particle DM

524 Section 2.4 shows the Standard Model of particle physics and is currently the most accurate  
525 model for the dynamics of fundamental particles like electrons and photons. The current status  
526 of the SM does not have a viable DM candidate. When looking at the standard model, we can  
527 immediately exclude any charged particle because charged particles interact strongly with light.  
528 Specifically, this will rule out the following charged, fundamental particles:  $e, \mu, \tau, W, u, d, s, c, t, b$   
529 and their corresponding antiparticles. Recalling from Section 2.2 that DM must be long-lived and  
530 stable over the age of the universe which excludes all SM particles with decay half-lives at or shorter  
531 than the age of the universe. The lifetime constraint additionally eliminates the  $Z$  and  $H$  bosons.  
532 Finally, the candidate DM needs to be somewhat massive. Recall from Section 2.2 that DM is cold  
533 or not relativistic through the universe. This eliminates the remaining SM particles:  $\nu_{e,\mu,\tau}, g, \gamma$  as  
534 DM candidates. Because there are no DM candidates within the SM, the DM problem strongly  
535 hints to physics beyond the SM (BSM).

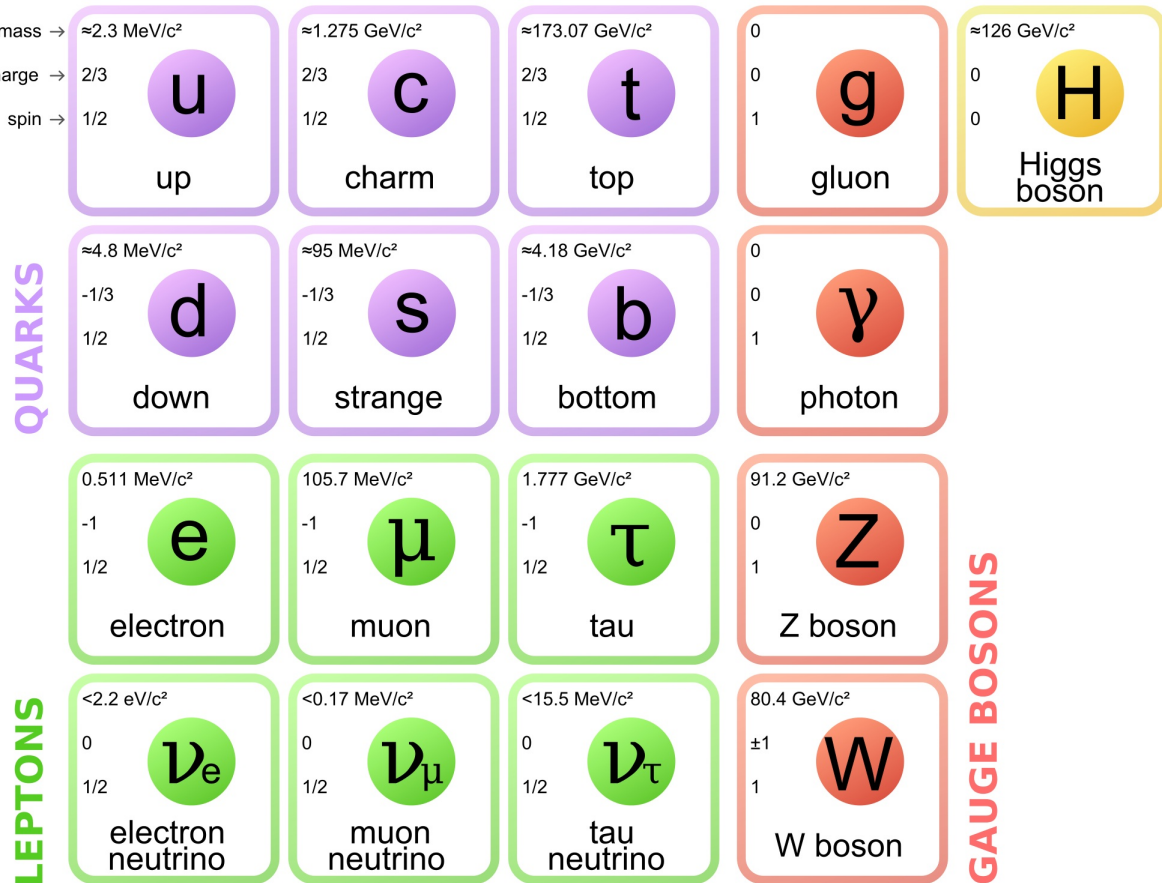


Figure 2.7 The Standard Model (SM) of particle physics. Figure taken from <http://www.quantumdiaries.org/2014/03/14/the-standard-model-a-beautiful-but-flawed-theory/>

### 536 2.4.1 Shake it, Break it, Make it

537 When considering DM that couples in some way with the SM, the interactions are roughly  
 538 demonstrated by interaction demonstrated in Figure 2.8. The figure is a simplified Feynman  
 539 diagram where the arrow of time represents the interaction modes of: **Shake it, Break it, Make it.**

540 **Shake it** refers to the direct detection of dark matter. Direct detection interactions start with  
 541 a free DM particle and an SM particle. The DM and SM interact via elastic or inelastic collision  
 542 and recoil away from each other. The DM remains in the dark sector and imparts some momentum  
 543 onto the SM particle. The hope is that the momentum imparted onto the SM particle is sufficiently  
 544 high enough to pick up with extremely sensitive instruments. Because we cannot create the DM in  
 545 the lab, a direct detection experiment must wait until DM is incident on the detector. Most direct  
 546 detection experiments are therefore placed in low-background environments with inert detection

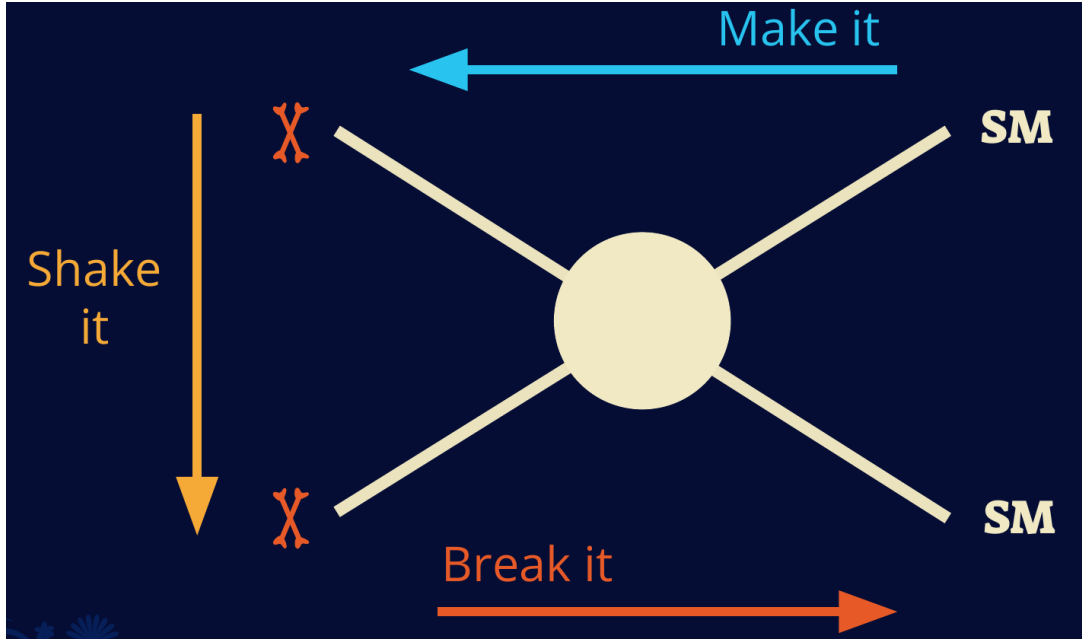


Figure 2.8 Simplified Feynman diagram demonstrating different ways DM can interact with SM particles. The 'X's refer to the DM particles whereas the SM refer to fundamental particles in the SM. The large circle in the center indicates the vertex of interaction and is purposely left vague. The colored arrows refer to different directions of time as well as their respective labels. The arrows indicate the initial and final state of the DM -SM interaction in time.

547 media like the noble gas Xenon. [14]

548 **Make it** refers to the production of DM from SM initial states. The experiment starts with  
 549 particles in the SM. These SM particles are accelerated to incredibly high energies and then collide  
 550 with each other. In the confluence of energy, DM hopefully emerges as a byproduct of the SM  
 551 annihilation. Often it is the collider experiments that are energetic enough to hypothetically produce  
 552 DM. These experiments include the world-wide collaborations ATLAS and CMS at CERN where  
 553 proton collide together at extreme energies. The DM searches, however, are complex. DM likely  
 554 does not interact with the detectors and lives long enough to escape the detection apparatus of  
 555 CERN's colliders. This means any DM production experiment searches for an excess of events  
 556 with missing momentum or energy in the events. An example event with missing transverse  
 557 momentum is shown in Figure 2.9. The missing momentum with no particle tracks implies a  
 558 neutral particle carried the energy out of the detector. However, there are other neutral particles  
 559 in the SM, like neutrons or neutrinos, so any analysis has to account for SM signatures of missing

560 momentum. [15]

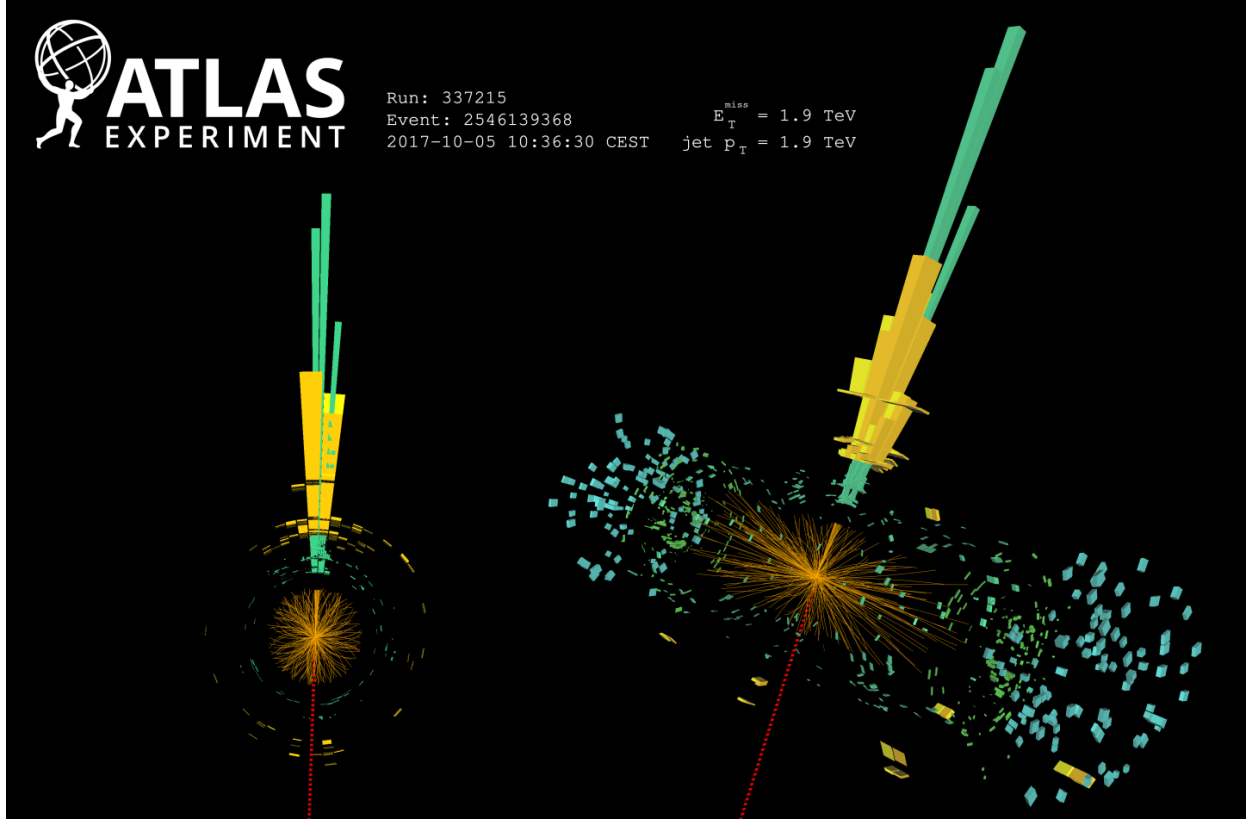


Figure 2.9 A single jet event in ATLAS detector from 2017 [16]. Jet momentum was observed to be 1.9 TeV. Missing transverse momentum was observed to be 1.9 TeV compared to the initial transverse momentum of the event was 0. Implied MET is traced by a red dashed line in event display.

#### 561 2.4.2 Break it: Standard Model Signatures of Dark Matter through Indirect Searches

562 **Break it** refers to the creation of SM particles from the dark sector, and it is the primary focus  
563 of this thesis. The interaction begins with DM or in the dark sector. The hypothesis is that this  
564 DM will either annihilate with itself or decay and produce an SM byproduct. This method is  
565 often referred to as the Indirect Detection of DM because we have no lab to directly control or  
566 manipulate the DM. Therefore, most indirect DM searches are performed using observations of  
567 known DM densities among the astrophysical sources. The strength is that we have the whole of the  
568 universe and its 13.6-billion-year lifespan to use as a detector and particle accelerator. Additionally,  
569 locations of dark matter are well cataloged since it was astrophysical observations that presented

570 the problem of DM in the first place.

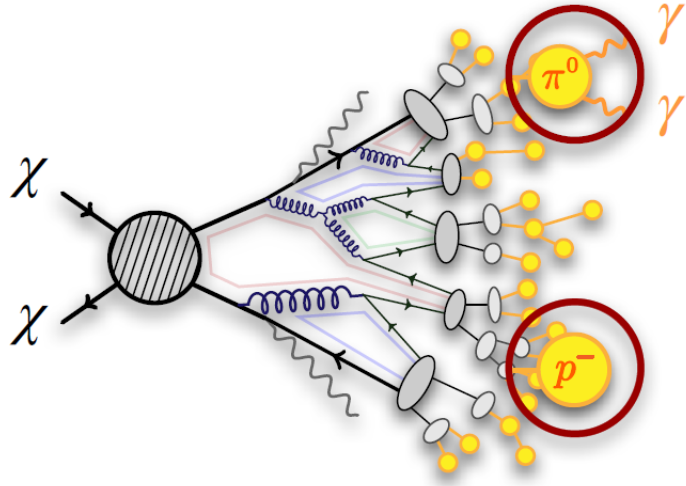


Figure 2.10 More detailed pseudo-Feynman diagram of particle cascade from dark matter annihilation into 2 quarks. The quarks hadronize and down to stable particles like  $\gamma$  or the anti-proton ( $p^-$ ). Diagram pulled from ICRC 2021 presentation on DM annihilation search [17].

571 However, anything can happen in the universe. There are many difficult to deconvolve back-  
572 grounds when searching for DM. One prominent example is the galactic center. We know the  
573 galactic center has a large DM content because of stellar kinematics in our Milky Way and DM halo  
574 simulations. Yet, any signal from the galactic center is challenging to parse apart from the extreme  
575 environment of our supermassive black hole, unresolved sources, and diffuse emission from the  
576 interstellar medium [18]. Despite the challenges, any DM model that yields evidence in the other  
577 two observation methods, **Shake it or Make it** must be corroborated with indirect observations of  
578 the known DM sources. Without corroborating evidence, DM observation in the lab is hard-pressed  
579 to demonstrate that it is the model contributing to the DM seen at the universal scale.

580 In the case of WIMP DM, signals are described in terms of primary SM particles produced  
581 from DM decay or annihilation. The SM initial state particles are then simulated down to stable  
582 final states such as the  $\gamma$ ,  $\nu$ ,  $p$ , or  $e$  which can traverse galactic lengths to reach Earth.

583 Figure 2.10 shows the quagmire of SM particles that emerges from SM initial states that are not  
584 stable [17]. There are many SM particles with varying energies that can be produced in such an

585 interaction. For any arbitrary DM source and stable SM particle, the SM flux from DM annihilating  
 586 to a neutral particle in the SM,  $\phi$ , from a region in the sky is described by the following.

$$\frac{d\Phi_\phi}{dE_\phi} = \frac{\langle\sigma v\rangle}{8\pi m_\chi^2} \frac{dN_\phi}{dE_\phi} \times \int_{\text{source}} d\Omega \int_{l.o.s} \rho_\chi^2 dl(r, \theta') \quad (2.4)$$

587 In Equation (7.1),  $\langle\sigma v\rangle$  is the velocity-weighted annihilation cross-section of DM to the SM.  $m_\chi$   
 588 refers to the mass of DM, noted with Greek letter  $\chi$ .  $\frac{dN_\phi}{dE_\phi}$  is the N particle flux weighted by the  
 589 particle energy. An example is provided in Figure 2.11 for the  $\gamma$  final state. The integrated terms  
 590 are performed over the solid angle,  $d\Omega$ , and line of sight, l.o.s.  $\rho$  is the density of DM for a  
 591 location  $(r, \theta')$  in the sky. The terms left of the ' $\times$ ' are often referred to as the particle physics  
 592 component. The terms on the right are referred to as the astrophysical component. For decaying  
 593 DM, the equation changes to...

$$\frac{d\Phi_\phi}{dE_\phi} = \frac{1}{4\pi\tau m_\chi} \frac{dN_\phi}{dE_\phi} \times \int_{\text{source}} d\Omega \int_{l.o.s} \rho_\chi dl(r, \theta') \quad (2.5)$$

594 In Equation (6.1),  $\tau$  is the decay lifetime of the DM. Just as in Equation (7.1), the left and right  
 595 terms are the particle physics and the astrophysical components respectively. The integrated  
 596 astrophysical component of Equation (7.1) is often called the J-Factor. Whereas the integrated  
 597 astrophysical component of Equation (6.1) is often called the D-Factor.

598     Exact DM  $\text{DM} \rightarrow \text{SM SM}$  branching ratios are not known, so it is usually assumed to go 100%  
 599 into an SM particle/anti-particle. Additionally, when a DM annihilation or decay produces one of  
 600 the neutral, long-lived SM particles ( $\nu$  or  $\gamma$ ), the particle is traced back to a DM source. For DM  
 601 above GeV energies, there are very few SM processes that can produce particles with such a high  
 602 energy. Seeing such a signal would almost certainly be an indication of the presence of dark matter.  
 603 Fortunately, the universe provides us with the largest volume and lifetime ever for a particle physics  
 604 experiment.

## 605 2.5 Sources for Indirect Dark Matter Searches

606     The first detection of DM relied on optical observations. Since then, we have developed new  
 607 techniques to find DM dense regions. As described in Section 2.3.1, many DM dense regions were  
 608 through observing galactic rotation curves. Our Milky Way galaxy is among DM dense regions

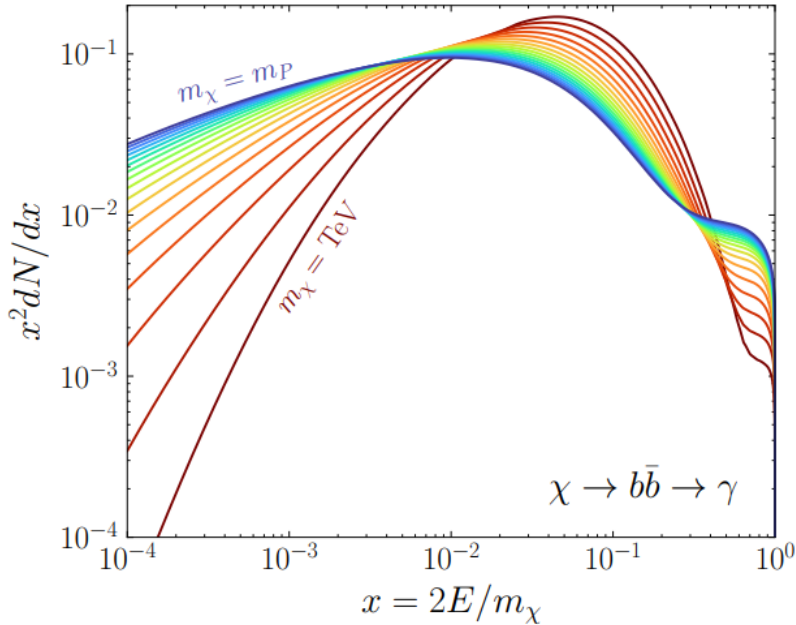


Figure 2.11 Dark Matter (DM) decay spectrum for  $b\bar{b}$  initial state and  $\gamma$  final state. Redder spectra are for larger DM masses. Bluer spectra are light DM masses.  $x$  is a unitless factor defined as the ratio of the mass of DM,  $m_\chi$ , and the final state particle energy  $E_\gamma$ . Figure from [19].

discovered, and it is the largest nearby DM dense region to look at. Additionally, the DM halo surrounding the Milky Way is clumpy [18]. There are regions in the DM halo of the Milky Way that have more DM than others that have captured gas over time. These sub-halos were dense enough collapse gas and form stars. These apparent sub galaxies are known as dwarf spheroidal galaxies and are the main sources studied in this thesis. Each source type comes with different trade-offs. Galactic Center studies will be very sensitive to the assumed distribution of DM. The central DM density can vary substantially as demonstrated in Figure 2.12. At distances close to the center of the galaxy, or small  $r$ , the differences in DM densities can be 3-4 orders of magnitude. Searches toward the galactic center will therefore be quite sensitive to the assumed DM distribution.

Searches toward Dwarf Spheroidal Galaxies (dSph's) suffer from uncertainties in the DM density less than the galactic center studies. This is mostly from their diminutive size being smaller than the angular resolution of most  $\gamma$ -ray observatories [18]. The DM content dSph's are typically determined with the Virial theorem, Equation (2.1), and are usually majority DM [18] in mass. DSph's tend to be ideal sources to look at for DM searches. Their environments are quiet with little

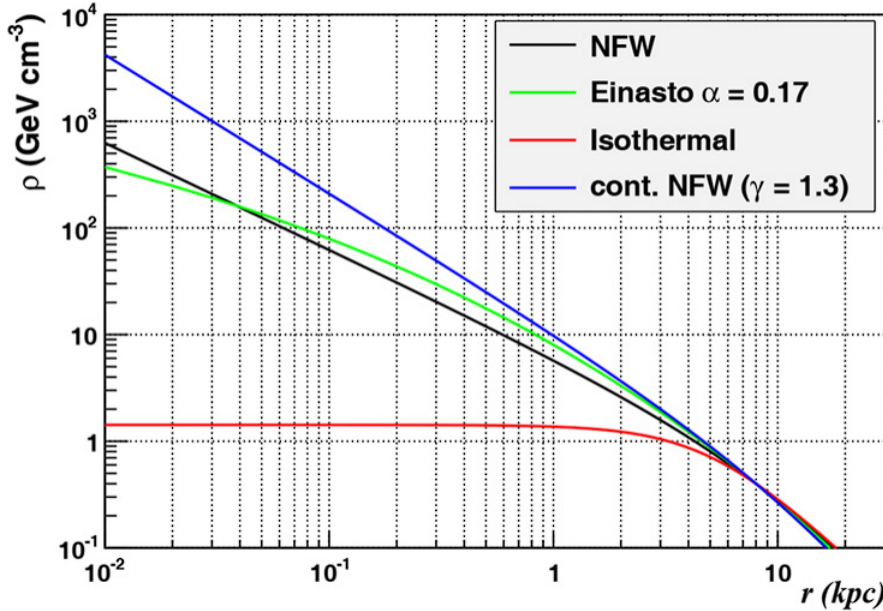


Figure 2.12 Different dark matter density profiles compared. Some models produce exceptionally large densities at small  $r$  [20].

623 astrophysical background. Unlike the galactic center, the most active components of dSph's are the  
 624 stars within them versus a violent accretion disc around a black hole. All this together means that  
 625 dSph's are among the best sources to look at for indirect DM searches. dSph's are the targets of  
 626 focus for this thesis.

## 627 2.6 Multi-Messenger Dark Matter

628 Astrophysics entered a new phase in the past few decades that leverages our increasing sensitivity  
 629 to SM channels and general relativity (GR). Up until the 21st century, astrophysical observations  
 630 were performed with photons ( $\gamma$ ) only. Astrophysics with this 'messenger' is fairly mature now.  
 631 Novel observations of the universe have since only adjusted the sensitivity of the wavelength of  
 632 light that is observed except at MeV energies. Gems like the CMB [10], and more have ultimately  
 633 been observations of different wavelengths of light. Multi-messenger astrophysics proposes using  
 634 other SM particles such the  $p^{+/-}$ , or  $\nu$  or gravitation waves predicted by general relativity.

635 The experiment LIGO had a revolutionary discovery in 2016 with the first detection of a binary  
 636 black hole merger [21]. This opened the collective imagination to observing the universe through  
 637 gravitational waves. There has also been a surge of interest in the neutrino ( $\nu$ ) sector. IceCube

638 demonstrated that we are sensitive to neutrinos in regions that correlate with significant photon  
 639 emission like the galactic plane [22]. Neutrinos, like gravitational waves and light, travel mostly  
 640 unimpeded from their source to our observatories. This makes pointing to the originating source  
 641 of these messengers much easier than it is for cosmic rays which are deflected from their source by  
 642 magnetic fields.

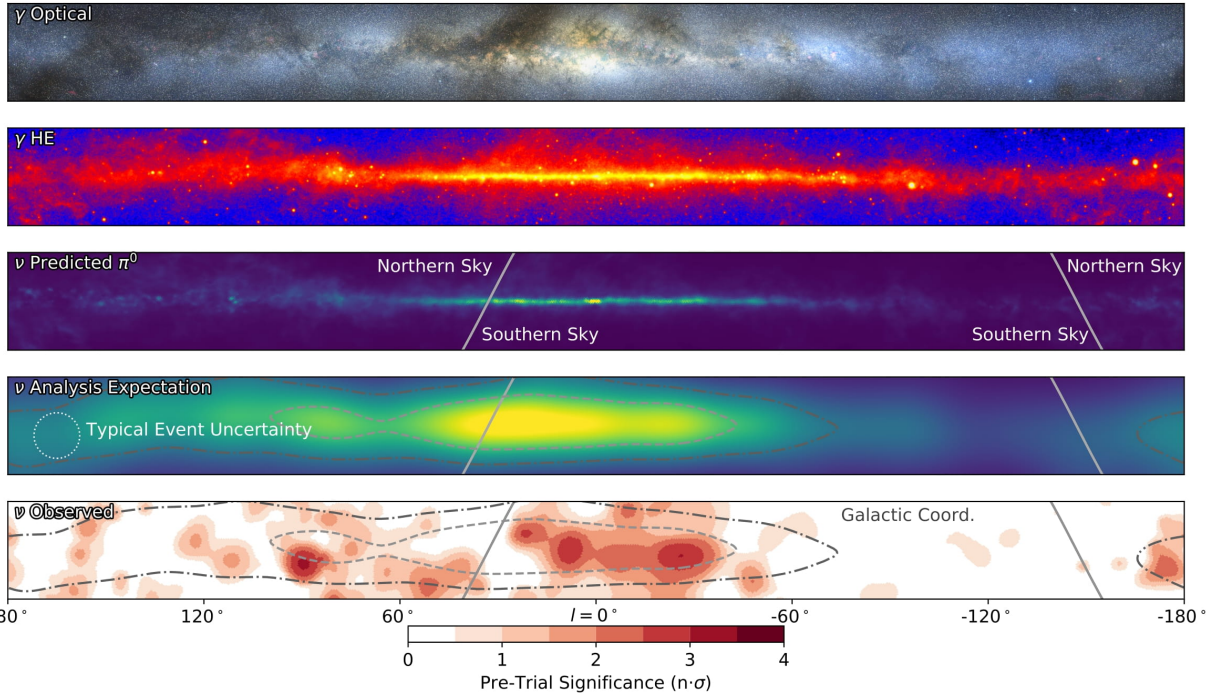


Figure 2.13 The Milky Way Galaxy in photons ( $\gamma$ ) and neutrinos ( $\nu$ ) [22]. The Galactic center is at  $l=0^\circ$  and is the brightest region in all panels. (top) An Optical color image of the Milky Way galaxy seen from Earth. Clouds of gas and dust obscure some light from stars. (2nd down) Integrated flux of  $\gamma$ -rays observed by the Fermi-LAT telescope [23]. (middle) Expected neutrino emission that corresponds with Fermi-LAT observations. (2nd up) Expected neutrino emission profile after considering detector systematics of IceCube. (bottom) Observed neutrino emission from region of the galactic plane. Substantial neutrino emission was detected.

643 The IceCube collaboration recently published a groundbreaking result of the Milky Way in  
 644 neutrinos. The recent result from IceCube, shown in Figure 2.13, proves that we can make  
 645 observations under different messenger regimes. The top two panels show the appearance of the  
 646 galactic plane to different wavelengths of light. Some sources are more apparent in some panels,  
 647 while others are not. This new channel is powerful because neutrinos are readily able to penetrate  
 648 through gas and dust in the Milky Way. This new image also refines our understanding of how high

649 energy particles are produced. For example, the fit to IceCube data prefers neutrino production  
 650 from the decay of  $\pi^0$  [22].

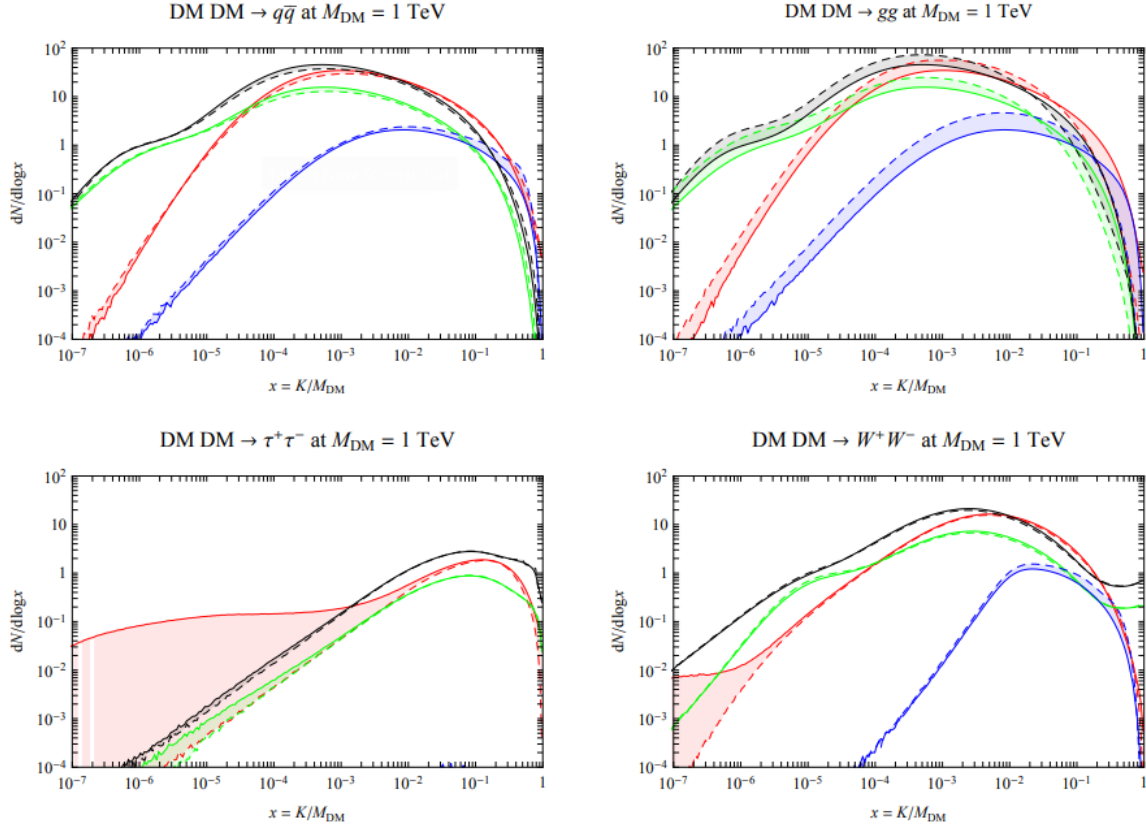


Figure 2.14 Dark Matter annihilation spectra for different final state particle and standard model annihilation channels [24]. Photons (red),  $e^\pm$  (green),  $\bar{p}$  (blue),  $\nu$  (black).

651 Exposing our observations to more cosmic messengers greatly increases our sensitivity to  
 652 rare processes. In the case of DM, Figure 2.14, there are many SM particles produced in DM  
 653 annihilation. Among the final state fluxes are gammas and neutrinos. Charged particles are also  
 654 produced however they would not likely make it to Earth since they will be deflected by magnetic  
 655 fields between the source and Earth. This means observatories that can see the neutral messengers  
 656 are especially good for DM searches and for combining data for a multi-messenger DM search.

## **CHAPTER 3**

657                   **HIGH ALTITUDE WATER CHERENKOV (HAWC) OBSERVATORY**

658   **3.1 The Detector**

659   **3.2 Events Reconstruction and Data Acquisition**

660   **3.2.1 G/H Discrimination**

661   **3.2.2 Angle**

662   **3.2.3 Energy**

663   **3.3 Remote Monitoring**

664   **3.3.1 ATHENA Database**

665   **3.3.2 HOMER**

666

## **CHAPTER 4**

### **ICECUBE NEUTRINO OBSERVATORY**

667 **4.1 The Detector**

668 **4.2 Events Reconstruction and Data Acquisition**

669 **4.2.1 Angle**

670 **4.2.2 Energy**

671 **4.3 Northern Test Site**

672 **4.3.1 PIgeon remote dark rate testing**

673 **4.3.2 Bulkhead Construction**

## CHAPTER 5

### GLORY DUCK: MULTI-WAVELENGTH SEARCH FOR DARK MATTTER ANNIHILATION TOWARDS DWARF SPHEROIDAL GALAXIES

#### 5.1 Introduction

The field of astrophysics now has several instruments and observatories sensitive to high energy gamma-rays. The energy sensitivity for the modern gamma-ray program spans many orders of magnitude. Figure 5.1 demonstrates these similar sensitivities across energies for the five experiments: Fermi-LAT, HAWC, HESS, MAGIC, and VERITAS.

Each of the five experiments featured in Figure 5.1 have independently searched for DM annihilation from dwarf spheroidal galaxies (dSph) and set limits. Intriguingly, there are regions of substantial overlap in their energy sensitivities. This clearly motivates an analysis that combines data from these five. Each experiment has unique gamma-ray detection methods and their weaknesses and strengths can be leveraged with each other. The HAWC gamma-ray observatory is extensively introduced in chapter 3, so it is not introduced here. A brief description of the remaining experiments are in the following paragraphs.

The Large Area Telescope (LAT) is a pair conversion telescope mounted on the NASA Fermi satellite in orbit  $\sim$ 550 km above the Earth [26]. LAT's field of view covers about 20% of the whole sky, and it sweeps the whole sky approximately every 3 hours. LAT's gamma-ray energy sensitivity ranges from 20 MeV up to 1 TeV. Previous DM searches towards dSphs using Fermi-LAT are published in [27] and [28]

The High Energy Spectroscopic System (HESS), Major Atmospheric Gamma Imaging Cherenkov (MAGIC), and Very Energetic Radiation Imaging Telescope Array System (VERITAS) are arrays of Imaging Atmospheric Cherenkov Telescopes (IACT). These telescopes observe the Cherenkov light emitted from gamma-ray showers in the Earth's atmosphere. The field of view for these telescopes is no larger than  $5^\circ$  with energy sensitivities ranging from 30 GeV up to 100 TeV [29, 30, 31]. IACTs are able to make precise observations in selected regions of the sky, however can only be operated in ideal dark conditions. HESS's observations of the dwarves

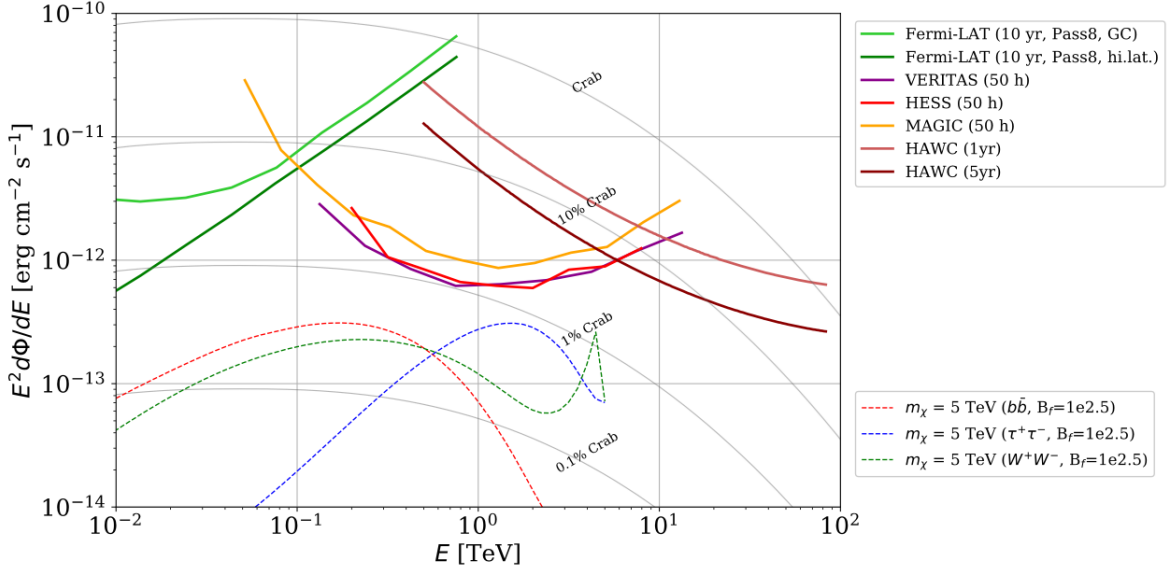


Figure 5.1 Sensitivities of five gamma-ray experiments compared to percentages of the Crab nebula’s emission and dark matter annihilation. Solid lines present estimated sensitivities to power law spectra [FACT CHECK THIS] for each experiment. Green lines are Fermi-LAT sensitivities where lighter green is the sensitivity to the galactic center and dark green is its sensitivity to higher declinations. Orange, red, and purple solid lines represent the MAGIC, HESS, and VERITAS 50 hour sensitivities respectively. The maroon and brown lines are the HAWC 1 year and 5 year sensitivities. Across four decades of gamma-ray energy, these experiments have similar sensitivities on the order  $10^{-12}$  erg  $\text{cm}^{-2}\text{s}^{-1}$ . The dotted lines are estimated dark matter fluxes assuming  $m_\chi = 5$  TeV DM annihilating to bottom quarks (red), tau leptons (blue), and W bosons (green). Faded gray lines outline percentage flux of the Crab nebula. Figure is an augmented version of [25]

700 Sculptor and Carina were between January 2008 and December 2009. HESS’s observations of  
 701 Coma Berenices were from 2010 to 2013, and Fornax was observed in 2010 [32, 33, 34]. MAGIC  
 702 provided deep observations of Segue1 between 2011 and 2013 [35]. MAGIC also provides data  
 703 for three dwarves: Coma Berenices, Draco, and Ursa Major II where observations were made  
 704 in: January - June 2019 [36], March - September 2018 [36], and 2014 - 2016 [37] respectively.  
 705 VERITAS provided data for Boötes I, Draco, Segue 1, and Ursa Minor from 2009 to 2016 [38].

706 This chapter presents the Glory Duck analysis, the name given for the search for dark matter  
 707 annihilation from dSph by combining data from the five gamma-ray observatories: Fermi-LAT,  
 708 HAWC, HESS, MAGIC, and VERITAS. Specifically, the methods in analysis and modeling are  
 709 presented for the HAWC gamma-ray observatory. This work was published to the Journal of  
 710 Cosmology and Astroparticle Physics and presented at the International Cosmic Ray Conference

711 in 2019, 2021, and 2023 [39, 40, 41] and others.

712 **5.2 Dataset and Background**

713 This section enumerates the data and background methods used for HAWC’s study of dSphs.

714 Section 5.2.1 and Section 5.2.2 are most useful for fellow HAWC collaborators looking to replicate  
715 the Glory Duck analysis.

716 **5.2.1 Itemized HAWC files**

717 • Detector Resolution: `response_aerie_svn_27754_systematics_best_mc_test_no`  
718     `broadpulse\_10pctlogchargesmearing_0.63qe_25kHzNoise_run5481_curvatu`  
719     `re0_index3.root`

720 • Data Map: `maps-20180119/liff/maptree_1024.root`

721 • Spectral Dictionary: `DM_CirrelliSpectrum_dict_gammas.npy`

722 • Analysis wiki: [https://private.hawc-observatory.org/wiki/index.php/Glory\\_Duck\\_Multi-Experiment\\_Dark\\_Matter\\_Search](https://private.hawc-observatory.org/wiki/index.php/Glory_Duck_Multi-Experiment_Dark_Matter_Search)

724 **5.2.2 Software Tools and Development**

725 This analysis was performed using HAL and 3ML [42, 43] in Python version 2. I built software  
726 to implement the *A Poor Particle Physicist Cookbook for Dark Matter Indirect Detection* (PPPC)  
727 [44] DM spectral model and dSphs spatial model from [45] for HAWC analysis. A NumPy version  
728 of this dictionary was made for both Py2 and Py3. The code base for creating this dictionary is  
729 linked on my GitLab sandbox:

730 • Py2: [Dictionary Generator \(Deprecated\)](#)

731 • Py3: [PPPC2Dict](#)

732 The analysis was performed using the  $f_{\text{hit}}$  framework performed in the HAWC Crab paper  
733 [42]. The Python2 NumPy dictionary file for gamma-ray final states is `dmCirSpecDict.npy`. The  
734 corresponding Python3 file is `DM_CirrelliSpectrum_dict_gammas.npy`. These files can also

735 be used for decay channels and the PPPC describes how [44]. All other software used for data  
736 analysis, DM profile generation, and job submission to SLURM are also kept in my sandbox for  
737 [the Glory Duck](#) project.

### 738 5.2.3 Data Set and Background Description

739 The HAWC data maps used for this analysis contain 1017 days of data between runs 2104  
740 (2014-11-26) and 7476 (2017-12-20). They were generated from pass 4.0 reconstruction. The  
741 analysis is performed using the  $f_{hit}$  energy binning scheme with bins (1-9) similar to what was done  
742 for the Crab and previous HAWC dSph analysis [42, 46]. Bin 0 was excluded as it has substantial  
743 hadronic contamination and poor angular resolution.

744 This analysis was done on dSphs because of their large DM mass content relative to baryonic  
745 mass. We consider the following to estimate the background to this study.

- 746 • The dSphs are small in HAWC’s field of view, so the analysis is not sensitive to large or small  
747 scale anisotropies.
- 748 • The dSphs used in this analysis are off the galactic plane.
- 749 • The dSphs are baryonically faint relative to their expected dark matter content and are not  
750 expected to contain high energy gamma-ray sources.

751 Therefor we make no additional assumptions on the background from our sources and use  
752 HAWC’s standard direct integration method for background estimation [42]. It is possible for  
753 gamma rays from DM annihilation to scatter in transit to HAWC via Inverse Compton Scattering  
754 (ICS). This was investigated and its impact on the flux is basically zero. Supporting information  
755 on this is in Section 5.7.1

## 756 5.3 Analysis

757 The expected differential photon flux from DM-DM annihilation to standard model particles,  
758  $d\Phi_\gamma/dE_\gamma$ , over solid angle,  $\Omega$  is described by the familiar equation.

$$\frac{d\Phi_\gamma}{dE_\gamma} = \frac{\langle\sigma v\rangle}{8\pi m_\chi^2} \frac{dN_\gamma}{dE_\gamma} \times \int_{\text{source}} d\Omega \int_{l.o.s} \rho_\chi^2 dl(r, \theta') \quad (5.1)$$

759 Where  $\langle \sigma v \rangle$  is the velocity weighted annihilation cross-section.  $\frac{dN}{dE}$  is the expected differential  
 760 number of photons produced at each energy per annihilation.  $m_\chi$  is the rest mass of the supposed  
 761 DM particle.  $\rho_\chi$  is the DM density.  $J$  is the astrophysical J-factor and is defined as

$$J = \int d\Omega \int_{l.o.s} dl \rho_\chi^2(r, \theta') \quad (5.2)$$

762  $l$  is the distance to the source from Earth.  $r$  is the radial distance from the center of the source.  $\theta'$  is  
 763 the half angle defining a cone containing the DM source. How each component is synthesized and  
 764 considered for HAWC's analysis is presented in the following sections. Section 5.3.1 presents the  
 765 particle physics model for DM annihilation. Section 5.3.2 presents the spatial distributions built  
 766 for each dSph.

767 **5.3.1  $\frac{dN_\gamma}{dE_\gamma}$  - Particle Physics Component**

768 For these spectra, we import the PPPC with Electroweak (EW) corrections [44]. The spectrum  
 769 is implemented as a model script in astromodels for 3ML. The EW corrections were previously not  
 770 considered for HAWC and are significant for DM annihilating to EW coupled SM particles such  
 771 as all leptons, and the  $\gamma$ ,  $Z$ , and  $W$  bosons [46]. Figure 5.2 demonstrates the significance of EW  
 772 corrections for W boson annihilation. Across EW SM channels, the gamma-ray spectra become  
 773 harder than spectra without EW corrections. Tables from the PPPC were reformatted into Python  
 774 NumPy dictionaries for collaboration-wide use. A class in astromodels was developed to include  
 775 the EW correction from the PPPC and is aptly named `PPPCSpectra` within `DM_models.py`.

776 **5.3.2  $J$ - Astrophysical Component**

777 The J-factor profiles for each source are imported from Geringer-Sameth (referred to with  $\mathcal{GS}$ )  
 778 [45]. These were pulled from the publication as  $J(\theta)$ , where  $\theta$  is the angular separation from the  
 779 center of the source. HAWC requires maps in terms of  $\frac{dJ}{d\Omega}$ , so the conversion from the maps was  
 780 done in the following way...

781 First, convert the angular distances to solid angles

$$\Omega = 2 \cdot \pi(1 - \cos(\theta)) \quad (5.3)$$

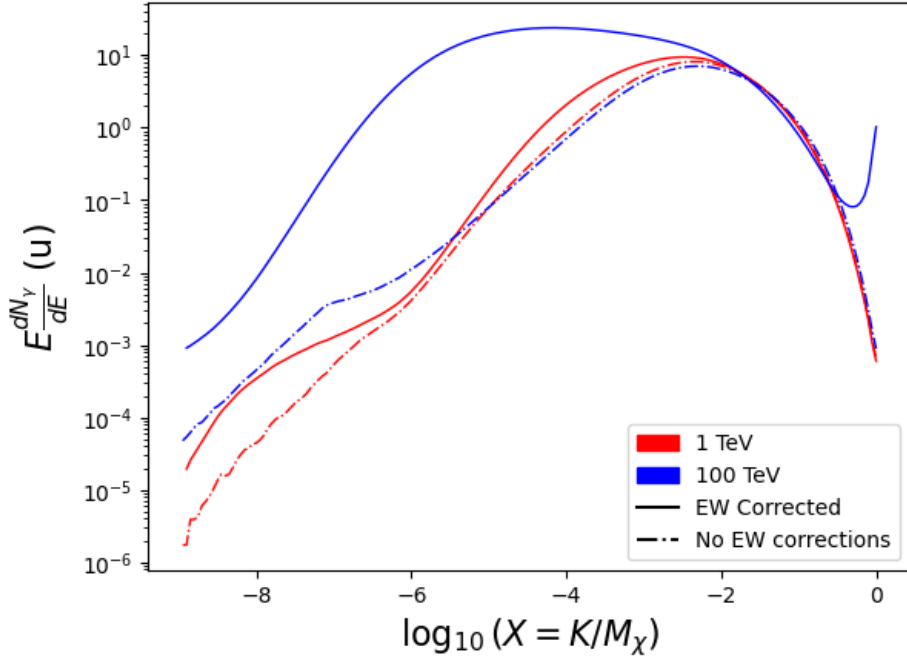


Figure 5.2 Effect of Electroweak (EW) corrections on expected DM annihilation spectrum for  $\chi\chi \rightarrow W^-W^+$ . Solid lines are spectral models that consider EW corrections. Dash-dot lines are spectral models without EW corrections. Red lines are models for  $M_\chi = 1$  TeV. Blue lines represent models for  $M_\chi = 100$  TeV. All models are sourced from the PPPC4DMID [44].

which reduces with a small angle approximation to  $\pi\theta^2$ . Next, the central difference for both the  $\Delta J$  and  $\Delta\Omega$  value were calculated from the discretized  $J(\theta)$  with the central difference stencil:

$$\Delta\phi_i = \phi_{i+1} - \phi_{i-1} \quad (5.4)$$

Where  $\phi$  is either  $\Omega$  or  $J$ . These were done separately in case the grid spacing in  $\theta$  was not uniform. Finally, these lists are divided so that we are left with an approximation of the  $dJ/d\Omega$  profile that is a function of  $\theta$ . Admittedly, this is an approximation method for the map which introduces small errors compared to the true profile estimate. This was checked as a systematic against the author's profiling of the spatial distribution and is documented in Section 5.8.1.

With  $\frac{dJ}{d\Omega}(\theta)$ , a map is generated, first by filling in the north-east quadrant of the map. This quadrant is then reflected twice, vertically then horizontally, to fill the full map. Maps are then normalized by dividing the discrete 2D integral of the map. The 2D integral was a simple height

792 of bins, Newton’s integral:

$$p^2 \cdot \sum_{i,j=0}^{N,M} \frac{dJ}{d\Omega}(\theta_{i,j}, \phi_{i,j}) \quad (5.5)$$

793 These maps are HEALpix maps with NSIDE 16384 and saved in the `.fits` format.

794 Another DM spatial distribution model from Bonnivard ( $\mathcal{B}$ ) [47] was used for the Glory Duck  
795 study. However, to save computational time, limits from  $\mathcal{GS}$  were scaled to  $\mathcal{B}$  instead of each  
796 experiment performing a full study a second time. How these models compare is demonstrated  
797 for each dSph in Figure 5.16 and Figure 5.17 Plots of these maps are provided for each source  
798 in chapter A Examples of the two most impactful dSphs derived from  $\mathcal{GS}$ , Segue1 and Coma  
799 Berenices are featured in Figure 5.3

### 800 5.3.3 Source Selection and Annihilation Channels

801 We use many of the dSphs presented in HAWC’s previous dSph DM search [46]. HAWC’s  
802 sources for Glory Duck include Boötes I, Coma Berenices, Canes Venatici I + II, Draco, Hercules,  
803 Leo I, II, + IV, Segue 1, Sextans, and Ursa Major I + II. A full description of all sources used  
804 in Glory Duck is found in Table 5.1. Triangulum II was excluded from the Glory Duck analysis  
805 because of large uncertainties in its  $J$  factor. Ursa Minor was excluded from HAWC’s contribution  
806 to the combination because the source extension model extended Ursa Minor beyond HAWC’s field  
807 of view. Ursa Minor was not expected to contribute significantly to the combined limit, so work  
808 was not invested in a solution to include Ursa Minor.

809 This analysis improves on the previous HAWC dSph paper [46] in the following ways. Pre-  
810 viously, the dSphs were treated and implemented as point sources. For this analysis, dSphs are  
811 modeled and treated as extended source. The impact of this change with respect to the upper limit  
812 is source dependent and is explored in Section 5.7.2. Previously, the particle physics model used for  
813 gamma-ray spectra from DM annihilation did not have EW corrections where the PPPC includes  
814 them. Finally, the gamma-ray ray dataset is much larger. The study performed here analyzes over  
815 1000 days of data compared to 507.

816 The SM annihilation channels probed for the Glory Duck combination include  $b\bar{b}$ ,  $e\bar{e}$ ,  $\mu\bar{\mu}$ ,  $\tau\bar{\tau}$ ,  
817  $t\bar{t}$ ,  $W^+W^-$ , and  $ZZ$ . A summary of all sources, with a description of each experiments’ sensitivity

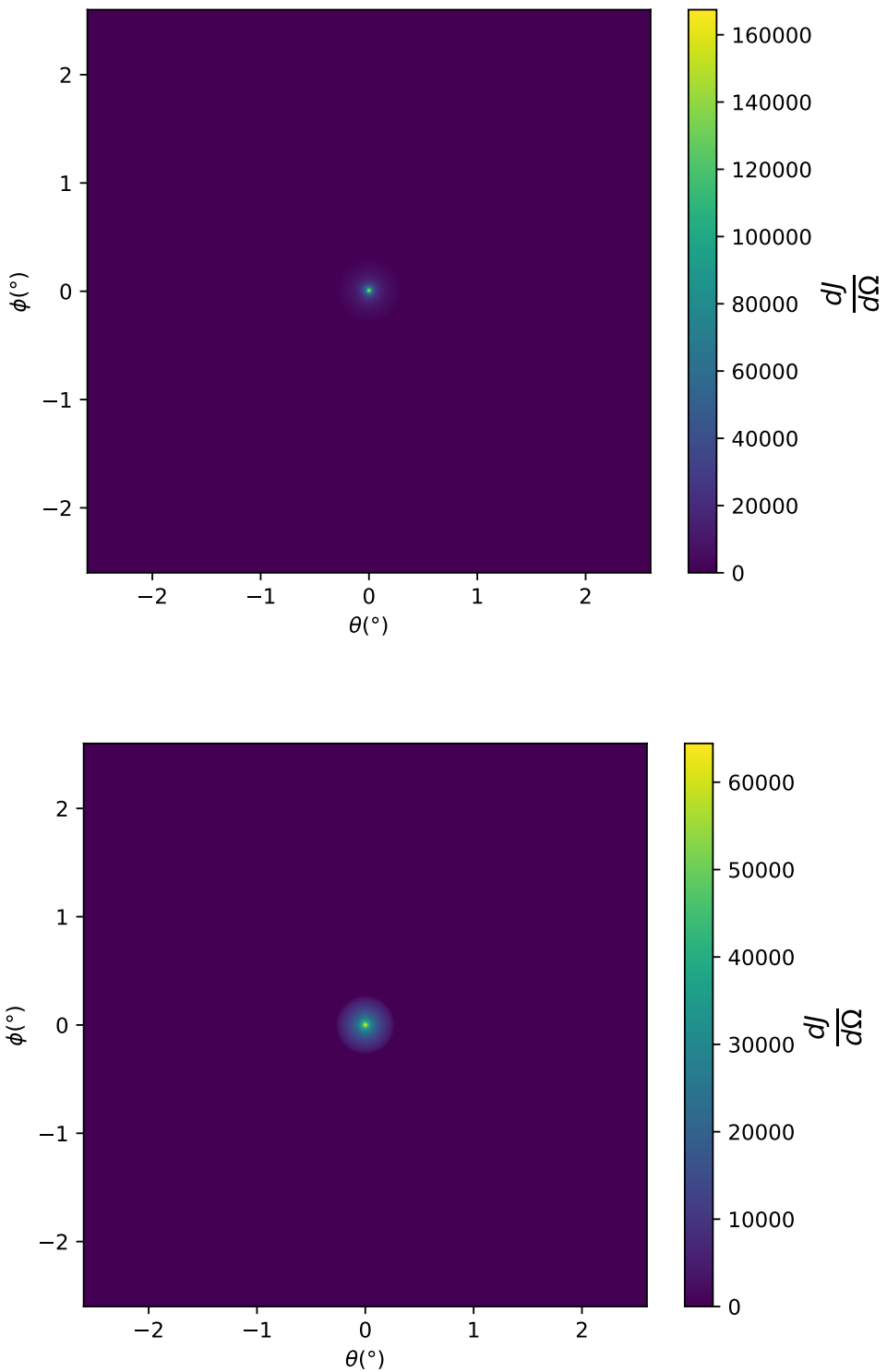


Figure 5.3  $\frac{dJ}{d\Omega}$  maps for Segue1 (top) and Coma Berenices (bottom). Origin is centered on the specific dwarf spheroidal galaxies (dSph). X and Y axes are the angular separation from the center of the dwarf. Plots of the remaining 11 dSph HAWC studied are linked in Fig. A.1.

Table 5.1 Summary of the relevant properties of the dSphs used in the present work. Column 1 lists the dSphs. Columns 2 and 3 present their heliocentric distance and galactic coordinates, respectively. Columns 4 and 5 report the  $J$ -factors of each source given from the  $\mathcal{GS}$  and  $\mathcal{B}$  independent studies and their estimated  $\pm 1\sigma$  uncertainties. The values  $\log_{10} J$  ( $\mathcal{GS}$  set) [45] correspond to the mean  $J$ -factor values for a source extension truncated at the outermost observed star. The values  $\log_{10} J$  ( $\mathcal{B}$  set) [47] are provided for a source extension at the tidal radius of each dSph. **Bolded sources are within HAWC's field of view and provided to the Glory Duck analysis.**

Name	Distance (kpc)	$l, b$ ( $^{\circ}$ )	$\log_{10} J$ ( $\mathcal{GS}$ set) $\log_{10}(\text{GeV}^2\text{cm}^{-5}\text{sr})$	$\log_{10} J$ ( $\mathcal{B}$ set) $\log_{10}(\text{GeV}^2\text{cm}^{-5}\text{sr})$
<b>Boötes I</b>	66	358.08, 69.62	$18.24^{+0.40}_{-0.37}$	$18.85^{+1.10}_{-0.61}$
<b>Canes Venatici I</b>	218	74.31, 79.82	$17.44^{+0.37}_{-0.28}$	$17.63^{+0.50}_{-0.20}$
<b>Canes Venatici II</b>	160	113.58, 82.70	$17.65^{+0.45}_{-0.43}$	$18.67^{+1.54}_{-0.97}$
Carina	105	260.11, -22.22	$17.92^{+0.19}_{-0.11}$	$18.02^{+0.36}_{-0.15}$
<b>Coma Berenices</b>	44	241.89, 83.61	$19.02^{+0.37}_{-0.41}$	$20.13^{+1.56}_{-1.08}$
<b>Draco</b>	76	86.37, 34.72	$19.05^{+0.22}_{-0.21}$	$19.42^{+0.92}_{-0.47}$
Fornax	147	237.10, -65.65	$17.84^{+0.11}_{-0.06}$	$17.85^{+0.11}_{-0.08}$
<b>Hercules</b>	132	28.73, 36.87	$16.86^{+0.74}_{-0.68}$	$17.70^{+1.08}_{-0.73}$
<b>Leo I</b>	254	225.99, 49.11	$17.84^{+0.20}_{-0.16}$	$17.93^{+0.65}_{-0.25}$
<b>Leo II</b>	233	220.17, 67.23	$17.97^{+0.20}_{-0.18}$	$18.11^{+0.71}_{-0.25}$
<b>Leo IV</b>	154	265.44, 56.51	$16.32^{+1.06}_{-1.70}$	$16.36^{+1.44}_{-1.65}$
Leo V	178	261.86, 58.54	$16.37^{+0.94}_{-0.87}$	$16.30^{+1.33}_{-1.16}$
Leo T	417	214.85, 43.66	$17.11^{+0.44}_{-0.39}$	$17.67^{+1.01}_{-0.56}$
Sculptor	86	287.53, -83.16	$18.57^{+0.07}_{-0.05}$	$18.63^{+0.14}_{-0.08}$
<b>Segue I</b>	23	220.48, 50.43	$19.36^{+0.32}_{-0.35}$	$17.52^{+2.54}_{-2.65}$
Segue II	35	149.43, -38.14	$16.21^{+1.06}_{-0.98}$	$19.50^{+1.82}_{-1.48}$
<b>Sextans</b>	86	243.50, 42.27	$17.92^{+0.35}_{-0.29}$	$18.04^{+0.50}_{-0.28}$
<b>Ursa Major I</b>	97	159.43, 54.41	$17.87^{+0.56}_{-0.33}$	$18.84^{+0.97}_{-0.43}$
<b>Ursa Major II</b>	32	152.46, 37.44	$19.42^{+0.44}_{-0.42}$	$20.60^{+1.46}_{-0.95}$
Ursa Minor	76	104.97, 44.80	$18.95^{+0.26}_{-0.18}$	$19.08^{+0.21}_{-0.13}$

818 to the source, is provided in Table 5.2.

## 819 5.4 Likelihood Methods

### 820 5.4.1 HAWC Likelihoods

821 For every analysis bin in energy,  $f_{hit}$  bins (1-9), and location, we can expect  $N$  signal events and  
822  $B$  background events. The expected number of excess signal events from dark matter annihilation,

Table 5.2 Summary of dSph observations by each experiment used in this work. A ‘-’ indicates the experiment did not observe the dSph for this study. For Fermi-LAT, the exposure at 1 GeV is given. For HAWC,  $|\Delta\theta|$  is the absolute difference between the source declination and HAWC latitude. HAWC is more sensitive to sources with smaller  $|\Delta\theta|$ . For IACTs, we show the zenith angle range, the total exposure, the energy range, the angular radius  $\theta$  of the signal or ON region, the ratio of exposures between the background-control (OFF) and signal (ON) regions ( $\tau$ ), and the significance of gamma-ray excess in standard deviations,  $\sigma$ .

Source name	Fermi-LAT	HAWC	H.E.S.S, MAGIC, VERITAS						
	Exposure ( $10^{11}$ s m $^2$ )	$ \Delta\theta $ (°)	IACT	Zenith (°)	Exposure (h)	Energy range (GeV)	$\theta$ (°)	$\tau$	$S$ ( $\sigma$ )
Boötes I	2.6	4.5	VERITAS	15 – 30	14.0	100–41000	0.10	8.6	-1.0
Canes Venatici I	2.9	14.6	–	–	–	–	–	–	–
Canes Venatici II	2.9	15.3	–	–	–	–	–	–	–
Carina	3.1	–	H.E.S.S.	27 – 46	23.7	310 – 70000	0.10	18.0	-0.3
Coma Berenices	2.7	4.9	H.E.S.S.	47 – 49	11.4	550 – 70000	0.10	14.4	-0.4
			MAGIC	5 – 37	49.5	60 – 10000	0.17	1.0	–
			MAGIC	29 – 45	52.1	70 – 10000	0.22	1.0	–
Draco	3.8	38.1	VERITAS	25 – 40	49.8	120 – 70000	0.10	9.0	-1.0
Fornax	2.7	–	H.E.S.S.	11 – 25	6.8	230 – 70000	0.10	45.5	-1.5
Hercules	2.8	6.3	–	–	–	–	–	–	–
Leo I	2.5	6.7	–	–	–	–	–	–	–
Leo II	2.6	3.1	–	–	–	–	–	–	–
Leo IV	2.4	19.5	–	–	–	–	–	–	–
Leo V	2.4	–	–	–	–	–	–	–	–
Leo T	2.6	–	–	–	–	–	–	–	–
Sculptor	2.7	–	H.E.S.S.	10 – 46	11.8	200 – 70000	0.10	19.8	-2.2
Segue I	2.5	2.9	MAGIC	13 – 37	158.0	60 – 10000	0.12	1.0	-0.5
			VERITAS	15 – 35	92.0	80 – 50000	0.10	7.6	0.7
Segue II	2.7	–	–	–	–	–	–	–	–
Sextans	2.4	20.6	–	–	–	–	–	–	–
Ursa Major I	3.4	32.9	–	–	–	–	–	–	–
Ursa Major II	4.0	44.1	MAGIC	35 – 45	94.8	120 – 10000	0.30	1.0	-2.1
Ursa Minor	4.1	–	VERITAS	35 – 45	60.4	160 – 93000	0.10	8.4	-0.1

823  $S$ , is estimated by convolving Equation (7.1) with HAWC's energy response and pixel point spread  
 825 functions. I then compute the test statistic (TS) with the log-likelihood ratio test,

$$\text{TS} = -2 \ln \left( \frac{\mathcal{L}_0}{\mathcal{L}^{\max}} \right) \quad (5.6)$$

826 where  $\mathcal{L}_0$  is the null hypothesis, or no DM emission, likelihood.  $\mathcal{L}^{\max}$  is the best fit signal  
 827 hypothesis where  $\langle \sigma v \rangle$  maximizes the likelihood. We calculate the likelihood of each source and  
 828 model, assuming events are Poisson distributed, with

$$\mathcal{L} = \prod_i \frac{(B_i + S_i)^{N_i} e^{-(B_i + S_i)}}{N_i!} \quad (5.7)$$

829 where  $S_i$  is the sum of expected number of signal counts.  $B_i$  is the number of background counts  
 830 observed.  $N_i$  is the total number of counts.

831 I also calculate an upper limit on  $\langle \sigma v \rangle$  by calculating the 95% confidence level (CL). For the  
 832 CL, we define a parameter,  $\text{TS}_{95}$ , as

$$\text{TS}_{95} \equiv \sum_{\text{bins}} \left[ 2N \ln \left( 1 + \frac{\epsilon S_{\text{ref}}}{B} \right) - 2\epsilon S_{\text{ref}} \right] \quad (5.8)$$

833 where the expected signal counts from a dSph is scaled by  $\epsilon$ .  $S_{\text{ref}}$  is the expected number of excess  
 834 counts in a bin from DM emission from a dSph with a corresponding annihilation cross-section,  
 835  $\langle \sigma v \rangle$ . We scan  $\epsilon$  such that

$$2.71 = \text{TS}_{\max} - \text{TS}_{95} \quad (5.9)$$

### 836 5.4.2 Glory Duck Joint Likelihood

837 The joint likelihood for the 5-experiment combination was done similarly as Section 5.4.1. We  
 838 calculate upper limits on  $\langle \sigma v \rangle$  from the TS, Eq. (5.6), and define the likelihood ratio more generally

$$\lambda(\langle \sigma v \rangle | \mathcal{D}_{\text{dSphs}}) = \frac{\mathcal{L}(\langle \sigma v \rangle; \hat{\nu} | \mathcal{D}_{\text{dSphs}})}{\mathcal{L}(\widehat{\langle \sigma v \rangle}; \hat{\nu} | \mathcal{D}_{\text{dSphs}})} \quad (5.10)$$

839  $\mathcal{D}_{\text{dSphs}}$  is the totality of observations across experiments and dSphs.  $\nu$  are the nuisance parameters  
 840 which are the  $J$  factors in this study.  $\widehat{\langle \sigma v \rangle}$  and  $\hat{\nu}$  are the respective estimate that maximize  $\mathcal{L}$   
 841 globally. Finally,  $\hat{\nu}$  is the set of nuisance parameters that maximize  $\mathcal{L}$  for a fixed value of  $\langle \sigma v \rangle$ .

842 The *complete* joint likelihood,  $\mathcal{L}$  that encompasses all observations from all instruments and  
 843 dSphs can be factorized into *partial* functions for each dSph  $l$  (with  $\mathcal{L}_{\text{dSph},l}$ ) and its  $J$  factor ( $\mathcal{J}_l$ ):

$$\mathcal{L}(\langle\sigma v\rangle; \nu | \mathcal{D}_{\text{dSphs}}) = \prod_{l=1}^{N_{\text{dSphs}}} \mathcal{L}_{\text{dSph},l}(\langle\sigma v\rangle; J_l, \nu_l | \mathcal{D}_l) \times \mathcal{J}_l(J_l | J_{l,\text{obs}}, \sigma_{\log J_l}). \quad (5.11)$$

844 For this study,  $N_{\text{dSphs}} = 20$  is the number of dSphs studied.  $\mathcal{D}_l$  are the gamma-ray observations  
 845 of dSph,  $l$ .  $\nu_l$  are the nuisance parameters modifying the gamma-ray observations of dSph,  $l$ ,  
 846 but excludes  $\mathcal{J}_l$ .  $\mathcal{J}_l$  is the  $J$  factor for dSph,  $l$ , as defined in Equation (5.2), and it is a nuisance  
 847 parameter whose value is unknown.  $\log_{10} J_{l,\text{obs}}$  and  $\sigma_{\log J_l}$  are obtained from fitting a log-normal  
 848 function of  $J_{l,\text{obs}}$  to the posterior distribution of  $J_l$  [48].  $\log_{10} J_{l,\text{obs}}$  and  $\sigma_{\log J_l}$  values are provided  
 849 in Table 5.1. The term  $\mathcal{J}_l$  constraining  $J_l$  is written as:

$$\mathcal{J}_l(J_l | J_{l,\text{obs}}, \sigma_{\log J_l}) = \frac{1}{\ln(10)J_{l,\text{obs}}\sqrt{2\pi}\sigma_{\log J_l}} \exp\left(-\frac{(\log_{10} J_l - \log_{10} J_{l,\text{obs}})^2}{2\sigma_{\log J_l}^2}\right). \quad (5.12)$$

850 Both the  $\mathcal{GS}$  and  $\mathcal{B}$ , displayed in Table 5.1, sets of  $J$  factors are used in this analysis. Equation (5.12)  
 851 is also normalized, so it can also be interpreted as a probability density function (PDF) for  $J_{l,\text{obs}}$ .  
 852 From Equation (7.1), we can also see that  $\langle\sigma v\rangle$  and  $J_l$  are degenerate when computing  $\mathcal{L}_{\text{dSph},l}$ .  
 853 Therefore, as noted in [49], it is sufficient to compute  $\mathcal{L}_{\text{dSph},l}$  versus  $\langle\sigma v\rangle$  for a fixed value of  $J_l$ .  
 854 We used  $J_{l,\text{obs}}(\mathcal{GS})$  reported in Tab. 5.1, in order to perform the profile of  $\mathcal{L}$  with respect to  $J_l$ .  
 855 The degeneracy implies that for any  $J'_l \neq J_{l,\text{obs}}$  (in practice in our case we used  $J'_l = J_{l,\text{obs}}(\mathcal{B})$  to  
 856 compute results from a different set of  $J$  factors):

$$\mathcal{L}_{\text{dSph},l}(\langle\sigma v\rangle; J'_l, \nu_l | \mathcal{D}_l) = \mathcal{L}_{\text{dSph},l}\left(\frac{J'_l}{J_{l,\text{obs}}}\langle\sigma v\rangle; J_{l,\text{obs}}, \nu_l | \mathcal{D}_l\right), \quad (5.13)$$

857 which is a straightforward rescaling operation that reduces the computational needs of the profiling  
 858 operation since:

$$\mathcal{L}(\langle\sigma v\rangle; \hat{\nu} | \mathcal{D}_{\text{dSphs}}) = \prod_{l=1}^{N_{\text{dSphs}}} \max_{J_l} \left[ \mathcal{L}_{\text{dSph},l}(\langle\sigma v\rangle; J_l, \hat{\nu}_l | \mathcal{D}_l) \times \mathcal{J}_l(J_l | J_{l,\text{obs}}, \sigma_{\log J_l}) \right]. \quad (5.14)$$

859 In addition, Eq. (5.13) enables the combination of data from different gamma-ray instruments and  
 860 observed dSphs via tabulated values of  $\mathcal{L}_{\text{dSph},l}$ , or equivalently of  $\lambda$  from Eq. (5.10) as was done in

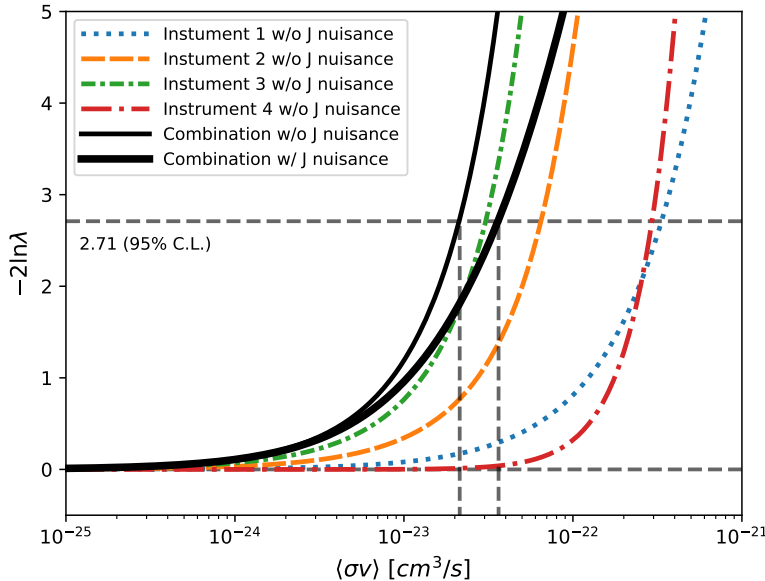


Figure 5.4 Illustration of the combination technique showing a comparison between  $-2 \ln \lambda$  provided by four instruments (colored lines) from the observation of the same dSph without any  $J$  nuisance and their sum, *i.e.* the resulting combined likelihood (thin black line). According to the test statistics of Equation (5.6), the intersection of the likelihood profiles with the line  $-2 \ln \lambda = 2.71$  indicates the 95% C.L. upper limit on  $\langle \sigma v \rangle$ . The combined likelihood (thin black line) shows a smaller value of upper limit on  $\langle \sigma v \rangle$  than those derived by individual instruments. We also show how the uncertainties on the  $J$  factor effects the combined likelihood and degrade the upper limit on  $\langle \sigma v \rangle$  (thick black line). All likelihood profiles are normalized so that the global minimum  $\widehat{\langle \sigma v \rangle}$  is 0. We note that each profile depends on the observational conditions in which a target object was observed. The sensitivity of a given instrument can be degraded and the upper limits less constraining if the observations are performed in non-optimal conditions such as a high zenith angle or a short exposure time.

861 this work, versus  $\langle \sigma v \rangle$ .  $\mathcal{L}_{\text{dSph},l}$  is computed for a fixed value of  $J_l$  and profiled with respect to all  
 862 instrumental nuisance parameters  $\nu_l$ , these nuisance parameters are discussed in more detail below.  
 863 These values are produced by each detector independently and therefore there is no need to share  
 864 sensitive low-level information used to produce them, such as event lists. Figure 5.4 illustrates the  
 865 multi-instrument combination technique used in this study with a comparison of the upper limit  
 866 on  $\langle \sigma v \rangle$  obtained from the combination of the observations of four experiments towards one dSph  
 867 versus the upper limit from individual instruments. It also shows graphically the effect of the  
 868  $J$ -factor uncertainty on the combined observations.

869 The *partial* joint likelihood function for gamma-ray observations of each dSph ( $\mathcal{L}_{\text{dSph},l}$ ) is

written as the product of the likelihood terms describing the  $N_{\text{exp},l}$  observations performed with any of our observatories:

$$\mathcal{L}_{\text{dSph},l} (\langle \sigma v \rangle; J_l, \nu_l | \mathcal{D}_l) = \prod_{k=1}^{N_{\text{exp},l}} \mathcal{L}_{lk} (\langle \sigma v \rangle; J_l, \nu_{lk} | \mathcal{D}_{lk}), \quad (5.15)$$

where each  $\mathcal{L}_{lk}$  term refers to an observation of the  $l$ -th dSph with associated  $k$ -th instrument responses.  $N_{\text{exp},l}$  varies from dSph to dSph and can be inferred from Table 5.2.

Each collaboration separately analyzes their data for  $\mathcal{D}_{lk}$  corresponding to dSph  $l$  and gamma-ray detector  $k$ , using as many common assumptions as possible in the analysis. HAWC’s treatment was described earlier in Section 5.4.1 whereas the specifics of the remaining experiments is left to the publication. We compute the values for the likelihood functions  $\mathcal{L}_{lk}$  (see Eq. (5.15)) for a fixed value of  $J_l$  and profile over the rest of the nuisance parameters  $\nu_{lk}$ . Then, values of  $\lambda$  from Eq. (5.10) are computed as a function of  $\langle \sigma v \rangle$ , and shared using a common format. Results are computed for seven annihilation channels,  $W^+W^-$ ,  $ZZ$ ,  $b\bar{b}$ ,  $t\bar{t}$ ,  $e^+e^-$ ,  $\mu^+\mu^-$ , and  $\tau^+\tau^-$  over 62  $m_\chi$  values between 5 GeV and 100 TeV provided in [44]. The  $\langle \sigma v \rangle$  range is defined between  $10^{-28}$  and  $10^{-18} \text{cm}^3 \cdot \text{s}^{-1}$ , with 1001 logarithmically spaced values. The likelihood combination, i.e. Equation (5.11), and profile over the  $J$ -factor to compute the profile likelihood ratio  $\lambda$ , Equation (5.10), are carried out with two different public analysis software packages, namely `gLike` [50] and `LklCom` [51], that provide the same results [52].

As mentioned previously, each experiment computes the  $\mathcal{L}_{lk}$  from Equation (5.10) differently. The remainder of this section highlights the differences in this calculation across the experiments. Four experiments, namely *Fermi*-LAT, H.E.S.S., HAWC and MAGIC, use a binned likelihood to compute the  $\mathcal{L}_{lk}$ . For these experiments, for each observation  $\mathcal{D}_{lk}$  of a given dSph  $l$  carried out using a given gamma-ray detector  $k$ , the binned likelihood function is:

$$\mathcal{L}_{lk} (\langle \sigma v \rangle; J_l, \nu_{lk} | \mathcal{D}_{lk}) = \prod_{i=1}^{N_E} \prod_{j=1}^{N_P} \left[ \mathcal{P}(s_{lk,ij}(\langle \sigma v \rangle, J_l, \nu_{lk}) + b_{lk,ij}(\nu_{lk}) | N_{lk,ij}) \right] \times \mathcal{L}_{lk,\nu} (\nu_{lk} | \mathcal{D}_{\nu_{lk}}) \quad (5.16)$$

where  $N_E$  and  $N_P$  are the number of considered bins in reconstructed energy and arrival direction, respectively;  $\mathcal{P}$  represents a Poisson PDF for the number of gamma-ray candidate events  $N_{lk,ij}$

893 observed in the  $i$ -th bin in energy and  $j$ -th bin in arrival direction, when the expected number is  
 894 the sum of the expected mean number of signal events  $s_{ij}$  (produced by DM annihilation) and of  
 895 background events  $b_{ij}$ ;  $\mathcal{L}_{lk,\nu}$  is the likelihood term for the extra  $\nu_{lk}$  nuisance parameters that vary  
 896 from one instrument  $k$  to another. The expected counts for signal events  $s_{ij}$  for a given dSph  $l$  and  
 897 detector  $k$  is given by:

$$s_{ij}(\langle\sigma\nu\rangle, J) = \int_{E'_{\min,i}}^{E'_{\max,i}} dE' \int_{P'_{\min,j}}^{P'_{\max,j}} d\Omega' \int_0^\infty dE \int_{\Delta\Omega_{tot}} d\Omega \int_0^{T_{\text{obs}}} dt \frac{d^2\Phi(\langle\sigma\nu\rangle, J)}{dEd\Omega} \text{IRF}(E', P' | E, P, t) \quad (5.17)$$

898 where  $E'$  and  $E$  are the reconstructed and true energies,  $P'$  and  $P$  the reconstructed and true  
 899 arrival directions;  $E'_{\min,i}$ ,  $P'_{\min,j}$ ,  $E'_{\max,i}$ , and  $P'_{\max,j}$  are their lower and upper limits of the  $i$ -th  
 900 energy bin and the  $j$ -th arrival direction bin;  $T_{\text{obs}}$  is the (dead-time corrected) total observation  
 901 time;  $t$  is the time along the observations;  $d^2\Phi/dEd\Omega$  is the DM flux in the source region (see  
 902 Equation (7.1)); and  $\text{IRF}(E', P' | E, P, t)$  is the IRF, which can be factorized as the product of the  
 903 effective collection area of the detector  $A_{\text{eff}}(E, P, t)$ , the PDFs for the energy estimator  $f_E(E' | E, t)$ ,  
 904 and arrival direction  $f_P(P' | E, P, t)$  estimators. Note that for Fermi-LAT, HAWC, MAGIC, and  
 905 VERITAS the effect of the finite angular resolution is taken into account through the convolution  
 906 of  $d\Phi/dEd\Omega$  with  $f_P$  in Equation (5.17), whereas in the cases of H.E.S.S.  $f_P$  is approximated by a  
 907 delta function. This approximation has been made in order to maintain compatibility of the result  
 908 with what has been previously published. The difference introduced by this approximation is  $< 5\%$   
 909 for all considered dSphs. A more comprehensive review of the differences between the analyses of  
 910 different instruments can be found in [25].

## 911 5.5 HAWC Results

912 13 of the 20 dSphs considered for the Glory Duck analysis are within HAWC's field of view.  
 913 These dSph are analyzed for emission from DM annihilation according to the likelihood method  
 914 described in Section 5.4. The 13 likelihood profiles are then stacked to synthesize a combined  
 915 limit on the dark matter cross-section,  $\langle\sigma\nu\rangle$ . This combination is done for the 7 SM annihilation  
 916 channels used in the Glory Duck analysis. Figure 5.5 shows the combined limit for all annihilation  
 917 channels with HAWC only observations. We also perform 300 studies of Poisson trials on the

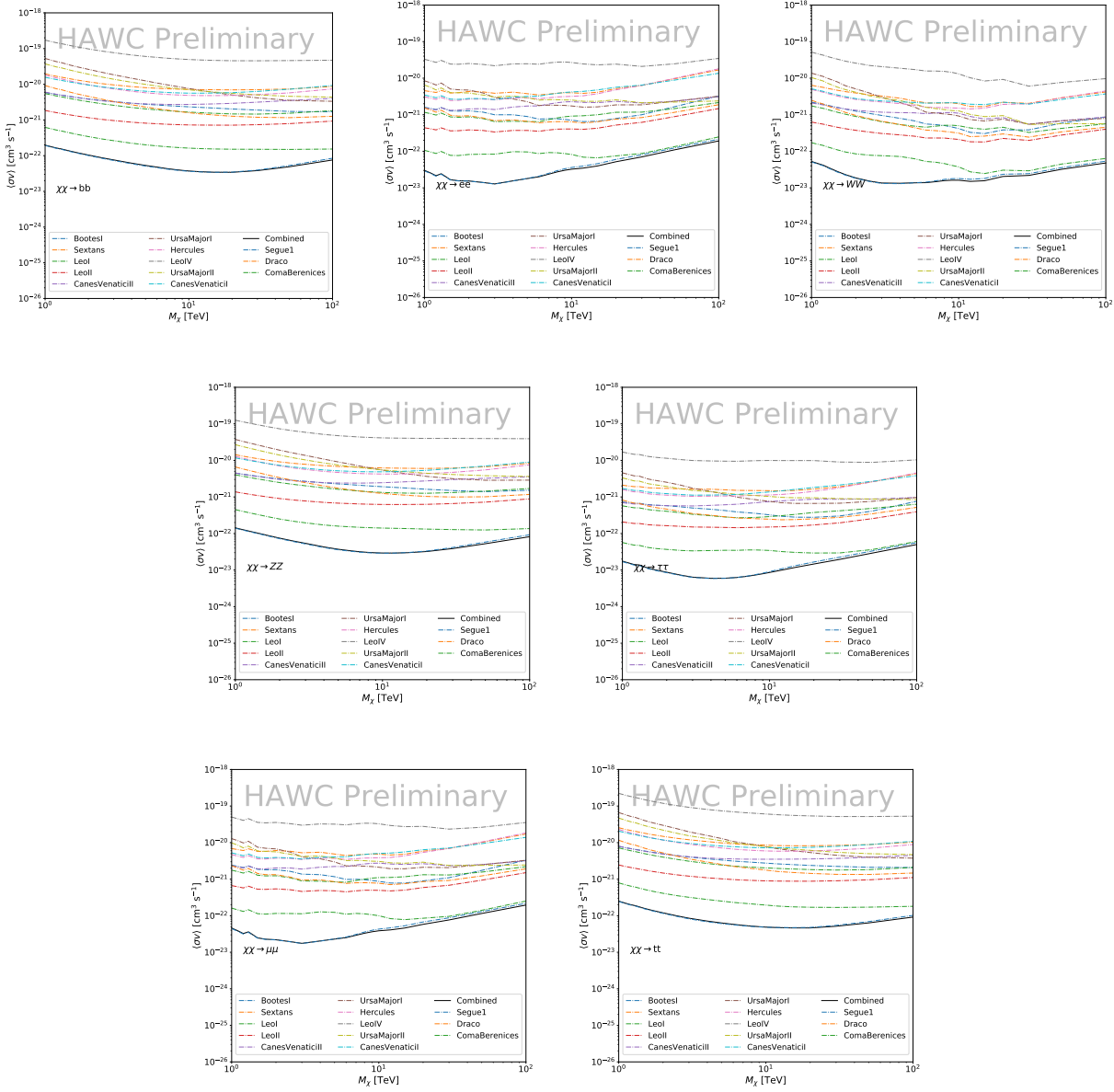


Figure 5.5

background. These trials are used to produce HAWC Brazil bands which were shared with the other collaborators for combined Brazil Bands. The results on fitting to HAWC's Poisson trials of the DM hypothesis is shown in Figure 5.7 for all the DM annihilation channels studied for Glory Duck.

No DM was found in HAWC observations. HAWC's limits are dominated by the dSphs Segue1 and Coma Berenices. The remaining 11 dSphs do not contribute significantly to the limit because

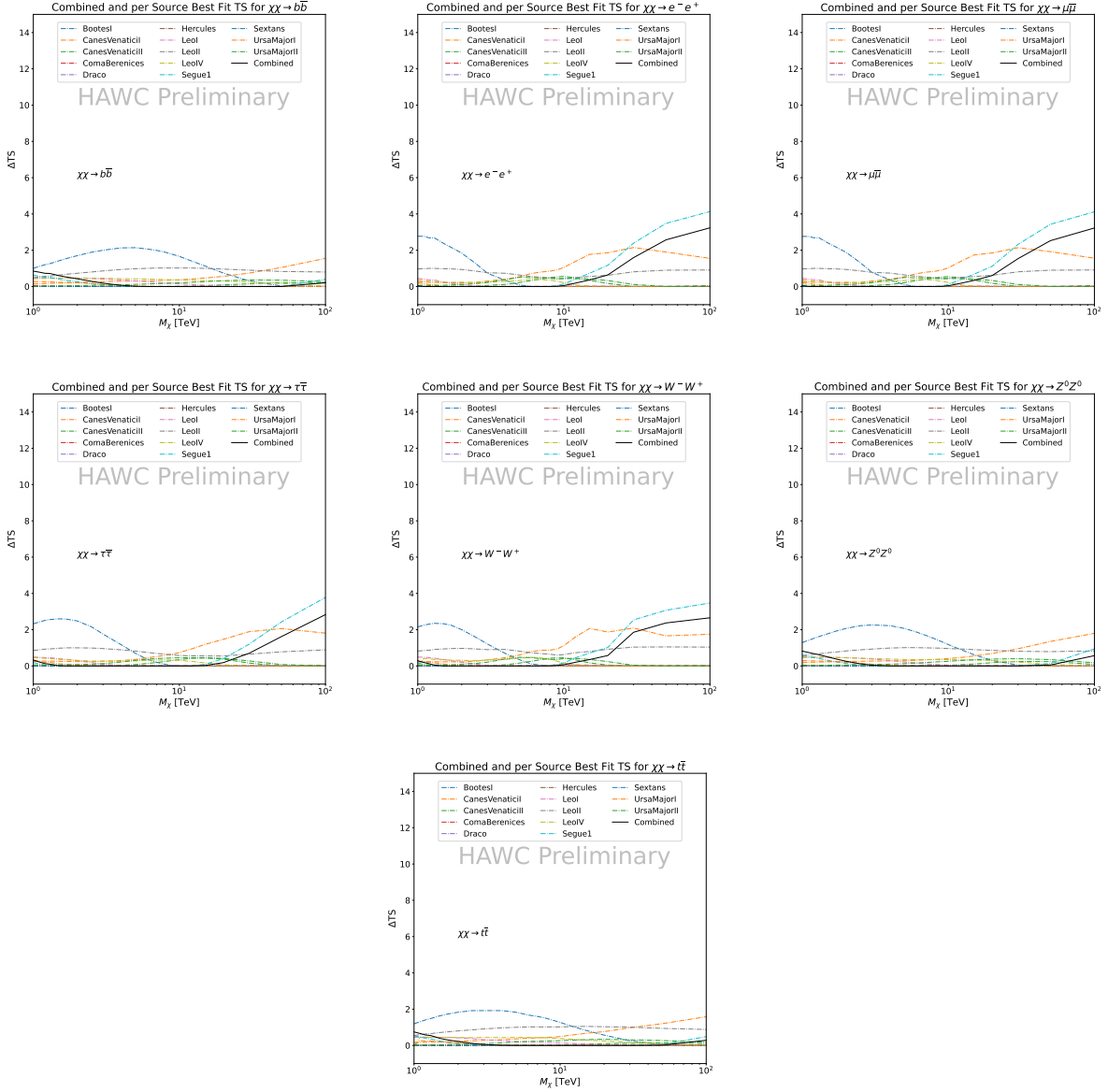


Figure 5.6 HAWC TS values for best fit  $\langle \sigma v \rangle$  versus  $m_\chi$  for seven SM annihilation channels with  $J$  factors from  $\mathcal{GS}$ . The solid black line shows the combined best fit TS values. The colored, dashed lines are the TS values for each of the 13 sources HAWC studied.

924 they are at high zenith and/or have much smaller  $J$  factors. Even though some remaining dSphs  
 925 have large  $J$  factors, they are towards the edge of HAWC's field of view where HAWC analysis is  
 926 less sensitive.

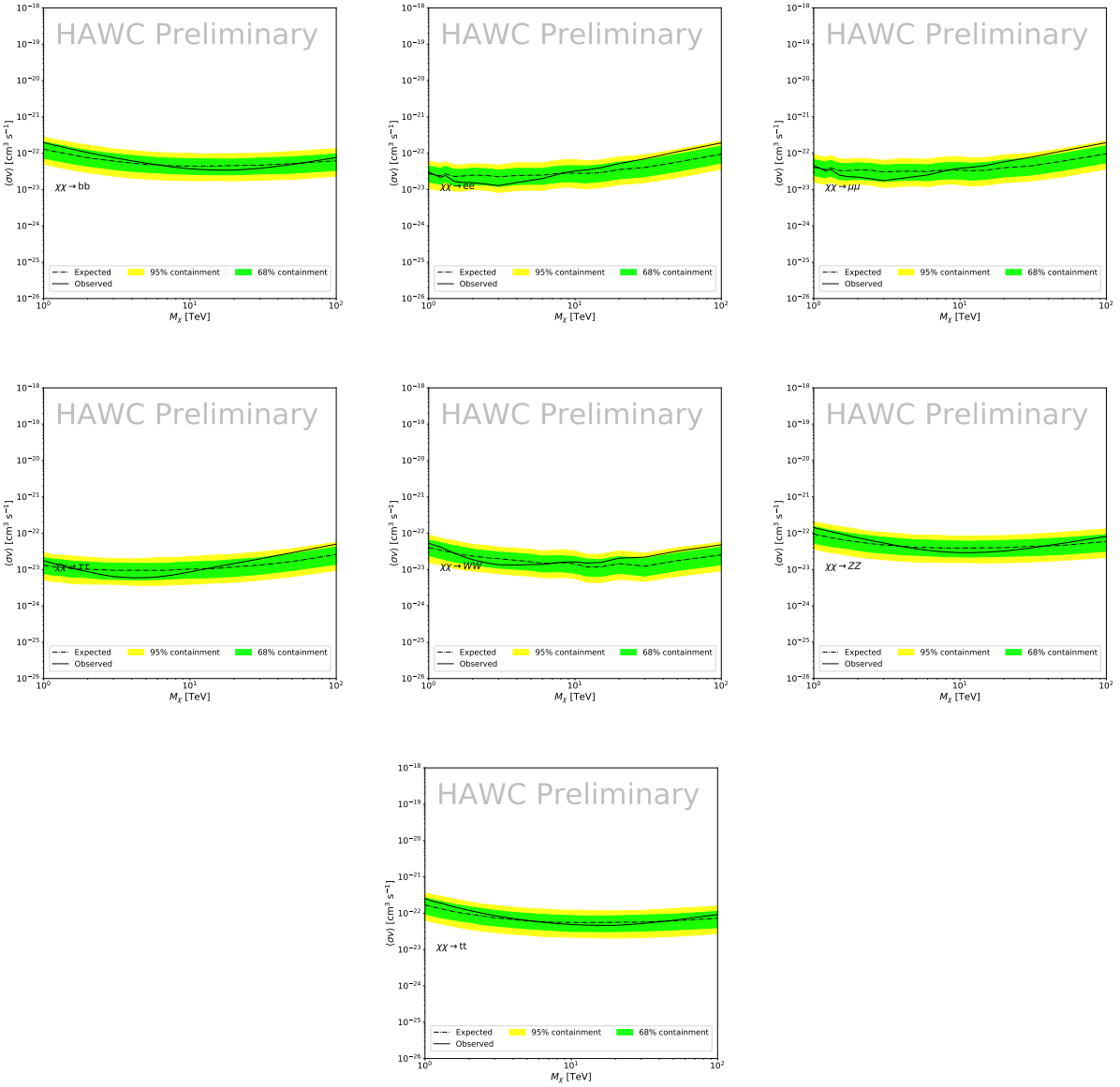


Figure 5.7 HAWC Brazil bands at 95% confidence level on  $\langle\sigma v\rangle$  versus DM mass for seven annihilation channels with  $J$ -factors from GS [53]. The solid line represents the combined limit from 13 dSphs. The dashed line is the expected limit. The green band is the 68% containment. The yellow band is the 95% containment.

## 927 5.6 Glory Duck Combined Results

928 The crux of this analysis is that HAWC's results are combined with 4 other gamma-ray observa-  
 929 tories: Fermi-LAT, H.E.S.S., MAGIC, and VERITAS. No significant DM emission was observed  
 930 by any of the five instruments. We present the upper limits on  $\langle\sigma v\rangle$  assuming seven independent  
 931 DM self annihilation channels, namely  $W^+W^-$ ,  $Z^+Z^-$ ,  $b\bar{b}$ ,  $t\bar{t}$ ,  $e^+e^-$ ,  $\mu^+\mu^-$ , and  $\tau^+\tau^-$ . The 68%

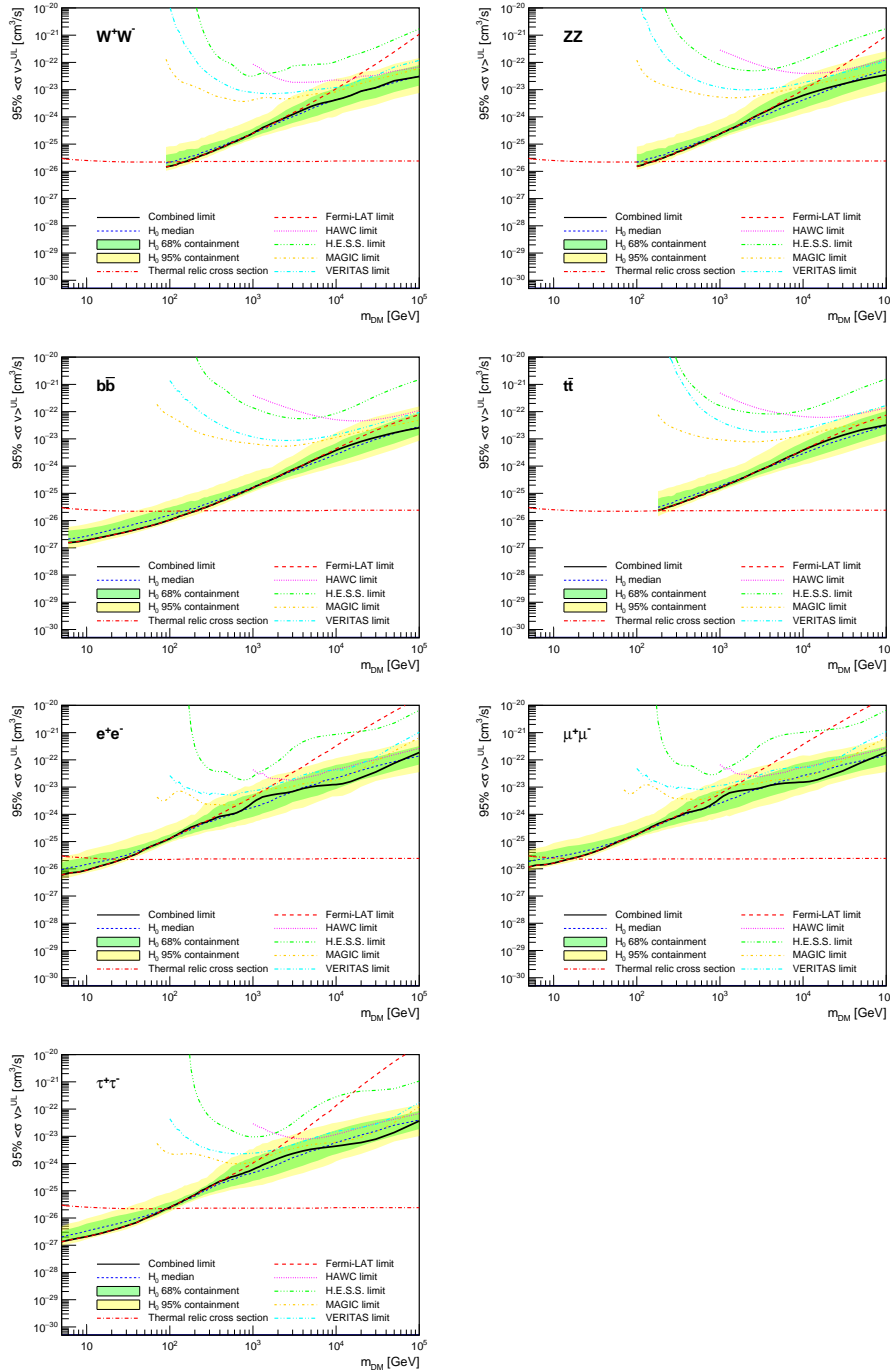


Figure 5.8 Upper limits at 95% confidence level on  $\langle\sigma v\rangle$  in function of the DM mass for eight annihilation channels, using the set of  $J$  factors from Ref. [53] ( $\mathcal{GS}$  set in Table 5.1). The black solid line represents the observed combined limit, the black dashed line is the median of the null hypothesis corresponding to the expected limit, while the green and yellow bands show the 68% and 95% containment bands. Combined upper limits for each individual detector are also indicated as solid, colored lines. The value of the thermal relic cross-section in function of the DM mass is given as the red dotted-dashed line [54].

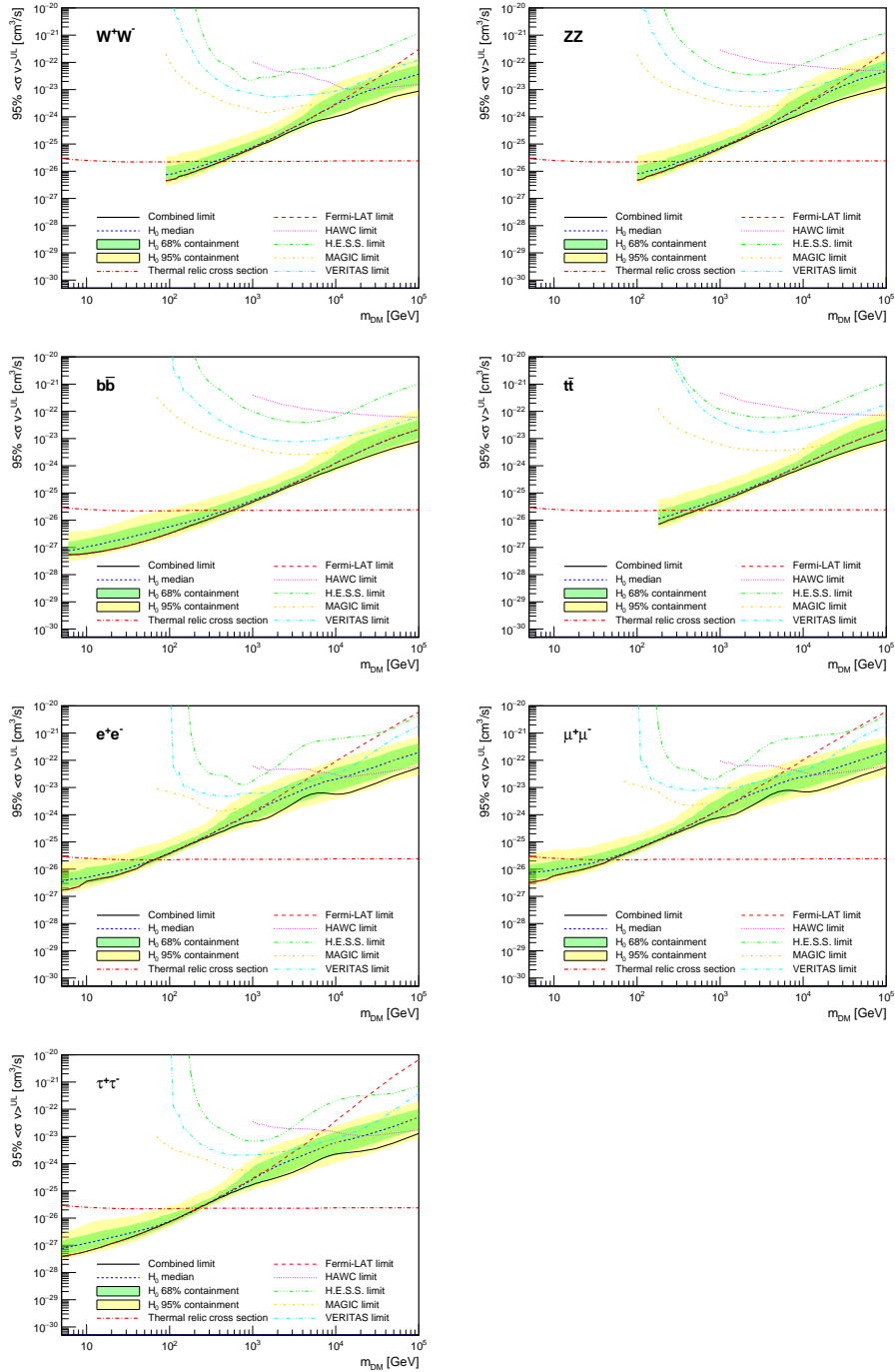


Figure 5.9 Same as Fig. 5.8, using the set of  $J$  factors from Ref. [47, 55] ( $\mathcal{B}$  set in Table 5.1).

and 95% containment bands are produced from 300 Poisson realizations of the null hypothesis corresponding to each of the combined datasets. These 300 realizations are combined identically to dSph observations. The containment bands and the median are extracted from the distribution of resulting limits on the null hypothesis. These 300 realizations are obtained either by fast simu-

936 lations of the OFF observations, for H.E.S.S., MAGIC, VERITAS, and HAWC, or taken from real  
937 observations of empty fields of view in the case of Fermi-LAT [48, 56, 57].

938 The obtained limits are shown in Figure 5.8 for the  $\mathcal{G}\mathcal{S}$  set of  $J$ -factors [53] and in Figure 5.9  
939 for the  $\mathcal{B}$  set of  $J$ -factors [47, 55]. The combined limits are presented with their 68% and 95%  
940 containment bands, and are expected to be close to the median limit when no signal is present.  
941 We observe agreement with the null hypothesis for all channels, within  $2\sigma$  standard deviations,  
942 between the observed limits and the expectations given by the median limits. Limits obtained from  
943 each detector are also indicated in the figures, where limits for all dSphs observed by the specific  
944 instrument have been combined.

945 Below  $\sim 300$  GeV, the *Fermi*-LAT dominates the DM limits for all annihilation channels. From  
946  $\sim 300$  GeV to  $\sim 2$  TeV, *Fermi*-LAT continues to dominate for the hadronic and bosonic DM channels,  
947 yet the IACTs (H.E.S.S., MAGIC, and VERITAS) and *Fermi*-LAT all contribute to the limit for  
948 leptonic DM channels. For DM masses between  $\sim 2$  TeV to  $\sim 10$  TeV, the IACTs dominate leptonic  
949 DM annihilation channels, whereas both the *Fermi*-LAT and the IACTs dominate bosonic and  
950 hadronic DM annihilation channels. From  $\sim 10$  TeV to  $\sim 100$  TeV, both the IACTs and HAWC  
951 contribute significantly to the leptonic DM limit. For hadronic and bosonic DM, the IACTs and  
952 *Fermi*-LAT both contribute strongly.

953 We notice that the limits computed using the  $\mathcal{B}$  set of  $J$ -factor are always better compared to the  
954 ones calculated with the  $\mathcal{G}\mathcal{S}$  set. For the  $W^+W^-$ ,  $Z^+Z^-$ ,  $b\bar{b}$ , and  $t\bar{t}$  channels, the ratio between the  
955 limits computed with the two sets of  $J$ -factor is varying between a factor of  $\sim 3$  and  $\sim 5$  depending  
956 on the energy, with the largest ratio around 10 TeV. For the channels  $e^+e^-$ ,  $\mu^+\mu^-$ , and  $\tau^+\tau^-$ , the  
957 ratio lies between  $\sim 2$  to  $\sim 6$ , being maximum around 1 TeV. Examining Figure 5.16 and Figure 5.17  
958 in Section 5.8, these differences are explained by the fact that the  $\mathcal{B}$  set provides higher  $J$ -factors  
959 for the majority of the studied dSphs, with the notable exception of Segue I. The variation on the  
960 ratio of the limits for the two sets is due to different dSph dominating the limits depending on the  
961 energy. This pushes the range of thermal cross-section which can be excluded to higher mass. This  
962 comparison demonstrates the magnitude of systematic uncertainties associated with the choice of

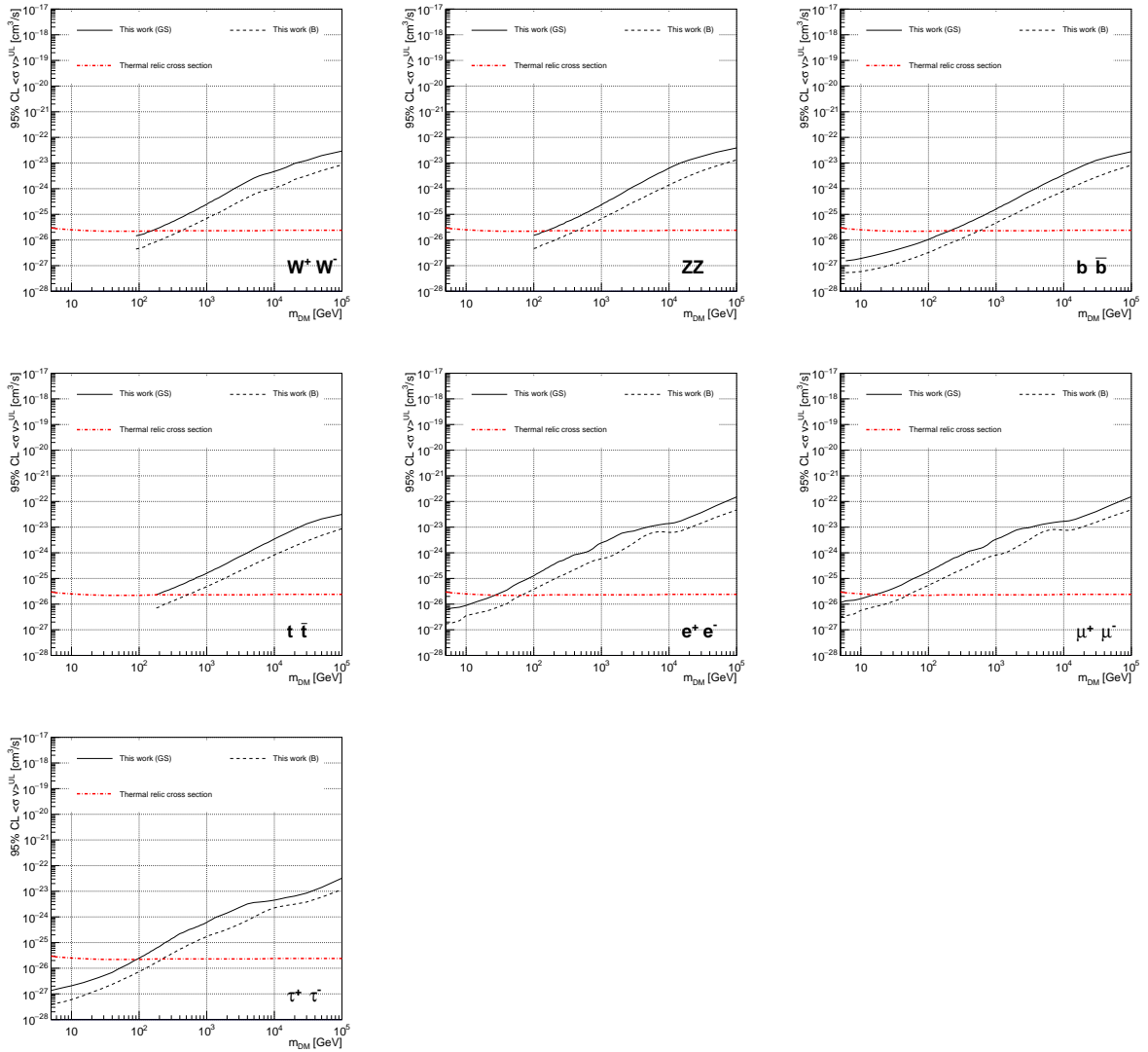


Figure 5.10 Comparisons of the combined limits at 95% confidence level for each of the eight annihilation channels when using the  $J$  factors from Ref. [53] ( $\mathcal{GS}$  set in Table 5.1), plain lines, and the  $J$  factor from Ref. [47, 55] ( $\mathcal{B}$  set in Table 5.1), dashed lines. The cross-section given by the thermal relic is also indicated [54].

### 963 the $J$ -factor

964 This comparison demonstrates the magnitude of systematic uncertainties associated with the  
 965 choice of the  $J$ -factor calculation. The  $\mathcal{GS}$  and  $\mathcal{B}$  sets present a difference in the limits for all  
 966 channels of about This difference is explained, see Figure 5.16 and Figure 5.17 in Appendix, by the  
 967 fact that the  $\mathcal{B}$  set provides higher  $J$  factors for all dSph except for Segue I. This pushes the range  
 968 of thermal cross-section which can be excluded to higher mass.

969 **5.7 HAWC Systematics**

970 **5.7.1 Inverse Compton Scattering**

971       The DM-DM annihilation channels produce many high energy electrons regardless of the  
972 primary annihilation channel. These high energy electrons can produce high energy gamma-rays  
973 through Inverse Compton Scattering (ICS). If this effect is strong, it would change the morphology  
974 of the source and increase the total expected gamma-ray counts from any source. The PPPC [44]  
975 provides tools in Mathematica for calculating the impact of ICS for an arbitrary location in the  
976 sky for a specified annihilation channel. We calculated the change in gamma-ray counts for DM  
977 annihilation to primary  $e\bar{e}$  for RA and Dec corresponding to Segue1 and Coma Berenices. These  
978 dSphs were chosen because they are the strongest contributors to the limit.  $e\bar{e}$  was selected because  
979 it would have the largest number of high energy electrons. The effect was found to be on the order  
980 of  $10^{-7}$  on the gamma-ray spectrum. As a result, this systematic is not considered in our analysis.

981 **5.7.2 Point Source Versus Extended Source Limits**

982       The previous DM search toward dSph approximated the dSphs as point sources [46]. In  
983 this analysis, the dSphs are implemented as extended with J-factor distributions following those  
984 produced by [53]. The resolution of the cited map is much finer than HAWC's angular resolution.  
985 The vast majority of the J-factor distribution is represented on the central HAWC pixel of the dSph  
986 spatial map. However, the neighboring 8 pixels are not negligible and contribute to our limit.

987       Figure 5.11 shows a substantial improvement to the limit for Segue1. Fig. 5.12 however showed  
988 identical limits. These disparities are best explained by the relative difference in their J-Factors.  
989 Both dSphs pass almost overhead the HAWC detector, however Segue1 has the larger J-Factor  
990 between the two. Adjacent pixels to the central pixel will therefore contribute to the limits. This is  
991 the case for other dSph that are closer to overhead the HAWC detector.

992       Comparison plots for all sources and the combined limit can be found in the sandbox for the  
993 Glory Duck project.

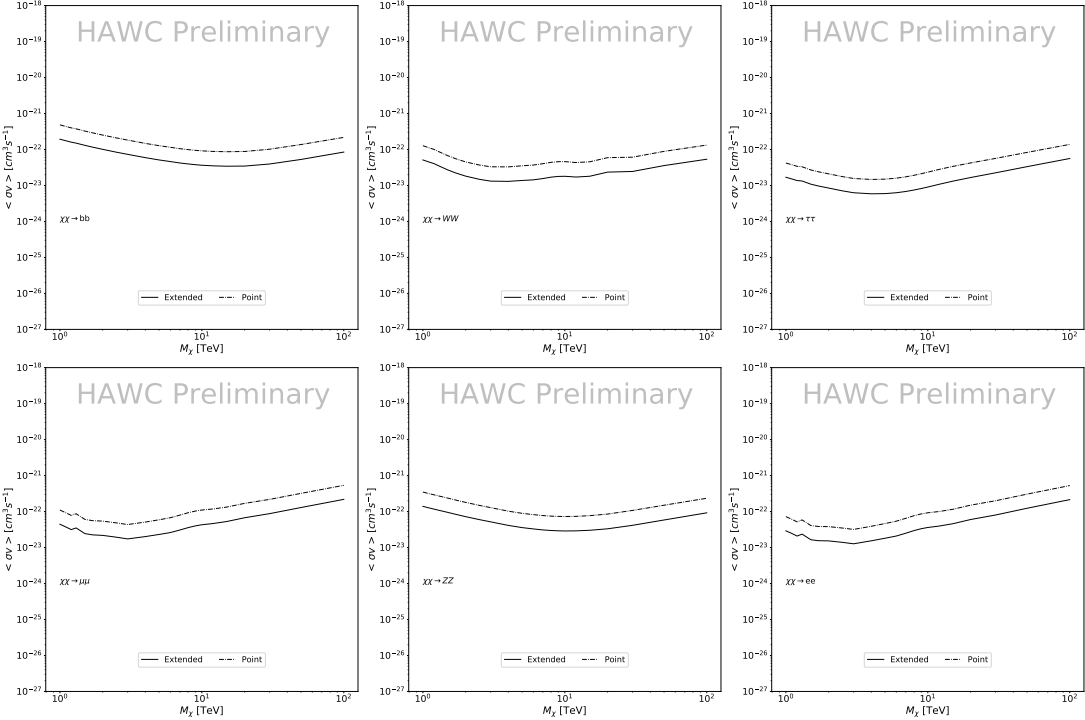


Figure 5.11 Comparisons of the combined limits at 95% confidence level for a point source analysis and extended source using [53]  $\mathcal{GS}$  J-factor distributions and PPPC [44] annihilation spectra. Shown are the limits for Segue1 which will have the most significant impact on the combined limit. 6 of the 7 DM annihilation channels are shown. Solid lines are extended source studies. Dashed lines are point source studies. Overall, the extended source analysis improves the limit by a factor of 2.

### 994 5.7.3 Impact of Pointing Systematic

995 During the analysis it was discovered that reconstruction of gamma-rays. Slides describing this  
 996 systematic can be found [here](#). Shown on the presentation is dependence on the pointing systematic  
 997 on declination. New spatial profiles were generated for every dSph and limits were computed for  
 998 the adjusted declination.

999 Section 5.7.3 demonstrates the impact of this systematic for all DM annihilation channels  
 1000 studied by HAWC. The impact is a tiny improvement, yet mostly identical, to the combined limits.

## 1001 5.8 J-factor distributions

### 1002 5.8.1 Numerical integration of $\mathcal{GS}$ maps

1003 It was discovered well after the HAWC analysis was completed that the published tables from  
 1004  $\mathcal{GS}$  [45] quoted median J-factors were computed in a non-trivial manner. The assumption myself

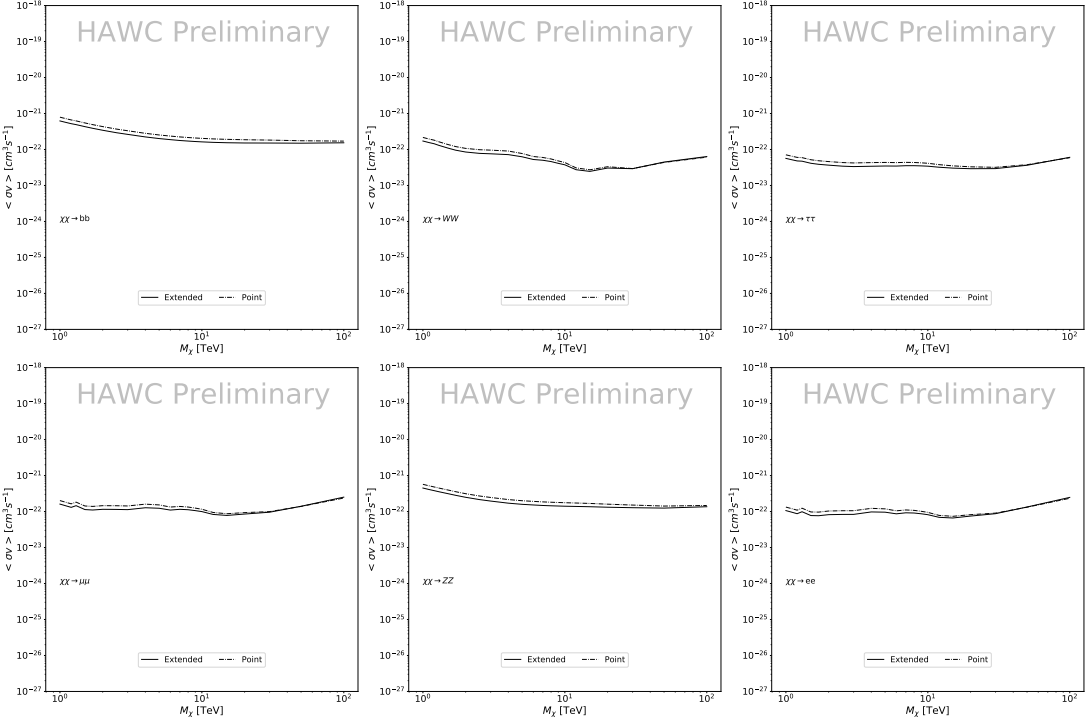


Figure 5.12 Same as Fig. 5.11 on Coma Berenices. This dSph also contributes significantly to the limit. The limits are identical in this case.

and collaborators had been that the published tables represented the  $J$ -factor as a function of  $\theta$  for the best global fit model on a per-source basis. However, this is not the case. Instead, what is published are the best fit model for each dwarf that only considers stars up to the angular separation  $\theta$ . Therefore, the model is changing for each value of  $\theta$  for each dwarf. Yet, the introduced features from unique models at each  $\theta$  are much smaller than the angular resolution of HAWC. It is not expected for these effects to impact the limits and TS greatly as a result.

Median  $J$ -factor model profiles were provided by the authors. New maps were generated and analyzed for Segue1 and Coma Berenices. Figure 5.14 shows the differential between maps generated with the method from Section 5.8.1 and from the authors of [45]. These maps were reanalyzed for all SM DM annihilation channels. Upper limits for these channels are shown in Figure 5.15

From Figure 5.15, we can see that the impact of these model difference was no substantial. The observed impact was a fractional effect which is much smaller than the impact from selecting another DM spatial distribution model as was shown in Figure 5.10.

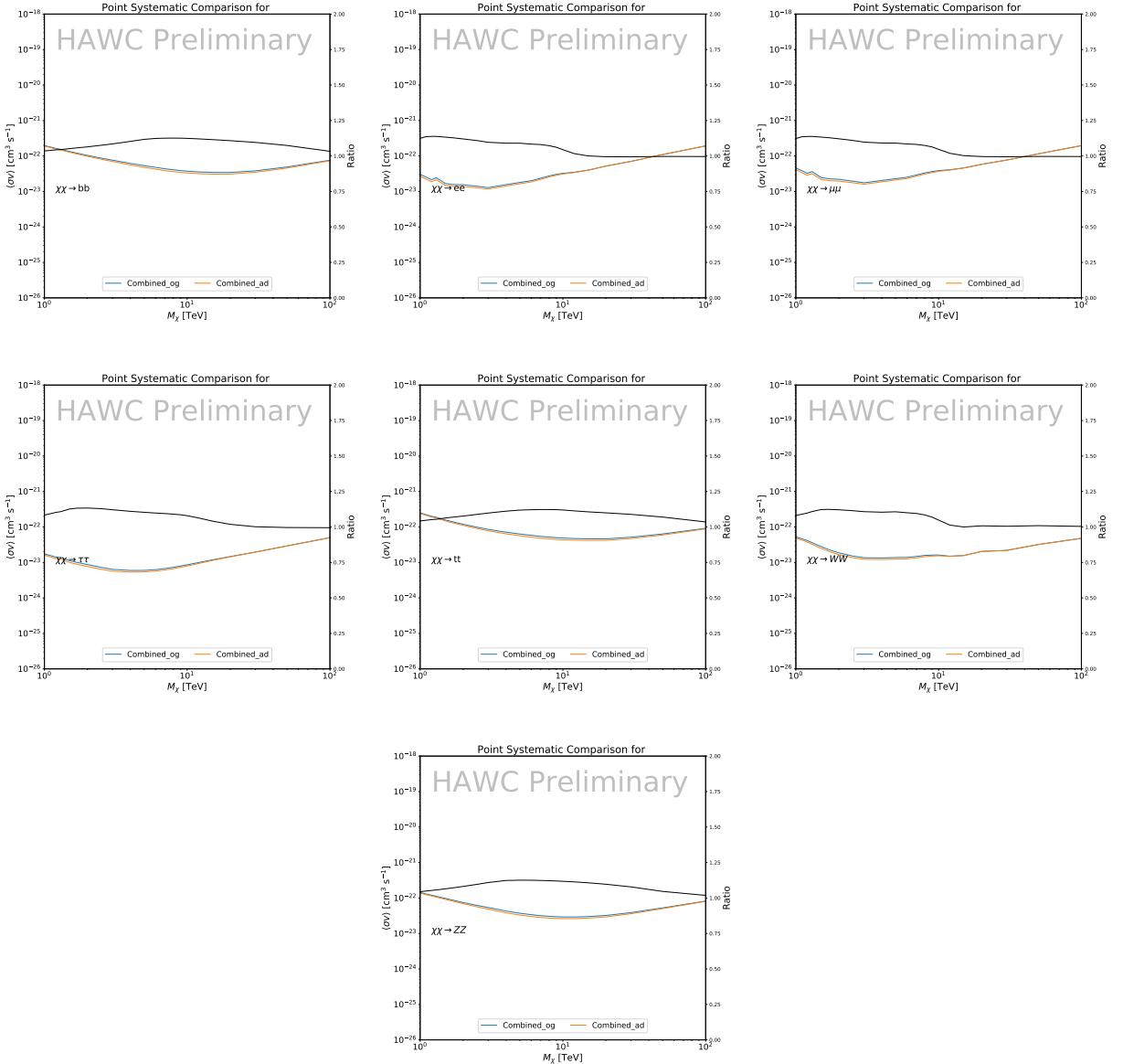


Figure 5.13 Comparison of combined limits when correcting for HAWC's pointing systematic. All DM annihilation channels are shown. The solid black line is the ratio between published limit to the declination corrected limit. The blue solid line or "Combined\_og" represented the limits computed for Glory Duck. The solid orange line or "Combined\_ad" represented the limits computed after correcting for the pointing systematic.

## 1019 5.8.2 $\mathcal{G}\mathcal{S}$ Versus $\mathcal{B}$ spatial models

1020 We show in this appendix a comparison between the  $J$ -factors computed by Geringer-Sameth  
 1021 *et al.* [53] (the  $\mathcal{G}\mathcal{S}$  set) and the ones computed by Bonnivard *et al.* [47, 55] (the  $\mathcal{B}$  set). The  
 1022  $\mathcal{G}\mathcal{S}$   $J$ -factors are computed through a Jeans analysis of the kinematic stellar data of the selected

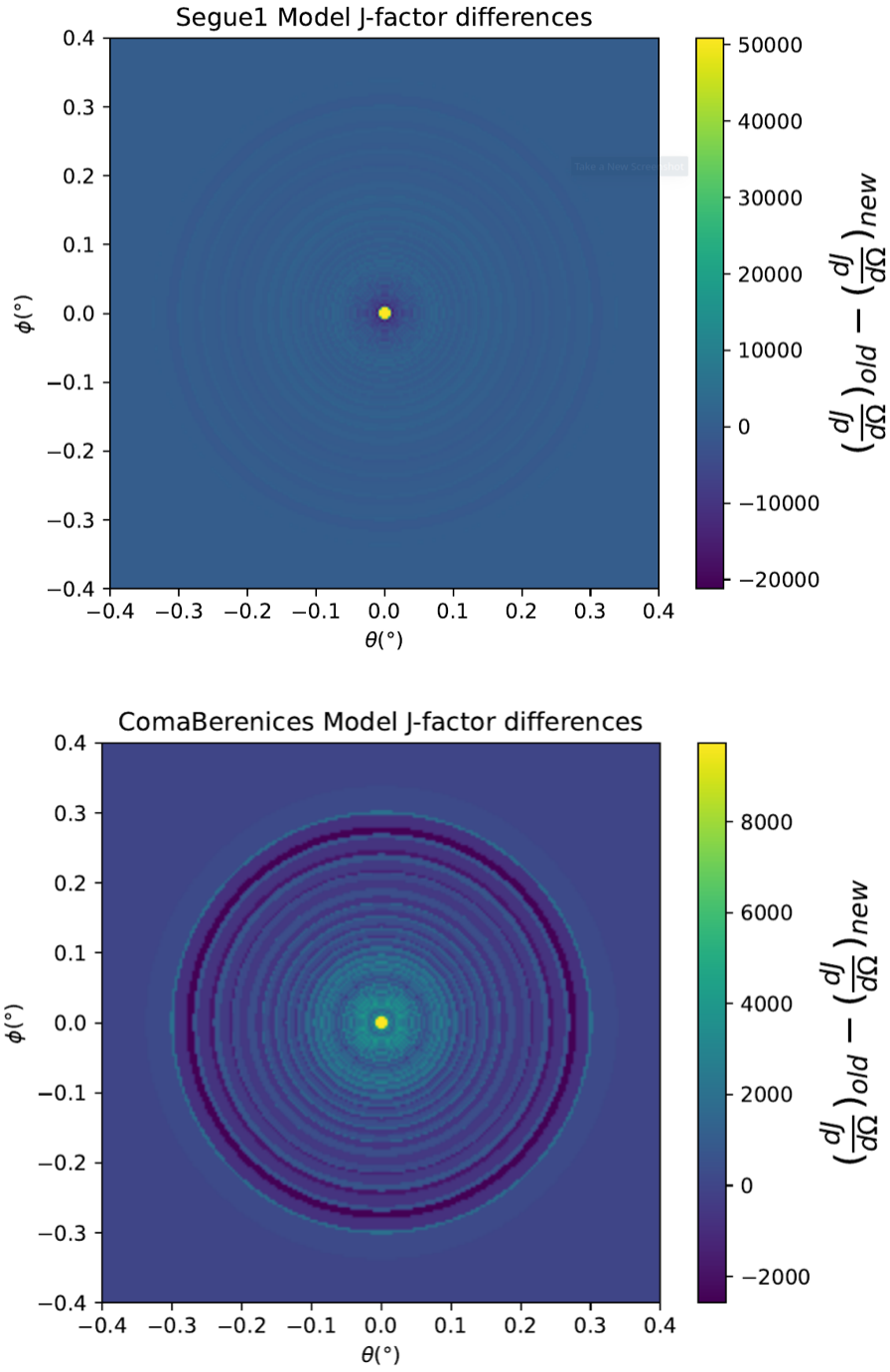


Figure 5.14 Differential map of  $dJ/\Omega$  from model built in Section 5.8.1 and profiles provided directly from authors. (Top) Differential from Segue1. (bottom) Differential from Coma Berenices. Note that their scales are not the same. Segue1 shows the deepest discrepancies which is congruent with its large uncertainties. Both models show anuli where unique models become apparent.

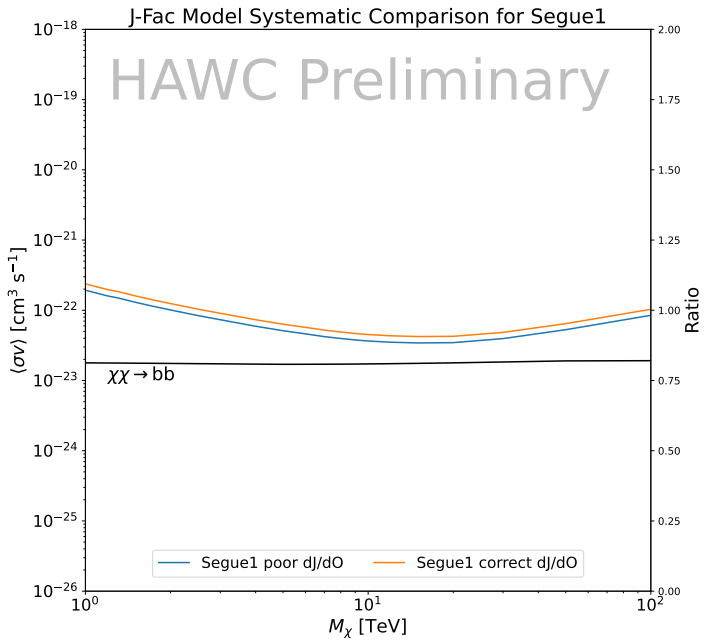
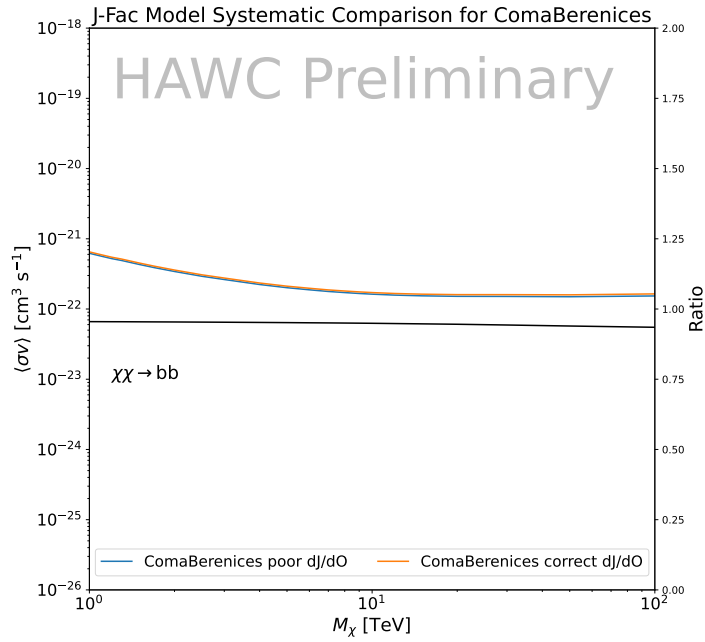


Figure 5.15 HAWC limits for Coma Berenices (top) and Segue1 (bottom) for two different map sets. Blue lines are limits calculated on maps with poor model representation. Orange lines are limits calculated on spatial profiles provided by the authors of [45]. Black line is the ratio of the poor spatial model limits to the corrected spatial models. The left y-axis measures  $\langle \sigma v \rangle$  for the blue and orange lines. The right y-axis measures the ratio and is unitless.

1023 dSphs, assuming a dynamic equilibrium and a spherical symmetry for the dSphs. They adopted  
1024 the generalized DM density distribution, known as Zhao-Hernquist, introduced by [58], carrying  
1025 three additional index parameters to describe the inner and outer slopes, and the break of the  
1026 density profile. Such a profile parametrization allows the reduction of the theoretical bias from  
1027 the choice of a specific radial dependency on the kinematic data. In other words, the increase of  
1028 free parameters with the use of the Zhao-Hernquist profile allows a better description of the mass  
1029 density distribution of dark matter.

1030 In addition, a constant velocity anisotropy profile and a Plummer light profile [59] for the stellar  
1031 distribution were assumed. The velocity anisotropy profile depends on the radial and tangential  
1032 velocity dispersion. However, its determination remains challenging since only the line-of-sight  
1033 velocity dispersion can be derived from velocity measurements. Therefore, the parametrization of  
1034 the anisotropy profile is obtained from simulated halos (see [60] for more details). They provide the  
1035 values of the  $J$ -factors of regions extending to various angular radius up to the outermost member  
1036 star.

1037 The  $\mathcal{B}$   $J$ -factors were computed through a Jeans analysis taking into account the systematic  
1038 uncertainties induced by the DM profile parametrization, the radial velocity anisotropy profile, and  
1039 the triaxiality of the halo of the dwarf galaxies. They performed a more complete study of the dSph  
1040 kinematics and dynamics than  $\mathcal{GS}$  for the determination of the  $J$ -factor. Conservative values of the  
1041  $J$ -factors where obtained using an Einasto DM density profile [61], a realistic anisotropy profile  
1042 known as the Baes & Van Hese profile [62] which takes into account that the inner regions can be  
1043 significantly non-isotropic, and a Zhao-Hernquist light profile [58].

1044 For both sets,  $J$ -factor values are provided for all dSphs as a function of the radius of the  
1045 integration region [53, 47, 55]. Table 5.1 shows the heliocentric distance and Galactic coordinates  
1046 of the twenty dSphs, together with the two sets of  $J$ -factor values integrated up to the outermost  
1047 observed star for  $\mathcal{GS}$  and the tidal radius for  $\mathcal{B}$ . Both  $J$ -factor sets were derived through a Jeans  
1048 analysis based on the same kinematic data, except for Draco where the measurements of [63] have  
1049 been adopted in the computation of the  $\mathcal{B}$  value. The computations for producing the  $\mathcal{GS}$  and  $\mathcal{B}$

1050 samples differ in the choice of the DM density, velocity anisotropy, and light profiles, for which the  
1051 set  $\mathcal{B}$  takes into account some sources of systematic uncertainties.

1052 Figure 5.16 and Figure 5.17 show the comparisons for the  $J$ -factor versus the angular radius  
1053 for each of the 20 dSphs used in this study. The uncertainties provided by the authors are also  
1054 indicated in the figures. For the  $\mathcal{GS}$  set, the computation stops at the angular radius corresponding  
1055 to the outermost observed star, while for the  $\mathcal{B}$  set, the computation stops at the angular radius  
1056 corresponding to the tidal radius.

## 1057 5.9 Discussion and Conclusions

1058 In this multi-instrument analysis, we have used observations of 20 dSphs from the gamma-ray  
1059 telescopes Fermi-LAT, H.E.S.S., MAGIC, VERITAS, and HAWC to perform a collective DM  
1060 search annihilation signals. The data were combined across sources and detectors to significantly  
1061 increase the sensitivity of the search. We have observed no significant deviation from the null, no  
1062 DM, hypothesis, and so present our results in terms of upper limits on the annihilation cross-section  
1063 for seven potential DM annihilation channels.

1064 Fermi-LAT brings the most stringent constraints for continuum channels below approximately  
1065 1 TeV. The remaining detectors dominate at higher energies. Overall, for multi-TeV DM mass,  
1066 the combined DM constraints from all five telescopes are 2-3 times stronger than any individual  
1067 telescope for multi-TeV DM.

1068 Derived from observations of many dSphs, our results produce robust limits given the DM  
1069 content of the dSphs is relatively well constrained. The obtained limits span the largest mass  
1070 range of any WIMP DM search. Our combined analysis improves the sensitivity over previously  
1071 published results from each detector which produces the most stringent limits on DM annihilation  
1072 from dSphs. These results are based on deep exposures of the most promising known dSphs with  
1073 the currently most sensitive gamma-ray instruments. Therefore, our results constitute a legacy of  
1074 a generation of gamma-ray instruments on WIMP DM searches towards dSphs. Our results will  
1075 remain the reference in the field until a new generation of more sensitive gamma-ray instruments  
1076 begin operations, or until new dSphs with higher  $J$ -factors are discovered.

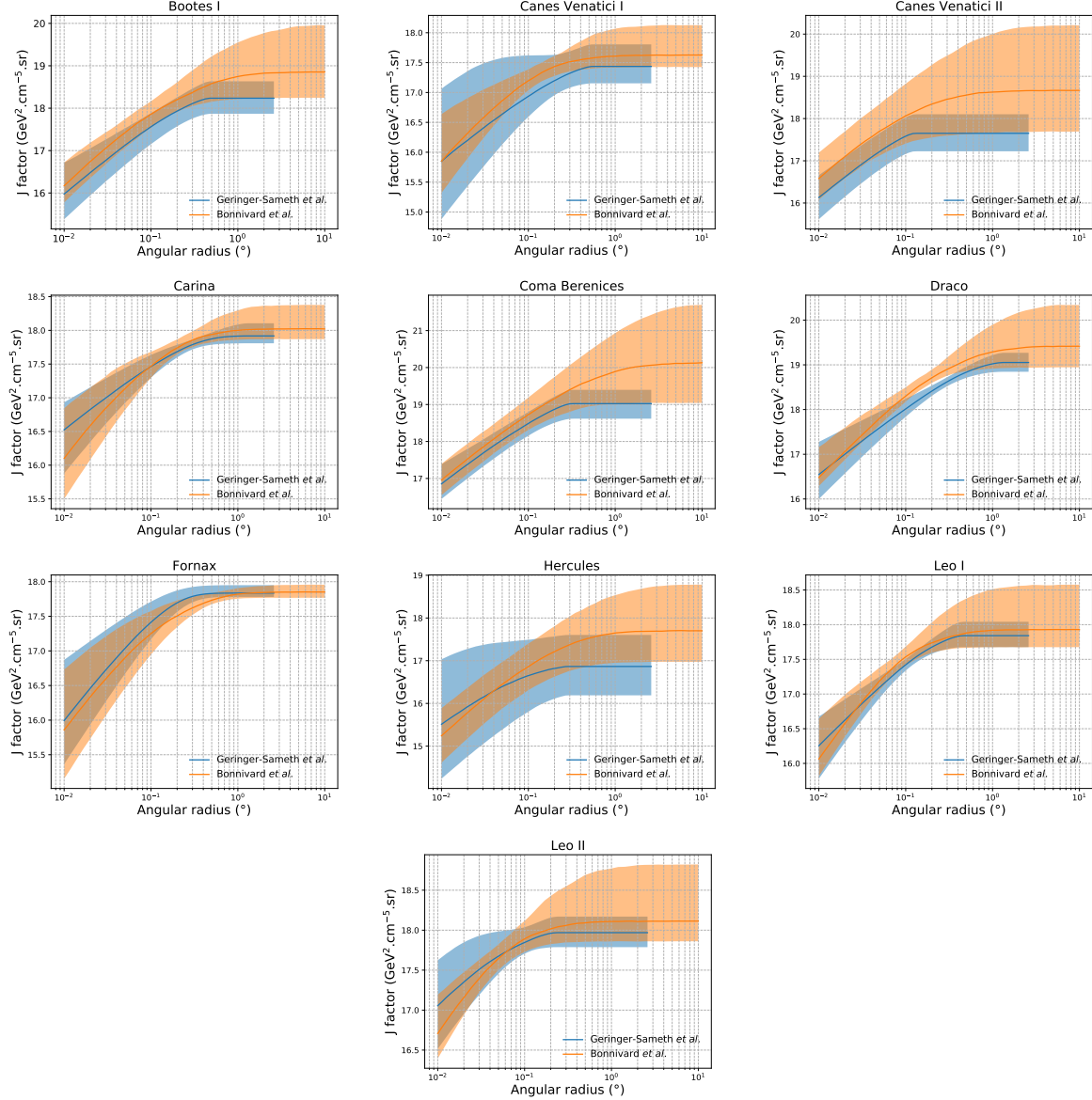


Figure 5.16 Comparisons between the  $J$ -factors versus the angular radius for the computation of  $J$  factors from Ref. [53] ( $\mathcal{GS}$  set in Table 5.1) in blue and for the computation from Ref. [47, 55] ( $\mathcal{B}$  set in Tab. 5.1) in orange. The solid lines represent the central value of the  $J$ -factors while the shaded regions correspond to the  $1\sigma$  standard deviation.

This analysis serves as a proof of concept for future multi-instrument and multi-messenger combination analyses. With this collaborative effort, we have managed to sample over four orders in magnitude in gamma-ray energies with distinct observational techniques. Determining the nature of DM continues to be an elusive and difficult problem. Larger datasets with diverse measurement techniques could be essential to tackling the DM problem. A future collaboration using similar

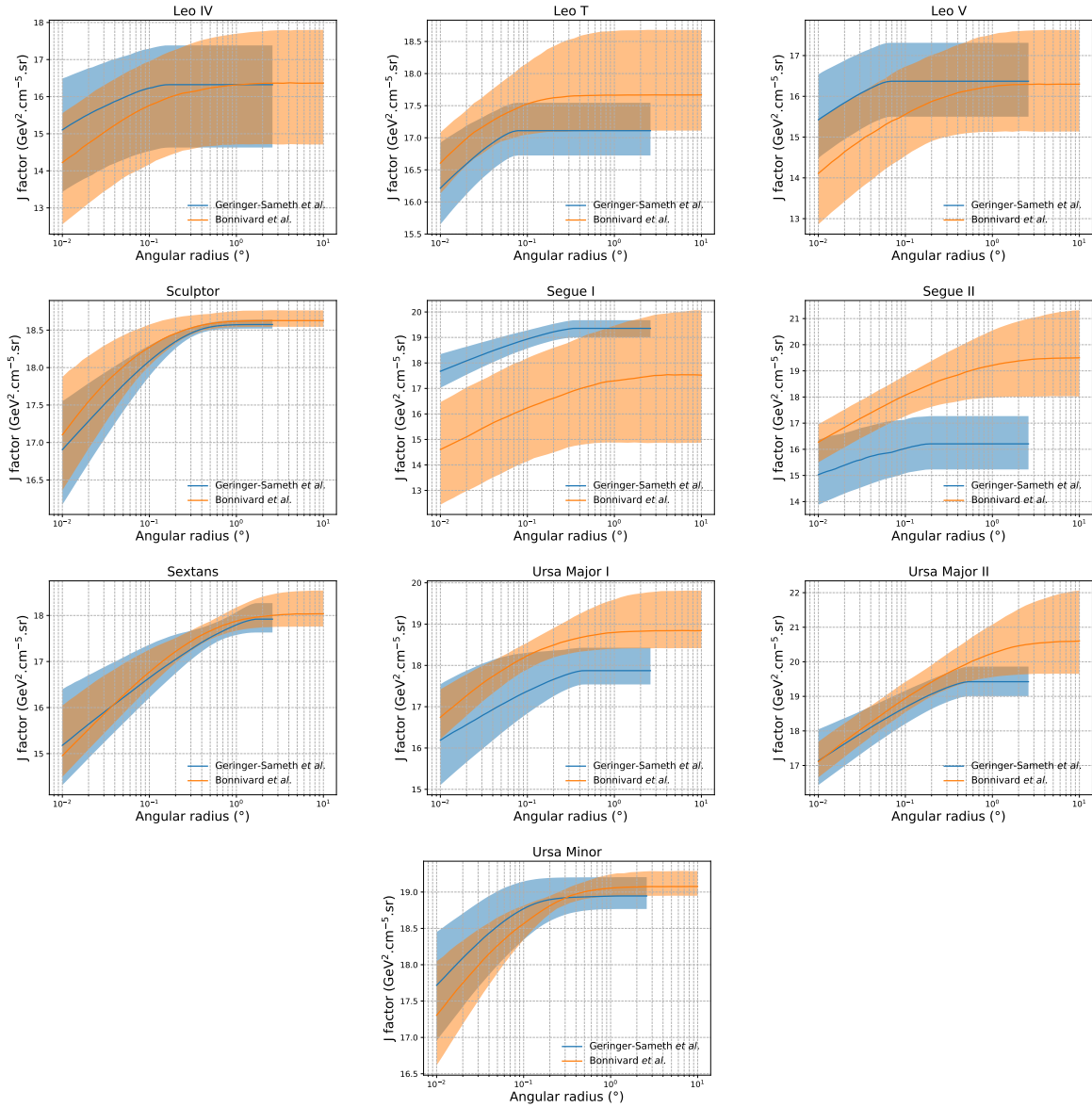


Figure 5.17 Comparisons between the  $J$ -factors versus the angular radius for the computation of  $J$  factors from Ref. [53] ( $\mathcal{GS}$  set in Tab. 5.1) in blue and for the computation from Ref. [47, 55] ( $\mathcal{B}$  set in Tab. 5.1) in orange. The solid lines represent the central value of the  $J$ -factors while the shaded regions correspond to the  $1\sigma$  standard deviation.

1082 techniques as the ones described in this paper could grow even beyond gamma rays. The models we  
 1083 used for this study include annihilation channels with neutrinos in the final state. Advanced studies  
 1084 could aim to merge our results with those from neutrino observatories with large data sets. Efforts  
 1085 are already underway to add data from the IceCube, ANTARES, and KM3NeT observatories to  
 1086 these gamma-ray results.

1087 From this work, a selection of the best candidates for observations, according to the latest  
1088 knowledge on stellar dynamics and modelling techniques for the derivation of the  $J$ -factors on  
1089 the potential dSphs targets, is highly desirable at the time that new experiments are starting their  
1090 dark matter programs using dSphs. Given the systematic uncertainty inherent to the derivation of  
1091 the  $J$ -factors, an informed observational strategy would be to select both objects with the highest  
1092  $J$ -factors that could lead to DM signal detection, and objects with robust  $J$ -factor predictions, i.e.  
1093 with kinematic measurements on many bright stars, which would strengthen the DM interpretation  
1094 reliability of the observation outcome.

1095 This analysis combines data from multiple telescopes to produce strong constraints on astro-  
1096 physical objects. From this perspective, these methods can be applied beyond just DM searches.  
1097 Almost every astrophysical study can benefit from multi-telescope, multi-wavelength gamma-ray  
1098 studies. We have enabled these telescopes to study the cosmos with greater precision and detail.  
1099 Many astrophysical searches can benefit from multi-instrument gamma-ray studies, for which our  
1100 analysis lays the foundation.

## CHAPTER 6

### MULTITHREADING HAWC ANALYSES FOR DARK MATTER SEARCHES

#### 6.1 Introduction

HAWC's current software suite, plugins to 3ML, does not fully utilize computational advancements of recent decades. Said advancements include the proliferation of Graphical Processing Units (GPUs), and multithreading on multicore processors. The analysis described in chapter 5 took up to 3 months of human time waiting for the full gambit of data analysis and simulation of background to run. Additionally, with the addition of a 2D binning scheme,  $f_{\text{hit}}$  and NN, the time needed to compute expected to grow. Although excessive computing time was, in part, from an intense use of a shared computing cluster, it was evident that there was room for improvement.

In HAWC's next generation dSph DM search, I decided to develop codes that would utilize the multicore processors on modern high performance computing clusters. The results of this work are featured in this chapter and brought a human timing improvement to computation that scales as  $1/N$  where  $N$  is the number of threads.

#### 6.2 Dataset and Background

This section enumerates the data and background methods used for HAWC's multithreaded study of dSphs. Section 6.2.1 and Section 6.2.2 are most useful for fellow HAWC collaborators looking to replicate a multithreaded dSph DM search.

##### 6.2.1 Itemized HAWC files

- Detector Resolution: `refit-Pass5-Final-NN-detRes-zenith-dependent.root`
- Data Map: `Pass5-Final-NN-maptree-ch103-ch1349-zenith-dependent.root`
- Spectral Dictionary: `HDMspectra_dict_gamma.npy`

##### 6.2.2 Software Tools and Development

This analysis was performed using HAL and 3ML [42, 43] in Python version 3. I built software in collaboration with Michael Martin and Letrell Harris to implement the *Dark Matter Spectra from*

1125 *the Electroweak to the Planck Scale* (HDM) [64] and dSphs spatial model from [65] for HAWC  
1126 analysis. A NumPy dictionary of HDM was made for Py3. The corresponding Python3 file is  
1127 `HDMspectra_dict_gamma.npy`. These files can also be used for decay channels and tools are  
1128 provided in HDM’s [git repository](#) [64]. The analysis was performed using the Neural Network  
1129 energy estimator for Pass 5.F. A description of this estimator was provided in chapter 3. **TODO:**  
1130 **Define a subsection when it’s written**, and its key improvements are an improved energy estimation  
1131 and improved sensitivities at higher zenith angles. All other software used for data analysis, DM  
1132 profile generation, and job submission to SLURM are also kept in my sandbox in the [Dark Matter](#)  
1133 [HAWC](#) project. The above repository also incorporates the model inputs used previously in Glory  
1134 Duck, described in chapter 5

1135 **6.2.3 Data Set and Background Description**

1136 The HAWC data maps used for this analysis contain 2565 days of data between runs 2104 (   
1137 **TODO: Day start**) and 7476 ( **TODO: Day end**). They were generated from pass 5.f reconstruction.  
1138 The analysis is performed using the NN energy estimator with bin list:

1139     B1C0Ea, B1C0Eb, B1C0Ec, B1C0Ed, B1C0Ee, B2C0Ea, B2C0Eb, B2C0Ec, B2C0Ed, B2C0Ee,  
1140     B3C0Ea, B3C0Eb, B3C0Ec, B3C0Ed, B3C0Ee, B3C0Ef, B4C0Eb, B4C0Ec, B4C0Ed, B4C0Ee,  
1141     B4C0Ef, B5C0Ec, B5C0Ed, B5C0Ee, B5C0Ef, B5C0Eg, B6C0Ed, B6C0Ee, B6C0Ef, B6C0Eg,  
1142     B6C0Eh, B7C0Ee, B7C0Ef, B7C0Eg, B7C0Eh, B7C0Ei, B8C0Ee, B8C0Ef, B8C0Eg, B8C0Eh,  
1143     B8C0Ei, B8C0Ej, B9C0Ef, B9C0Eg, B9C0Eh, B9C0Ei, B9C0Ej, B10C0Eg, B10C0Eh,  
1144     B10C0Ei, B10C0Ej, B10C0Ek, B10C0El

1145 Bin 0 was excluded as it has substantial hadronic contamination and poor angular resolution.

1146 Background considerations and source selection was identical to Section 5.2, and no additional  
1147 arguments are provided here. Many of the HAWC systematics explored in Section 5.7 also apply  
1148 for this DM search and are not added upon here.

1149 **6.3 Analysis**

1150 The analysis and its systematics are almost identical to Section 5.3. Importantly, we use the  
1151 same Equation (7.1) and Equation (5.2) for estimating the gamma-ray flux at HAWC from our  
1152 sources. We add on to the previous study with a search for DM decay. The flux equations for DM  
1153 decay are

$$\frac{d\Phi_\gamma}{dE_\gamma} = \frac{1}{4\pi\tau m_\chi} \frac{dN_\gamma}{dE_\gamma} \times \int_{\text{source}} d\Omega \int_{l.o.s} \rho_\chi dl(r, \theta') \quad (6.1)$$

1154 with a new quantity, the  $D$  factor, defined as

$$D = \int d\Omega \int_{l.o.s} dl \rho_\chi(r, \theta') \quad (6.2)$$

1155 Software was written to accommodate DM decay from dSphs, however decay profiles were not  
1156 received from  $\mathcal{L}\mathcal{S}$  by the time of writing this thesis.

1157 **6.3.1  $\frac{dN_\gamma}{dE_\gamma}$  - Particle Physics Component**

1158 For these spectra, we import HDM with Electroweak (EW) corrections and additional correc-  
1159 tions for neutrinos above the EW scale [64]. The spectrum is implemented as a model script in  
1160 astromodels for 3ML. A comprehensive description of EW corrections and neutrino considerations  
1161 are provided later in [TODO: refeance MM nu duck](#).

1162 Figure 6.1 demonstrates the impact of changes from HDM on DM annihilation to W bosons.  
1163 A class in astromodels was developed to include HDM and is aptly named `HDMspectra` within  
1164 `DM_models.py`. The SM DM annihilation channels studied here are  $\chi\chi \rightarrow$ :

1165  $e^+e^-$ ,  $\mu^+\mu^-$ ,  $\tau^+\tau^-$ ,  $b\bar{b}$ ,  $t\bar{t}$ ,  $gg$ ,  $W^+W^-$ ,  $ZZ$ ,  $c\bar{c}$ ,  $u\bar{u}$ ,  $d\bar{d}$ ,  $s\bar{s}$ ,  $\nu_e\bar{\nu}_e$ ,  $\nu_\mu\bar{\nu}_\mu$ ,  $\nu_\tau\bar{\nu}_\tau$ ,  $\gamma\gamma$ ,  $hh$ .

1166 For  $\gamma\gamma$  and  $ZZ$ , a substantial fraction of the signal photons are expected to have total energy equal  
1167 to  $m_\chi$  [64]. This introduces a  $\delta$ -function that is much narrower than the energy resolution of the  
1168 HAWC detector. To ensure that this feature is not lost in the likelihood fits, the 'line' feature is  
1169 convolved with a Gaussian kernel with a  $1\sigma$  width of  $0.05 \cdot m_\chi$  and total kernel window of  $\pm 4\sigma$ .  
1170 This differs from HAWC's previous line study where 30% of HAWC's energy resolution was used  
1171 for the kernel [66]. The NN energy estimator's strength compared to  $f_{\text{hit}}$  at low gamma-ray energy

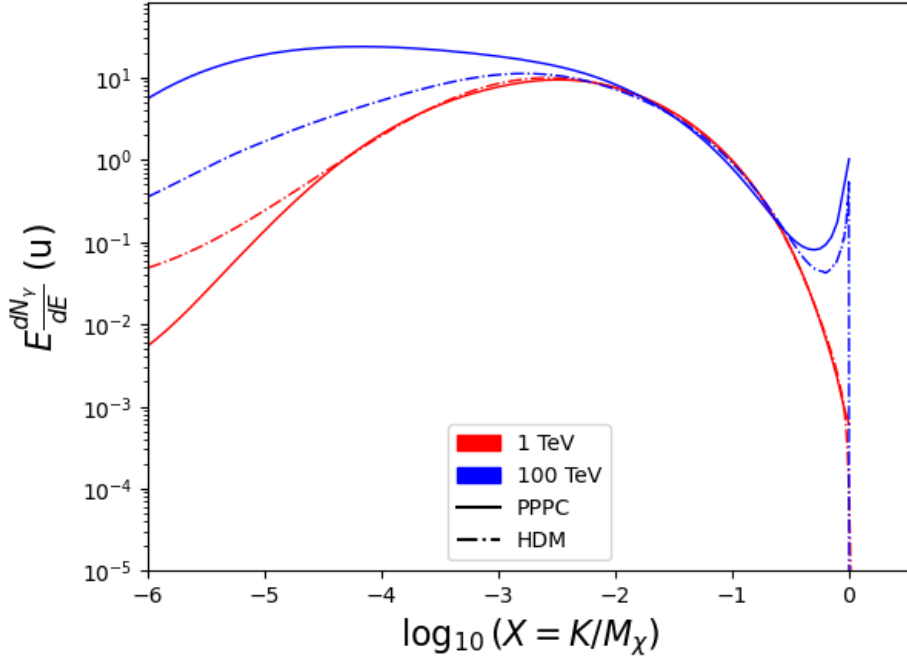


Figure 6.1 Difference between spectral hypotheses from PPPC [44] and HDM [64]. Shown is the expected DM annihilation spectrum for  $\chi\chi \rightarrow W^-W^+$ . Solid lines are spectral models with EW corrections from the PPPC. Dash-dot lines are spectral models from HDM. Red lines are models for  $M_\chi = 1$  TeV. Blue lines represent models for  $M_\chi = 100$  TeV.

enables smaller resolutions in addition to low energy tails in the spectral models [64].  $\chi\chi \rightarrow \gamma\gamma$  and ZZ spectral hypotheses are shown in Figure 6.2. Spectral models for the remaining annihilation channels are plotted for each  $m_\chi$  in Figure B.1.

### 6.3.2 J and D- Astrophysical Components

The J-factor profiles for each source are imported from Louis Strigari et al. (referred to with  $\mathcal{LS}$ ) [65]. Profiles in  $\frac{dJ}{d\Omega}(\theta)$  up to  $\theta = 0.5^\circ$  were provided directly from the authors. Map generation from these profiles were almost identical to Section 5.3.2 except that a higher order trapezoidal integral was used for the normalization of the square, uniformly-spaced map:

$$p^2 \cdot \sum_{i=0}^N \sum_{j=0}^M w_{i,j} \frac{d\mathcal{K}}{d\Omega}(\theta_{i,j}, \phi_{i,j}) \quad (6.3)$$

$\mathcal{K}$  is either  $J$  or  $D$  for the spatial distributions of annihilation or decay respectively.  $p$  is the angular side of one pixel in the map.  $w_{i,j}$  is a weight assigned the following ways:

$w_{i,j} = 1$  if  $(\theta_{i,j}, \phi_{i,j})$  is fully within the region of integration

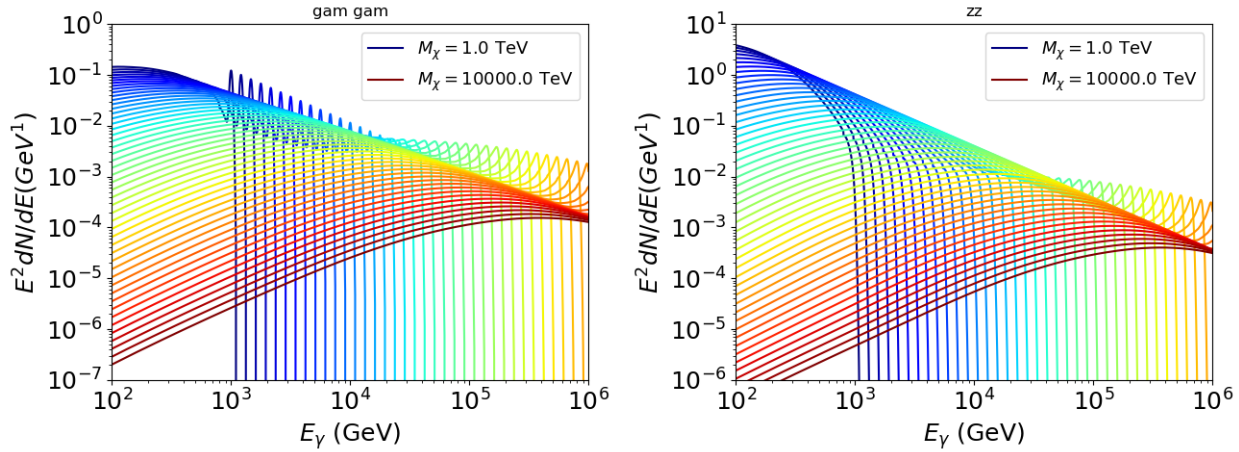


Figure 6.2 Photon spectra for  $\chi\chi \rightarrow \gamma\gamma$  (left) and  $\chi\chi \rightarrow ZZ$  (right) after Gaussian convolution of line features. Both spectra have  $\delta$ -features at photon energies equal to the DM mass. Bluer lines are annihilation spectra with lower DM mass. Redder lines are spectra from larger DM mass. All Spectral models are sourced from the Heavy Dark Matter models [64]. Axes are drawn roughly according to the energy sensitivity of HAWC.

1183        $w_{i,j} = 1/2$  if  $(\theta_{i,j}, \phi_{i,j})$  is on an edge of the region of integration

1184        $w_{i,j} = 1/4$  if  $(\theta_{i,j}, \phi_{i,j})$  is on a corner of the region of integration

1185   Figure 6.3 shows the median and  $\pm 1\sigma$  maps used as input for DM annihilation studied by  $\mathcal{LS}$ .

### 1186   **6.3.3 Source Selection and Annihilation Channels**

1187   HAWC's sources for this multithreaded analysis include Coma Berenices, Draco, Segue 1, and

1188   Sextans  $\mathcal{LS}$  observes up to 43 sources in its publication, however only 4 of the best fit profiles were  
 1189   provided at the time this thesis was written. A full description of each source used in this analysis  
 1190   is found in Table 6.1.

1191   This analysis improves on chapter 5 in the following ways. Previously, the particle physics

1192   model used for gamma-ray spectra from DM annihilation was from the PPPC [44] which missed  
 1193   important considerations relevant for the neutrino sector. HDM is used to account for this shortfall

1194   [64]. HDM also models DM to the Planck scale which permits HAWC to probe PeV scale DM.

1195   For this study, we sample DM masses: 1 TeV - 10 PeV with 6 mass bins per decade in DM mass.

1196   In the case of line spectra ( $\chi\chi \rightarrow \gamma\gamma$ , or  $ZZ$ ), we double the mass binning to 12 DM mass bins

1197   per decade in DM mass. A larger source catalog is used that uses a Navarro–Frenk–White (NFW)

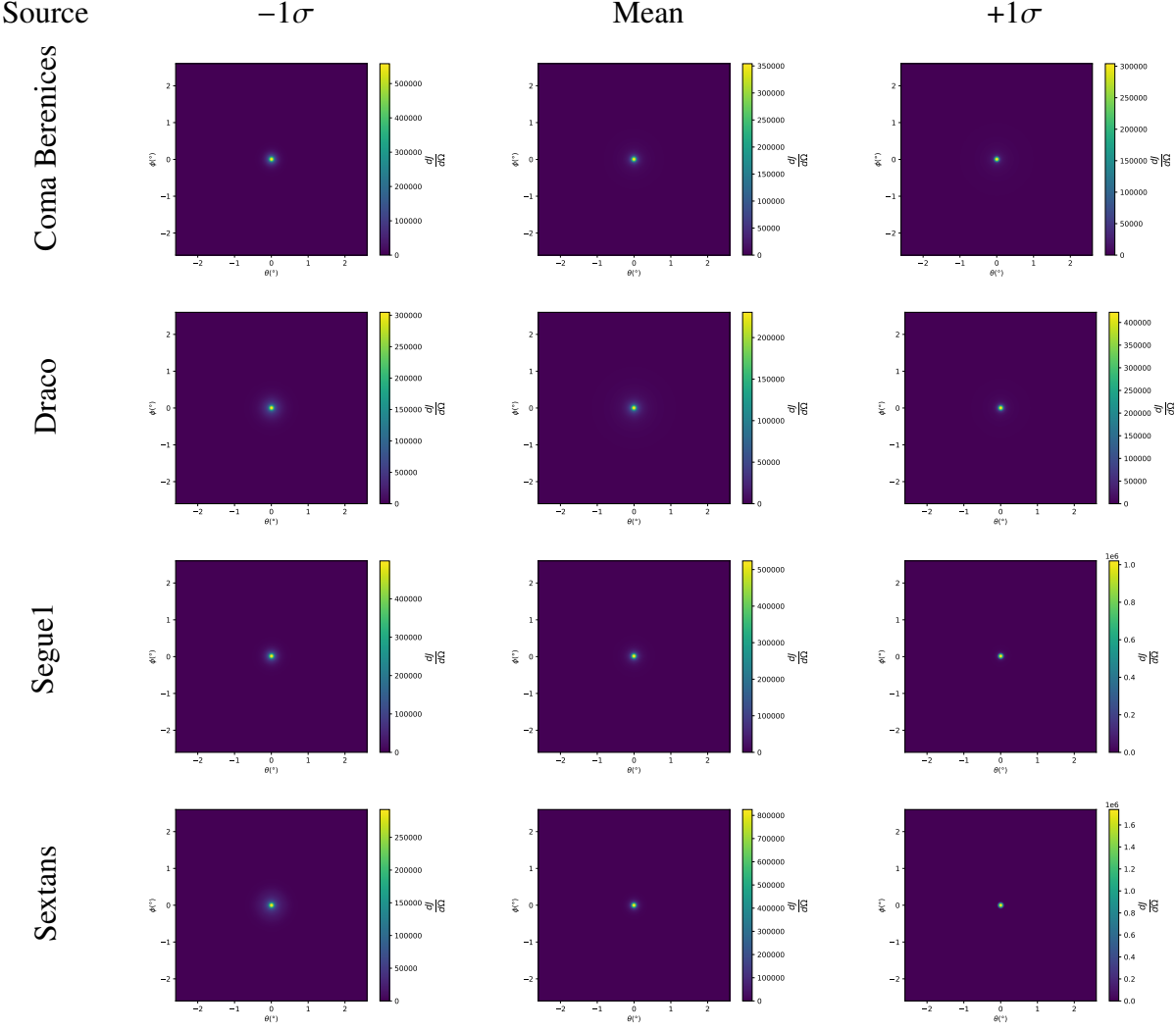


Figure 6.3  $\frac{dJ}{d\Omega}$  maps for Coma Berenices, Draco, Segue1, and Sextans. Columns are divided for the  $\pm 1\sigma$  uncertainties in  $dJ/d\Omega$  around the mean value from  $\mathcal{LS}$  [65]. Origin is centered on the specific dwarf spheroidal galaxies (dSph).  $\theta$  and  $\phi$  axes are the angular separation from the center of the dwarf

1198 spatial DM distribution from  $\mathcal{LS}$  [65]. Because NFW has fewer parameters than what is used  
 1199 for  $\mathcal{GS}$ ,  $\mathcal{LS}$  is able to fit ultra-faint dwarves, expanding the number of sources available for DM  
 1200 searches. Finally, the gamma-ray ray dataset is much larger. The study performed here analyzes  
 1201 2565 days of data compared to 1017 days analyzed in chapter 5.

## 1202 6.4 Likelihood Methods

1203 These are identical to Section 5.4.1 and no additional changes are made to the likelihood. Bins  
 1204 in this analysis are expanded to include HAWC’s NN energy estimator.

1205 **6.5 Computational Methods: Multithreading**

1206 Previously, as in Section 5.3, the likelihood was minimized for one model at a time. One  
 1207 model in this case representing a DM annihilation channel, DM mass, and dSph. In an effort  
 1208 to conserve human and CPU time, jobs submitted for high performance computing contained a  
 1209 list of DM masses to iterate over for likelihood fitting. Jobs were then trivially parallelized for  
 1210 each permutation of the two lists: CHANS (SM annihilation channel) and SOURCES (dSph spatial  
 1211 templates). The lists for CHANS and SOURCES are found in Section 6.3.1 and Table 6.1, respectively.  
 1212 Initially, 11 DM mass bins were serially sampled for one job defined by a [SM channel, dSph] set.  
 1213 Computing the likelihoods would take between 1.5 to 2 hrs, stochastically, for a job. We expect to  
 1214 compute likelihoods for data and 300 Poisson background trials. The estimated CPU time based on  
 1215 the above for all SM annihilation channels (17) and 25 sources (all  $\mathcal{LS}$  sources within HAWC's  
 1216 field of view) amounted to 127,925 jobs. In total, 1,407,175 likelihood fits and profiles would  
 1217 be computed for the 11 mass bins we wished to study. The estimated CPU time ranged between  
 1218 10k CPU days - 8k CPU days. Human time is more challenging to estimate as job allocation is  
 1219 stochastic and highly dependent on what other users are submitting, yet it is unlikely that all jobs  
 1220 would run simultaneously. Therefore, we can expect human time to be about as long as was seen  
 1221 in chapter 5 which was on the order of months to fully compute on a smaller analysis. A visual aid  
 1222 to describe how jobs were organized is provided in Figure 6.4.

Name	Distance (kpc)	$l, b$ ( $^{\circ}$ )	$\log_{10} J$ ( $\mathcal{LS}$ set) $\log_{10}(\text{GeV}^2 \text{cm}^{-5} \text{sr})$
Coma Berenices	44	241.89, 83.61	$19.00^{+0.36}_{-0.35}$
Draco	76	86.37, 34.72	$18.83^{+0.12}_{-0.12}$
Segue I	23	220.48, 50.43	$19.12^{+0.49}_{-0.58}$
Sextans	86	243.50, 42.27	$17.73^{+0.13}_{-0.12}$

Table 6.1 Summary of the relevant properties of the dSphs used in the present work. Column 1 lists the dSphs. Columns 2 and 3 present their heliocentric distance and galactic coordinates, respectively. Column 4 reports the  $J$ -factors of each source given from the  $\mathcal{LS}$  studies and estimated  $\pm 1\sigma$  uncertainties. The values  $\log_{10} J$  ( $\mathcal{LS}$  set) [65] correspond to the mean  $J$ -factor values for a source extension truncated at  $0.5^{\circ}$ .

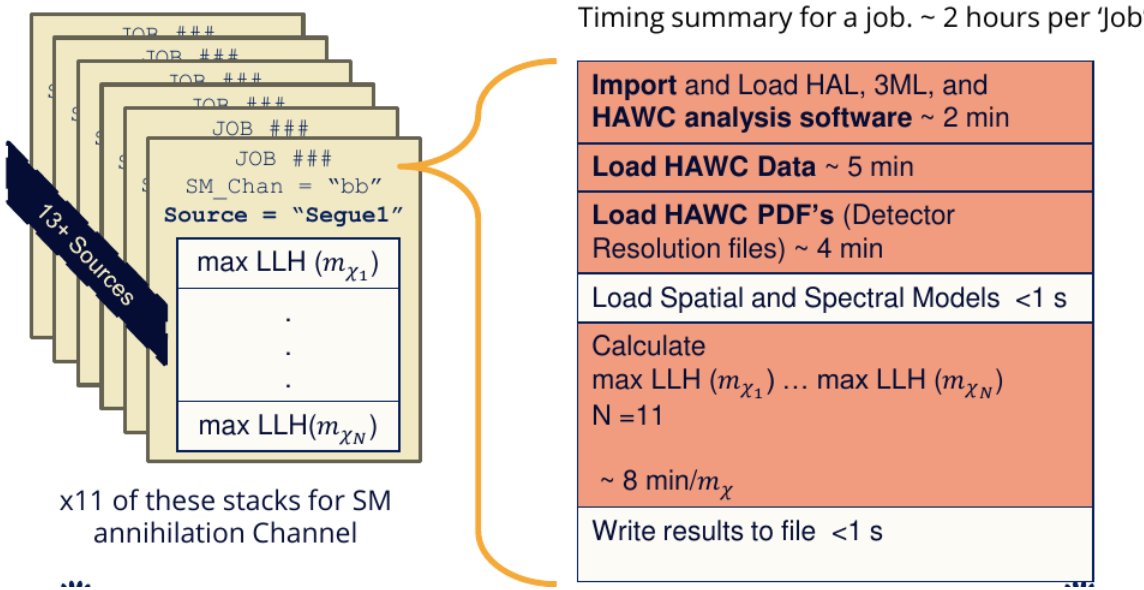


Figure 6.4 Infographic on how jobs and DM computation was organized in Section 5.3. Jobs were built for each permutation of CHANS and SOURCES shown by the left block in the figure. Each job, which took on the order 2 hrs to compute, had the following work flow: 1. Import HAWC analysis software, 2 min to run. 2. Load HAWC count maps, 5 min to run. 3. Load HAWC energy and spatial resolutions, 4 min. 5. Load DM spatial source templates and spectral models, less than 1 s. 6. Perform likelihood fit on data and model, about 8 min per DM mass. 7. Write results to file, less than 1s.

1223     The computational needs for this next generation DM analysis are extreme and is unlike other  
 1224     analyses performed on HAWC. It became clear that there was a lot to gain from optimizing how  
 1225     the likelihoods are computed. This section discusses how multi-threading was applied to solve and  
 1226     reduce HAWC's computing of likelihoods for large parameter spaces like in DM searches.

### 1227     6.5.1 Relevant Foundational Information

1228     The profiling of the likelihood for HAWC is done via gradient descent where the normalization  
 1229     of Equation (7.1) (linearly correlated with  $\langle \sigma v \rangle$ ) is rescaled in the descent. Additionally, we sample  
 1230     the likelihood space for a defined list of  $\langle \sigma v \rangle$ 's described in Section 5.4.2. The time to compute  
 1231     these values is not predictable or consistent because many variables can change across the full  
 1232     model-space. Comprehensively, these variables are:

- 1233       •  $m_{\chi}$  : DM rest mass
- 1234       • CHAN : DM SM annihilation channel.

1235 • SOURCE : dSph within HAWC's field of view. This involves a spatial template AND coordinate  
1236 in HAWC data.

1237 •  $\langle\sigma v\rangle$ : Effectively the flux normalization and free parameter in the likelihood fit.

1238 Therefore, we develop an asynchronous, functional-parallel coding pattern. Asynchronous mean-  
1239 ing that the instructions and computing within a function are independent and permitted to be out  
1240 of sync with sibling computations. Functional-parallel meaning that instructions are the subject of  
1241 parallelization rather than threading the likelihood computation. This is close to trivial parametriza-  
1242 tion seen in Figure 6.4 except that we seek to consolidate the loading stages (software, data, and  
1243 detector resolution loading). Reducing the total instances of loading stages and distributing access  
1244 to the reduced loads across multiple asynchronous threads is expected to reduce serial processing  
1245 time and the overhead implicit to each job in addition to saving human time.

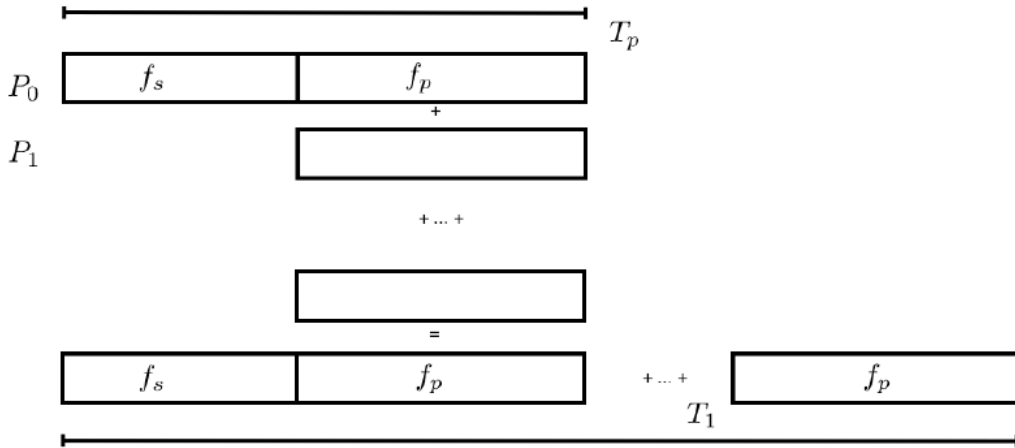


Figure 6.5 Graphic of Gustafson parallel coding pattern.  $f_s$  is the fraction of a program, in time, spent on serial computation.  $f_p$  is the fraction of computing time that is parallelizable.  $T_p$  is the total time for a parallel program to run.  $T_1$  is the total time for a parallel program to run if only 1 processor is allocated.  $P_N$  is the  $N$ -th processor where it's row is the computation the processor performs. The Gustafson pattern is most similar to what is implemented for this analysis. Figure is pulled from [67].

1246 We need a way to measure and compare the expected speedup and efficiency gain for this  
1247 asynchronous coding pattern. I pull inspiration for timing measurement from [67] and use *Amdahl's  
1248 law with hybrid programming*. Hybrid programming meaning that the computation is a mix of

1249 distributed and shared memory programming. If we assume the code is fully parallelizable over  $p$   
1250 processors and  $c$  threads, the ideal speedup is simply  $pc$  and ideal run-time is  $T_1/(pc)$ .  $T_1$  is the  
1251 total time for a parallel program to run if only 1 processor is allocated. However, the coding pattern  
1252 contains some amount of unavoidable serial computation, as shown in Figure 6.5. In our case, the  
1253 run time is estimated to be

$$T_{p,c} = \frac{T_1}{pc} (1 + F_s(c - 1)). \quad (6.4)$$

1254  $F_s$  is the fraction of CPU time dedicated to serial computation. The expected speedup is

$$S_{p,c} \equiv \frac{T_1}{T_{p,c}} = \frac{pc}{1 + F_s(c - 1)}. \quad (6.5)$$

1255 From Equation (6.5), we can see that the speed-up scales with  $p/F_s$ . We are free to minimize  
1256  $F_s$  asymptotically by enlarging the total models that are submitted to the thread pool, thereby  
1257 shrinking the CPU fraction dedicated to serial operation. We are also free to define exactly how  
1258 many threads and processors we utilize, yet eventually hit a hard cap at the hardware available on  
1259 our computing cluster. HAWC uses Intel Xeon processors with 48 cores and 96 threads. This  
1260 means when N-threads ( $c$ ) are defined,  $N \bmod 2$  cores ( $p$ ) are needed. We see that a successful  
1261 code scales well as the expected speedup is inversely correlated with  $F_s$ . As the total number of  
1262 models sampled grows, the speedup will also.

### 1263 6.5.2 Implementation

1264 The multithreaded code was written in Python3 and is documented in the `dark_matter_hawc`  
1265 [repository](#) within the script named `mpu_analysis.py`. A version of the script as of April 25  
1266 **TODO: make sure to update on this date** is also provided in Section B.2 It has many dependencies  
1267 including the HAWC analysis software. Figure 6.6 displays the workflow of a job with 3 threads.  
1268 Within a job, SOURCE is kept fixed . CHAN(S) remains 17 elements long. More  $m_\chi$  are sampled  
1269 from 11 bins up to 49 (for  $\gamma\gamma$  and ZZ) and 25 (for remaining CHANS) which amounts to 12 or 6  
1270 mass bins per decade. The DM mass,  $m_\chi$ , and SM annihilation channels, CHANS, are permuted into  
1271 a 473 element list which is split evenly across N threads where N ranges between 5 - 16. Within a  
1272 thread, for each  $m_\chi$ -CHAN tuple, 1001  $\langle\sigma v\rangle$  values are sampled in the likelihood, and the value of

Timing summary for a multi-threaded job.

Import and Load HAL, 3ML, and <b>HAWC analysis software</b> ~ 2 min		
Load HAWC Data ~ 5 min		
Load HAWC PDF's (Detector Resolution files) ~ 4 min		
Load Spatial Model < 1s		
Load Spectra Models <1 s	Load Spectra Models <1 s	Load Spectra Models <1 s
Calculate max LLH (Chan_0, $m_{\chi_1}$ ) ... max LLH (Chan_?, $m_{\chi_N}$ ) N = TOTAL/N_THREADS  ~ 8 min/Spec_model	Calculate max LLH (Chan_?, $m_{\chi_1}$ ) ... max LLH (Chan_?, $m_{\chi_N}$ ) N = TOTAL/N_THREADS  ~ 8 min/Spec_model	Calculate max LLH (Chan_?, $m_{\chi_1}$ ) ... max LLH (Chan_?, $m_{\chi_N}$ ) N = TOTAL/N_THREADS  ~ 8 min/Spec_model
Write results to file <1 s	Write results to file <1 s	Write results to file <1 s
Join Threads and terminate < 1s		

Figure 6.6 Task chart for one multithreaded job developed for this project. Green blocks indicate a shared resource across the threads AND computation performed serially. Red blocks indicate functional parallel processing within each thread. 3 threads are represented here, yet many more can be employed during the full analysis. Jobs are defined by the SOURCE as these require unique maps to be loaded into the likelihood estimator. The  $m_{\chi}$ , CHAN, and  $\langle \sigma v \rangle$  variables are entered into the thread pool and allocated as evenly as possible across the threads.

1273  $\langle \sigma v \rangle$  that maximizes the likelihood is found. Although rare, fits that failed are handled on a case  
 1274 by case basis.

### 1275 6.5.3 Performance

M Tasks	$T_{p,c}$ (hr:min:s)			
	$T_{1,1}$	$T_{1,2}$	$T_{1,8}$	$T_{1,16}$
50	1:40:37.5	0:52:43.7	0:19:13.8	0:13:44.0
74	2:22:30.0	1:15:00.6	0:25:21.3	0:15:49.8
100	(3:07:51.9)	1:40:10.5	0:30:44.4	0:20:01.4
200	(6:02:20.6)	-	1:00:32.0	0:30:35.0
473	(13:58:40.3)	-	<b>TODO: run this</b>	1:07:53.2

Table 6.2 Timing summaries for analyses for serial and multithreaded processes. M tasks is the number of functional-parallel tasks ran for the computation.  $T_{p,c}$  is a single run time in hours:minutes:seconds for runs utilizing  $p$  nodes and  $c$  threads. Runs are run interactively on the same computer to maximize consistency. Empty entries are indicated with '-'. (·) entries are estimated entries extrapolated from data earlier in the column.

1276 We see a tremendous reduction to human time waiting for our dSph analyses to run. Table 6.2

1277 shows the timing summaries for analyses of different sizes and thread counts. Additionally, the  
 1278 efficiency gained when consolidating the serial loading of data is also apparent in our ability to  
 1279 study many more tasks in about the same amount of wall time as a smaller serial computation. Trials  
 1280 represented in the table were run on an AMD Opteron® processor 6344 with 48 cores, 2 threads  
 1281 per core; 2.6 GHz clock. This is not the same architecture used for analysis on the computing  
 1282 cluster however they are similar enough that results shown here are reasonably representative of  
 1283 computing on the HAWC computing cluster. I use the Tab. 6.2 for the inferences and conclusions  
 1284 in the following paragraphs.

1285 First, we want to find  $T_s$ , the time of serial computation. From Fig. 6.5, the timing for our  
 1286 coding pattern can be written as

$$T_s + Mt_p = T_{1,1}^M. \quad (6.6)$$

1287  $M$  is the number of functional-parallel tasks (represented as column 1 of Tab. 6.2), and  $t_p$  is the  
 1288 average time to complete a single parallel task.  $T_{1,1}^M$  is the total time for a parallel program to run if  
 1289 only 1 processor is allocated for  $M$  parallel task. With two runs of different  $M$  ( $M1$  and  $M2$ ), we  
 1290 can use a system of equations to derive

$$T_s = T_{1,1}^{M1} - M1 \left( \frac{T_{1,1}^{M1} - T_{1,1}^{M2}}{M1 - M2} \right). \quad (6.7)$$

1291 We also extract  $t_p$  using the same methods:

$$t_p = \frac{T_{1,1}^{M1} - T_{1,1}^{M2}}{M1 - M2}. \quad (6.8)$$

1292 From Tab. 6.2, we set  $M1 = 50$  and  $M2 = 74$  and take their corresponding  $T_{1,1}$  from the table to  
 1293 calculate  $T_s$  and  $t_p$ .

$$T_s = 803.1\text{s} \text{ and } t_p = 104.6\text{s} \quad (6.9)$$

1294 Now, we have specific estimation for the fraction of serial computing time,  $F_s$ :

$$F_s = \frac{803.1}{803.1 + 104.6 \cdot M}. \quad (6.10)$$

1295 The maximum  $M$  for this study is 473 which evaluates using Eq. (6.10):  $F_s = 0.016$  or 1.6% of  
 1296 computing time. Table 6.3 shows the resulting speedups.

M Tasks	$F_s$	$S_{1,2}$	$S_{1,8}$	$S_{1,16}$
50	1.33 E-1	1.90 [1.76]	5.23 [4.14]	6.35 [5.34]
74	9.40 E-2	1.90 [1.83]	5.62 [4.82]	9.00 [6.64]
100	7.13 E-2	1.88 [1.87]	6.11 [5.34]	9.38 [7.73]
200	3.70 E-2	- [1.93]	5.98 [6.36]	11.85 [10.29]
473	1.60 E-2	- [1.97]	[7.20]	12.35 [12.91]

Table 6.3 Speed up summaries for analyses for serial and multithreaded processes. M tasks is the number of functional-parallel tasks ran for the computation.  $S_{p,c}$  is a single speedup comparison for runs utilizing  $p$  nodes and  $c$  threads. [·] are the estimated speedups calculated from Tab. 6.2, Eq. (6.10), and Eq. (6.5). Empty entries are indicated with '-'.

1297 We see a speedup that generally exceeds expectations from Eq. (6.5) for real trail runs. We also  
 1298 see that there are diminishing returns as the number of threads increases. For small jobs with large  $c$ ,  
 1299 both the expected and observed speedup are significantly smaller than  $c$ . One thing not considered  
 1300 in Eq. (6.5) is the time incurred via communication latency. Communication latency increases  
 1301 with the number of threads and contributes to diminishing returns. Additionally, these values are  
 1302 for single runs and do not consider the stochastic variation expected in a shared high performance  
 1303 computing resource. Therefor, these results are not strictly conclusive, yet demonstrate the merits  
 1304 of multi-threading. We see very clearly that there is a lot to gain, and this new coding pattern will  
 1305 expand HAWC's analysis capabilities.

## 1306 6.6 Analysis Results

1307 3 of the 43  $\mathcal{LS}$  dSphs considered for the multithreaded analysis. These dSph are analyzed for  
 1308 emission from DM annihilation according to the likelihood method described in Section 5.4. The 3  
 1309 likelihood profiles are then stacked to synthesize a combined limit on the dark matter cross-section,  
 1310  $\langle\sigma v\rangle$ . This combination is done for the 17 SM annihilation channels. Figure 6.7 and Fig. 6.8 show  
 1311 the combined limits for all annihilation channels with HAWC's observations. Test statistics of the  
 1312 best fit  $\langle\sigma v\rangle$  values for each DM mass and SM annihilation channels are shown in Fig. 6.9 and  
 1313 Fig. 6.10. We also compare these limits to HAWC's Glory Duck limits shown in Section 5.5. The  
 1314 comparison to Glory Duck are featured in Fig. 6.11 for all the DM annihilation channels studied  
 1315 for Glory Duck. A full comparison is provided in the appendix in Fig. B.2, Fig. B.3, and Fig. B.4.  
 1316 Here, we show updated limits for  $\chi\chi \rightarrow b\bar{b}, e\bar{e}, \mu\bar{\mu}, \tau\bar{\tau}, t\bar{t}, W^+W^-$ ,  $\gamma\gamma$  and  $ZZ$ . For the first time

ever, we show limits for  $\chi\chi \rightarrow c\bar{c}$ ,  $s\bar{s}$ ,  $u\bar{u}$ ,  $d\bar{d}$ ,  $\nu_e\bar{\nu}_e$ ,  $\nu_\mu\bar{\nu}_\mu$ ,  $\nu_\tau\bar{\nu}_\tau$ ,  $gg$ , and  $hh$ .

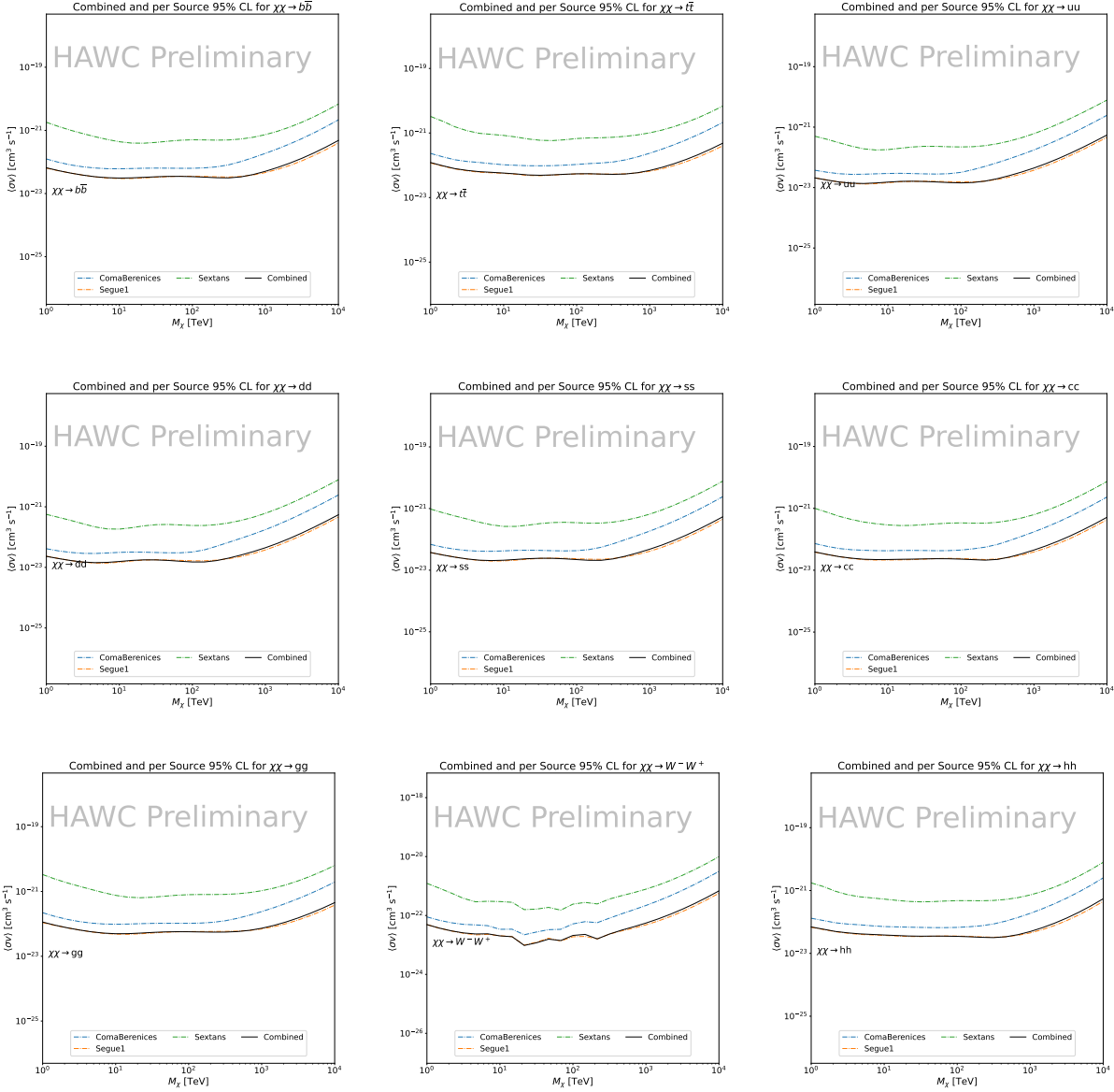


Figure 6.7 HAWC upper limits at 95% confidence level on  $\langle\sigma v\rangle$  versus DM mass for  $\chi\chi \rightarrow b\bar{b}$ ,  $t\bar{t}$ ,  $u\bar{u}$ ,  $d\bar{d}$ ,  $s\bar{s}$ ,  $c\bar{c}$ ,  $gg$ ,  $W^+W^-$ , and  $hh$ . Limits are with  $\mathcal{LS}$   $J$ -factors [65]. The solid line represents the observed combined limit. Dashed lines represent limits from individual dSphs.

No DM was found in HAWC observations. The largest excess found in HAWC data was for DM annihilating to  $W$ -bosons for  $m_\chi = 10 \text{ TeV}$  at  $2\sigma$ . HAWC's limits and excesses are dominated by Segue1. Coma Berenices shows excess at higher DM mass, yet no similar excesses were observed in Segue1. Sextans did not contribute significantly to signal excess or the combined limit as it is

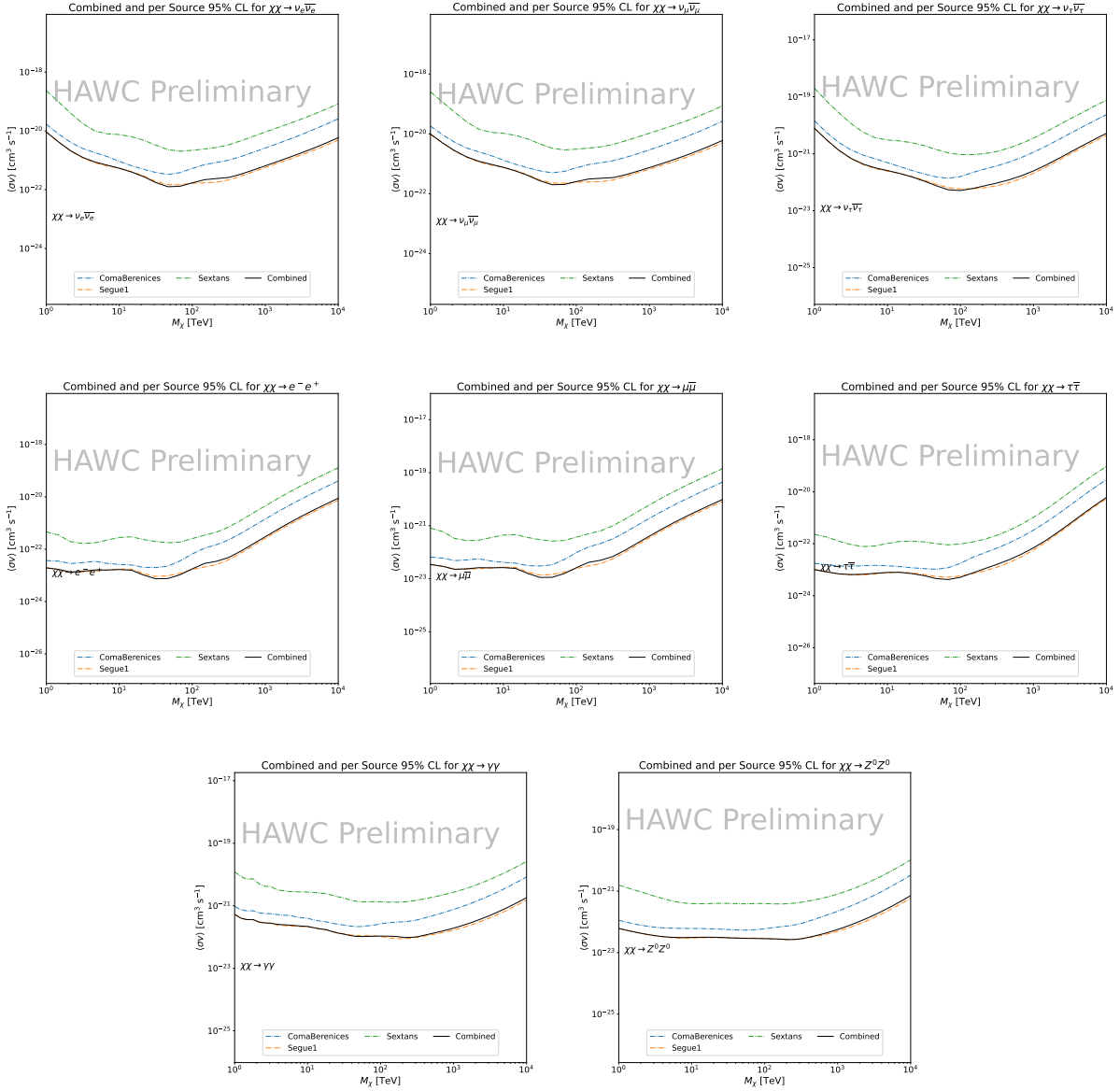


Figure 6.8 HAWC upper limits at 95% confidence level on  $\langle\sigma v\rangle$  versus DM mass for  $\chi\chi \rightarrow \nu_e \bar{\nu}_e$ ,  $\nu_\mu \bar{\nu}_\mu$ ,  $\nu_\tau \bar{\nu}_\tau$ ,  $e^- e^+$ ,  $\mu \bar{\mu}$ ,  $\tau \bar{\tau}$ ,  $\gamma \gamma$  and  $ZZ$ . Limits use  $\mathcal{L}S J$  factors [65]. The solid line represents the observed combined limit. Dashed lines represent limits from individual dSphs.

at high zenith. Draco was not included as the PDF of some of our analysis bins were wider than what is reasonable for a point source analysis. Draco is at a high zenith for HAWC, so the effort required to include it was not justified by the benefits.

We were not able to generate background trials in time of writing this thesis. These are not shown and are an immediate next step for this analysis before publication.

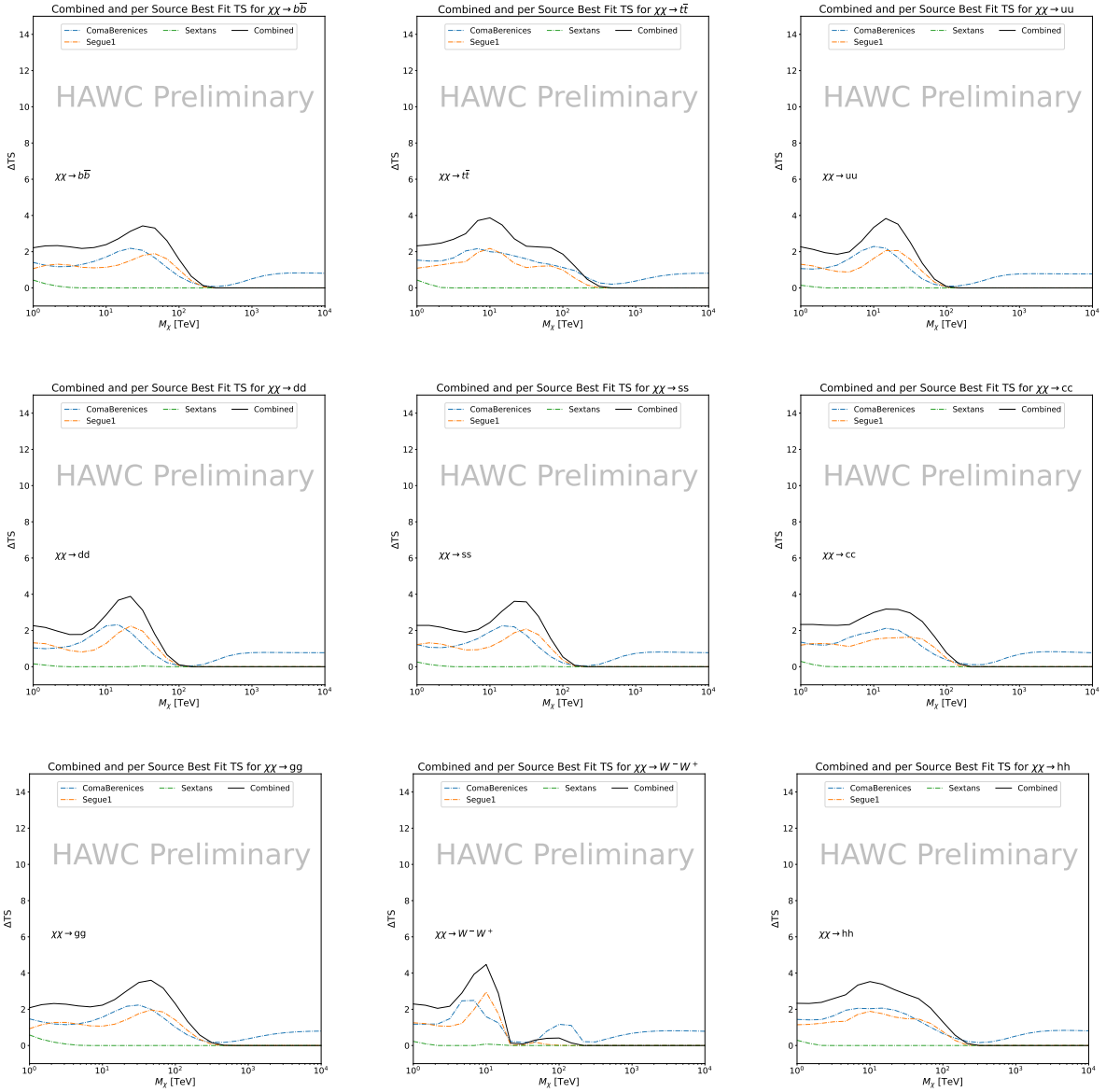


Figure 6.9 HAWC TS values for best fit  $\langle\sigma v\rangle$  versus  $m_\chi$  for SM annihilation channels:  $\chi\chi \rightarrow b\bar{b}$ ,  $t\bar{t}$ ,  $u\bar{u}$ ,  $d\bar{d}$ ,  $s\bar{s}$ ,  $c\bar{c}$ ,  $gg$ ,  $W^-W^+$ , and  $hh$ . Limits use  $\mathcal{L}\mathcal{S} J$  factors. The solid black line shows the combined best fit TS values. The colored, dashed lines are the TS values from each dSph.

When comparing these results to Section 5.5, we see an overall decrease to the confidence limit therefore improvement to HAWC's expected sensitivity. This improvement is generally stronger than a doubling of data, or a factor  $\sqrt{2}$  decrease. The comparison is somewhat complex and dependent on the dSph and SM annihilation channel. Figure 6.11 shows the comparisons of limits calculated for this analysis and Glory Duck (Section 5.5). Segue 1 and Coma Berenices are low

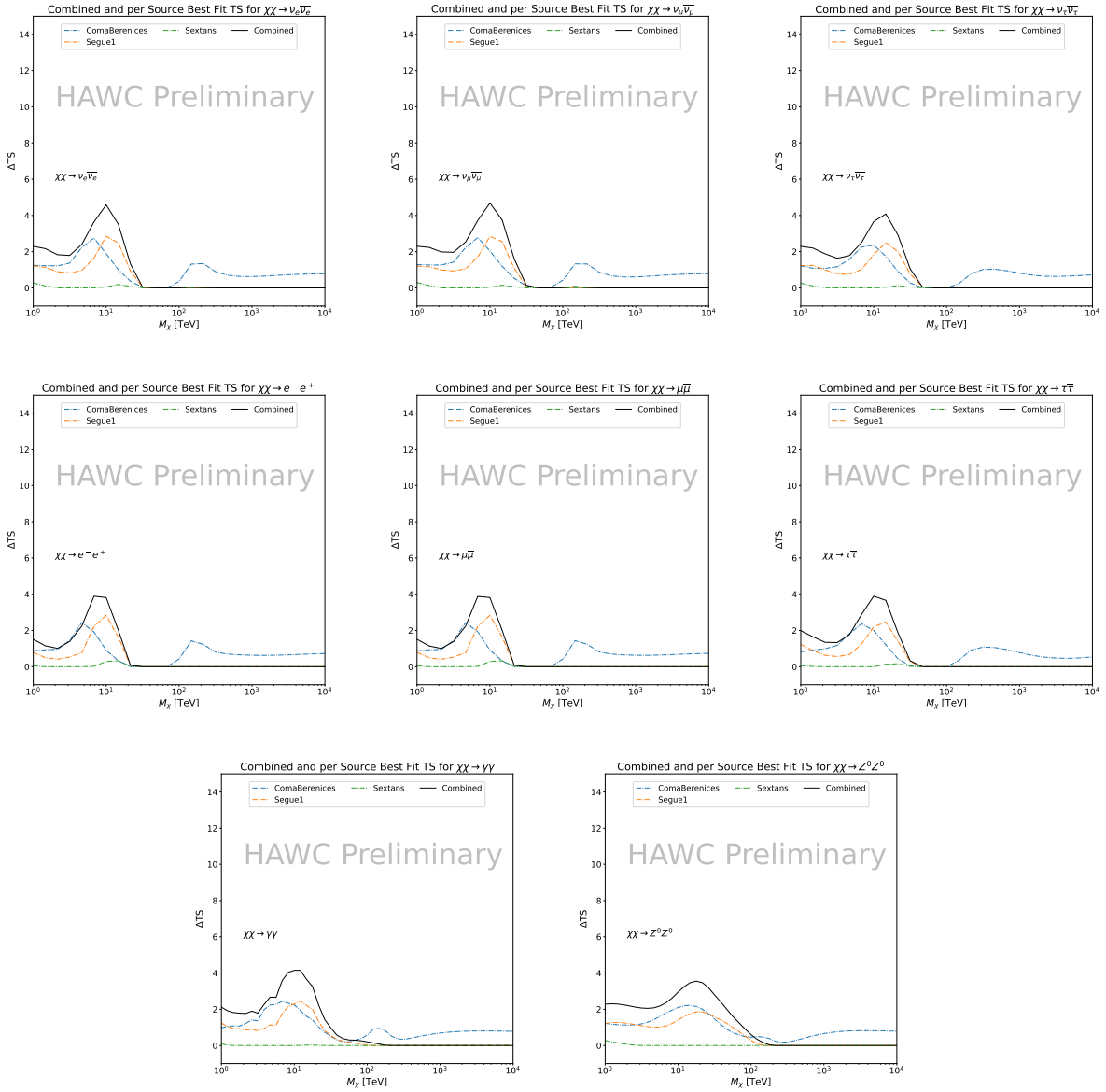


Figure 6.10 HAWC TS values for best fit  $\langle\sigma v\rangle$  versus  $m_\chi$  for SM annihilation channels:  $\chi\chi \rightarrow \nu_e \bar{\nu}_e$ ,  $\nu_\mu \bar{\nu}_\mu$ ,  $\nu_\tau \bar{\nu}_\tau$ ,  $e \bar{e}$ ,  $\mu \bar{\mu}$ ,  $\tau \bar{\tau}$ ,  $\gamma\gamma$  and  $ZZ$ . Limits use  $\mathcal{L}\mathcal{S} J$  factors. The solid black line shows the combined best fit TS values. The colored, dashed lines are the TS values from each dSph.

zenith where improvements to HAWC's analysis come only from energy estimation. Differences between these two are dominantly from their differences in  $J$ -factor, half-light radii of the dSphs, and the particle physics inputs. Substantial gains in HAWC's analysis methods (pass 5.F) were made at high zenith which is important for sources like Sextans. The HDM particle physics model produces almost identical spectra to the PPPC for  $\chi\chi \rightarrow e^- e^+$ , so can be used to compare limits

1337 between dSph. Overhead sources see minimal improvement to the limits, while high zenith sources  
1338 see an order of magnitude improvement for all DM masses. Softer SM annihilation channels see  
1339 broad improvements to the limit compared to harder channels.

1340 **6.7 Systematics**

1341 These are identical to what was performed earlier in Glory Duck, Section 5.7. We are also  
1342 sensitive to the choice in spatial template, and this was explored in Section 5.7.2 and Section 5.8.2.

1343 **6.8 Conclusion and Discussion**

1344 In this multithreaded analysis, we have used observations of 3 dSphs from HAWC to perform  
1345 a collective DM search for annihilation signals. The data were combined across sources to signifi-  
1346 cantly increase the sensitivity of the search. Advanced computational techniques were deployed to  
1347 accelerate wall-time spent analyzing by an order of magnitude. We have observed no significant  
1348 deviation from the null, no DM, hypothesis, and so present our results in terms of upper limits on  
1349 the annihilation cross-section for seventeen potential DM annihilation channels across four decades  
1350 of DM mass.

1351 This analysis serves as a proof of concept for multithreaded HAWC analyses with large parameter  
1352 spaces. Larger datasets with fast techniques will be essential to tackling the DM problem. The  
1353 models we used for this study include annihilation channels with neutrinos in the final state.  
1354 Advanced studies could aim to merge our results with those from neutrino observatories with large  
1355 data sets.

1356 A full HAWC analysis will include systematic studies of the  $J$ -factor distributions. Additionally,  
1357 because of the timing reduction, the study can be doubled in size to include DM decay. We have no  
1358 yet received the remaining spatial profiles to the  $\mathcal{LS}$  catalog, and limits can be quickly computed  
1359 once these are received. Finally, statistical studies with Poisson variation of HAWC's background  
1360 are essential to a comprehensive understanding of our observed excesses.

Segue1

Coma Berenices

Sextans

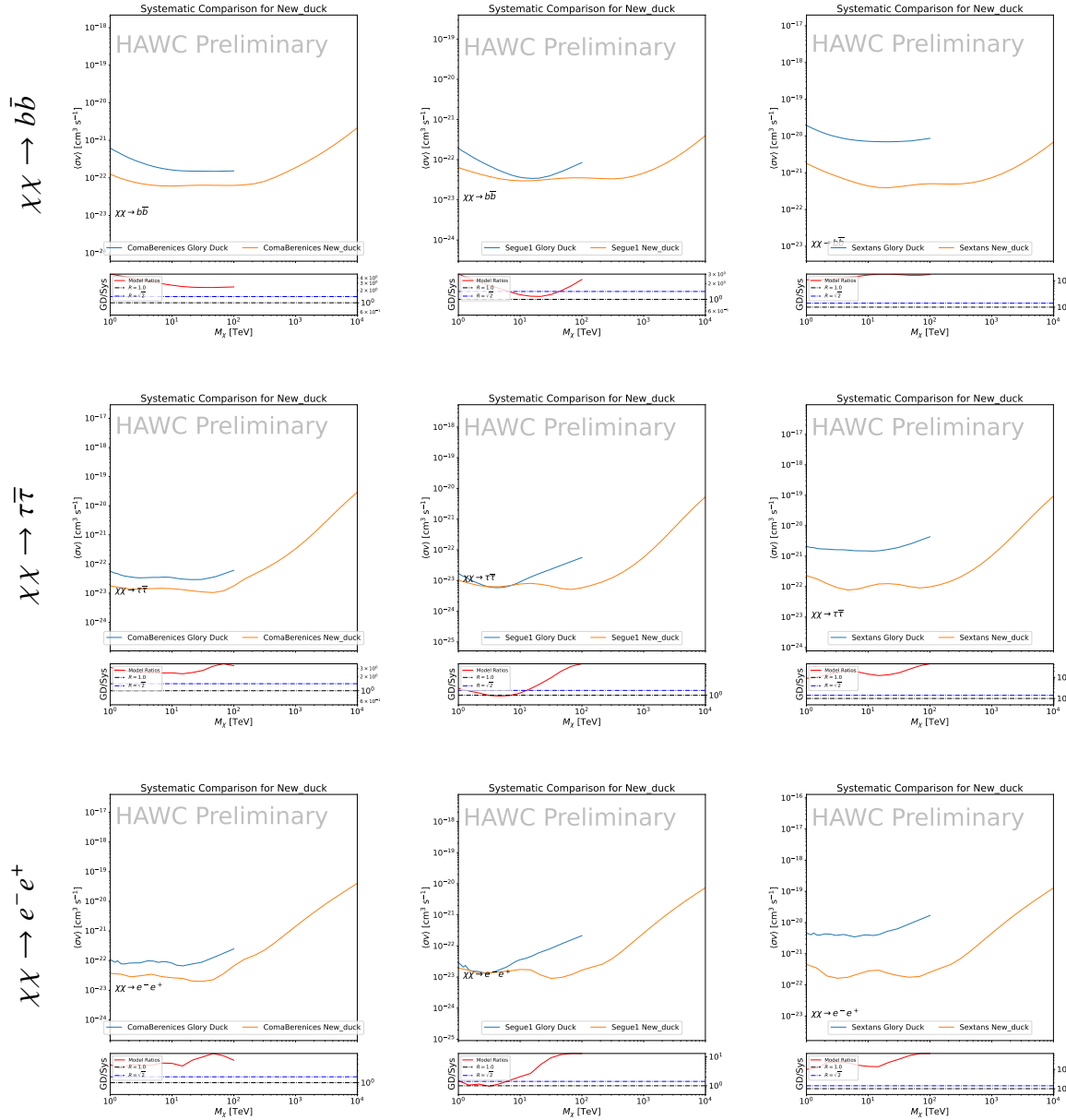


Figure 6.11 Comparison of HAWC limits from this analysis to Glory Duck (Fig. 5.5) for 3 dSphs and 3 SM annihilation channels:  $b\bar{b}$ ,  $\tau\bar{\tau}$ , and  $e\bar{e}$ . Each sector shows the 95% confidence limit from Glory Duck (blue line) and this analysis (orange line) in the top plot. The lower plot features the ratio in log scale of Glory Duck to this analysis in a red solid line. Horizontal dashed lines are for ratios of 1.0 (black) and  $\sqrt{2}$  (blue). Ratios larger than 1.0 are for limits smaller, or stricter, than Glory Duck. Ratios larger than  $\sqrt{2}$  indicates limits are stricter than a simple doubling of the Glory Duck data.

## CHAPTER 7

### 1361 HEAVY DARK MATTER ANNIHILATION SEARCH WITH ICECUBE'S NORTH SKY 1362 TRACK DATA

#### 1363 7.1 Introduction

1364 Neutrinos are another astrophysical messenger than can travel long distances without interaction.  
1365 Uniquely, they interact less readily than photons especially above PeV energies. Neutrinos thereofre  
1366 provide another window through which we can perform dark matter searches. Neutrinos come in  
1367 three flabors and so this triples the multiplicity of the particles we are searching for.

1368 Icecube has not done a DM annihilation analysis towards dwarf galaxies for a while. **TODO:**  
1369 [cite 2013 paper](#). This is in spite of the potentially crucial sensitivity afforded from neutrino spectral  
1370 lines [TODO: cite dan hooper and neutrino lines](#). A lot has changed in IC3 since that last analysis (we  
1371 have more strings, we have much more sophisticated analysis methods, and the theory modeling  
1372 has made significant leaps.) Therefore it is time to finally do a DM search toward dSphs. The hope  
1373 is that by laying down the important statistical foundation as well, that this work can be meshed  
1374 with gamma-ray data. IceCube is sensitive to annihilating DM to the DM ranges above 1 TeV  
1375 and can produce competitive results relative to gamma ray observatories in spectral models that  
1376 produce sharp neutrino features. The goal of this analysis is to perform a DM annihilation search  
1377 using the new datasets NST. The search will only be towards dwarf spheroidal galaxies (dSph).  
1378 These sources are known for their low backgrounds and high DM contents. Since the dataset is  
1379 sensitive to the north and south, as many dSph as possible will be included. Additionally, with  
1380 annihilation, these sources can be treated as point sources with little loss to sensitivity or model  
1381 dependence on how the DM is distributed. DM masses from 500 GeV to 100 PeV are considered  
1382 for this analysis. All standard model annihilation channels available from the HDMspectra are  
1383 studied in this analysis.

1384 Additional work is done to extract the Likelihood profiles for each DM, source hypothesis so  
1385 that these data can be combined with gamma-ray observatories. This work is considered a separate  
1386 project as the statistical treatment is unique from many IceCube analyses. The wiki for [ the

1387 combined analysis] **TODO: instead point to chapter**This chapter presents the analysis work for  
1388 IC3 for DM searches toward dSphs. This section describes the various steps and features of the  
1389 analysis. It is structure first introduces the data and how it is treated, then systematic studies of the  
1390 dwarves individually. Finally, the stacked analysis and results are presented.

1391 **7.2 Dataset and Background**

1392 This section enumerates the data and background methods used for IceCube's study of dSphs.  
1393 Section 7.2.1 and Section 7.2.2 are most useful for fellow IceCube collaborators looking to replicate  
1394 this analysis.

1395 **7.2.1 Itemized IceCube files**

- 1396 • Software Environment: CVMFS Py3-v4.1.1
- 1397 • Data Sample: Northern Tracks NY86v5p1
- 1398 • Analysis Software: csky ([nu\\_dark\\_matter](#))
- 1399 • Analysis wiki: [https://wiki.icecube.wisc.edu/index.php/Dark\\_Matter\\_Annihilation\\_Search\\_towards\\_dwarf\\_spheroidals\\_with\\_NST\\_and\\_DNN\\_Cascades](https://wiki.icecube.wisc.edu/index.php/Dark_Matter_Annihilation_Search_towards_dwarf_spheroidals_with_NST_and_DNN_Cascades)
- 1401 • Project repository

1402 **7.2.2 Software Tools and Development**

1403 This analysis was performed inside IceCube's CVMFS (3.4.1.1) software environment using  
1404 csky for likelihood calculations. Csky did not come with dark matter spectral models nor could  
1405 accomodate custom flux models. We developed these capacities for single source and stacked  
1406 source studies for this analysis. The analysis code is held in a separate repository from csky. The  
1407 [nu\\_dark\\_matter](#) branch of csky manages the input of custom dark matter spectra and accompanied  
1408 DM astrophysical source then calculates likelihoods with a selected data sample. The [IceCube Dark](#)  
1409 [Matter dSph repository](#) manages the generation of spectral models for neutrinos, physics parameter  
1410 extraction from  $n_{\text{sig}}$ ,  $J$ -factor per source inputs, and bookkeeping for the large parameter space.  
1411 The project repository required a secondary software environment for neutrino oscillations. How

1412 to launch and run those calculations are documented in the project repository and the Docker image  
1413 is additionally saved in Section C.1

1414 **7.2.3 Data Set and Background Description**

1415 For this analysis, I use the Northern Sky Tracks (NST) Sample (Version V005-P01). The sample  
1416 contains up-going track-like events, usually from  $\nu_\mu$  and  $\nu_\tau$  and has a superior angular resolution  
1417 compared to the cascade dataset. This sample covers 10.4 years of data (IC86\_2011-2021). The  
1418 accepted neutrino energy range used for the analysis is unique from most other IceCube searches  
1419 because DM spectra are very hard. The sampled energy range is  $1 < \log(E_\nu/\text{GeV}) < 9.51$  with  
1420 step size 0.125.

1421 The strength of a dwarf analysis is that there is no additional background consideration beyond  
1422 nominal, baseline background estimations. For NST, the nominal contribution comes from atmo-  
1423 spheric neutrinos and isotropic astrophysical neutrinos. We estimate the background by scrambling  
1424 NST data along Right Ascension.

1425 **7.3 Analysis**

1426 The expected differential neutrino flux from DM-DM annihilation to standard model particles,  
1427  $d\Phi_\nu/dE_\nu$ , over solid angle,  $\Omega$  is described by the familiar equation.

$$\frac{d\Phi_\nu}{dE_\nu} = \frac{\langle\sigma v\rangle}{8\pi m_\chi^2} \frac{dN_\nu}{dE_\nu} \times \int_{\text{source}} d\Omega \int_{l.o.s} \rho_\chi^2 dl(r, \theta') \quad (7.1)$$

1428 This is identical to past examples except that there are 3 neutrino flavors, so there are a corresponding  
1429 3 flux equations. Section 5.3 has a complete description of all the terms. Additionally, neutrinos  
1430 oscillate between flavors which needs to be considered for the expected neutrino flux at Earth.  
1431 Section 7.3.1 presents the particle physics model for DM annihilation. Section 7.3.2 presents the  
1432 spatial distributions built for each dSph.

1433 **7.3.1  $\frac{dN_\nu}{dE_\nu}$  - Particle Physics Component**

1434 Neutrino spectra from heavy dark matter annihilation were generated using HDMSSpectra [64]  
1435 and  $\chi$ arrov [68]. HDMSSpectra simulates the decay and annihilation of heavy dark matter, for  
1436 different dark matter masses and SM primary annihilation channels. The simulation includes

1437 electroweak radiative corrections and higher order loop corrections with quarks. This publication  
1438 also pushes the simulated DM mass to the Plank scale (1 EeV), however this study will not explore  
1439 that high.

1440 An important novel feature in the spectra is that neutrino line channels will be accompanied  
1441 with a low energy tail. Thus the earth will not fully attenuate a neutrino SM channel signal from  
1442 high declination sources where the neutrino flux must first traverse through the Earth. The SM  
1443 annihilation channels that feature lines include all leptonic channels. ( $\nu_{e,\mu,\tau}$ ,  $e$ ,  $\mu$ , and  $\tau$ ) We use  
1444 [Xarov](#) to propagate and oscillate the neutrinos from the source to Earth. Because these sources are  
1445 quite large in absolute terms, and also far (order 10 kpc or more), the resulting flavor spectra are  
1446 the averages of the transition probabilities [68]:

$$P(\nu_\alpha \rightarrow \nu_\beta) \approx \begin{bmatrix} 0.55 & 0.18 & 0.27 \\ 0.18 & 0.44 & 0.38 \\ 0.27 & 0.38 & 0.35 \end{bmatrix} \quad (7.2)$$

1447 When calculating the expected contribution to  $n_s$ , only  $\nu_\mu$ ,  $\nu_\tau$  are considered as NST's effective  
1448 area to  $\nu_e$  is essentially 0. With these consideration, the expected composite neutrino spectrum  
1449 is a average of the two flavors:  $(\nu_\mu + \nu_\tau)/2$ . The spectral tables are then converted to splines to  
1450 condense information, enable random sampling of the spectra, and enable faster computation times.  
1451 The spectral splines are finally implemented as a DM class in csky. Examples of the spectra before  
1452 and after propagation are shown in Fig. 7.1.

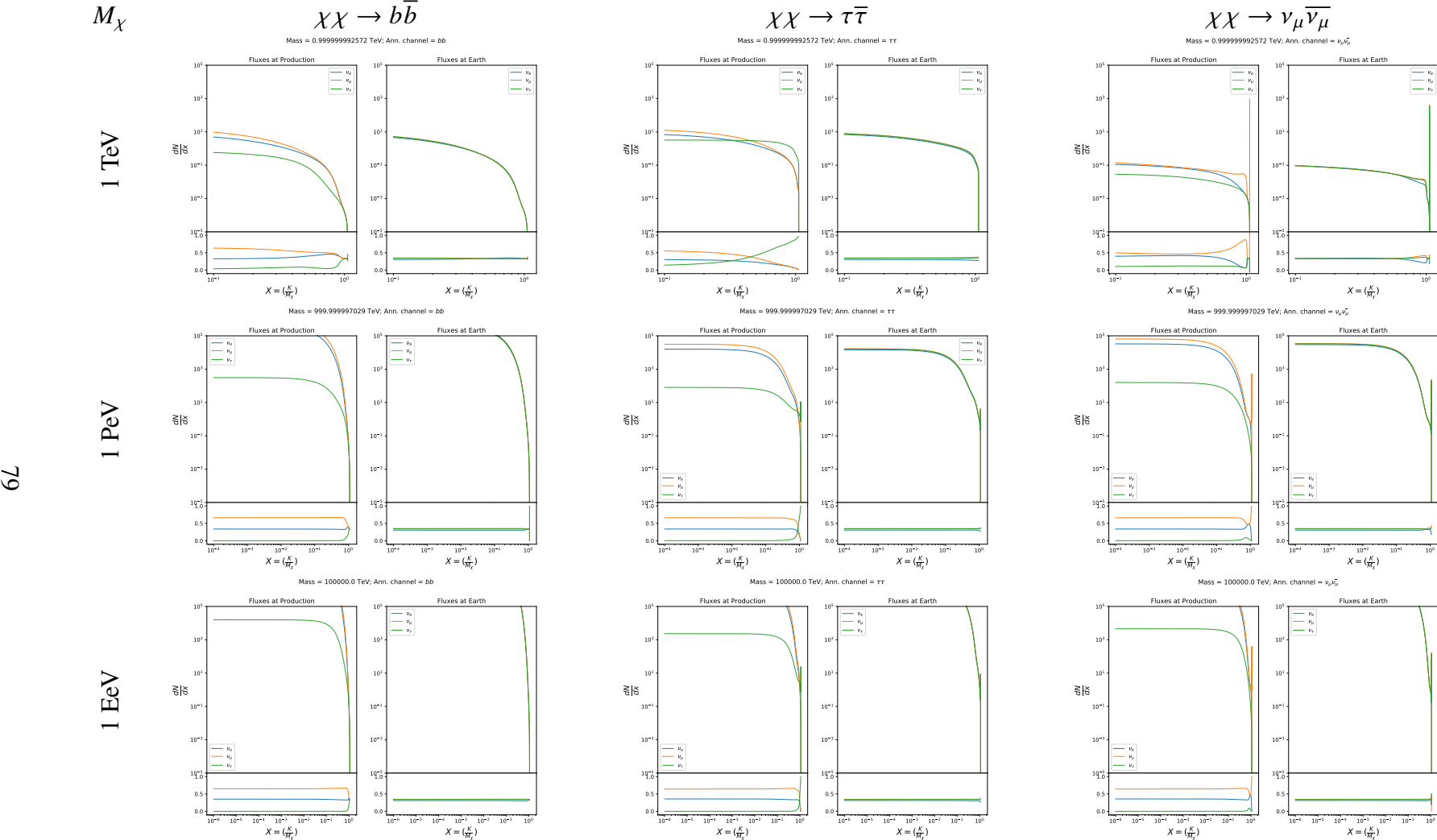


Figure 7.1 Neutrino spectra at production (left panels) and after oscillation at Earth (right panels). Blue, orange, and green lines are the  $\nu_e$ ,  $\nu_\mu$ , and  $\nu_\tau$  spectra respectively. Top panels show the spectra in  $\frac{dN}{dE}$ . Lower panels plot the flavor ratio to  $\nu_e + \nu_\mu + \nu_\tau$ . SM annihilation channels  $b\bar{b}$ ,  $\tau\bar{\tau}$ , and  $\nu_\mu \bar{\nu}_\mu$  are shown for  $M_\chi = 1 \text{ PeV}$ ,  $\text{TeV}$ , and  $\text{EeV}$ .

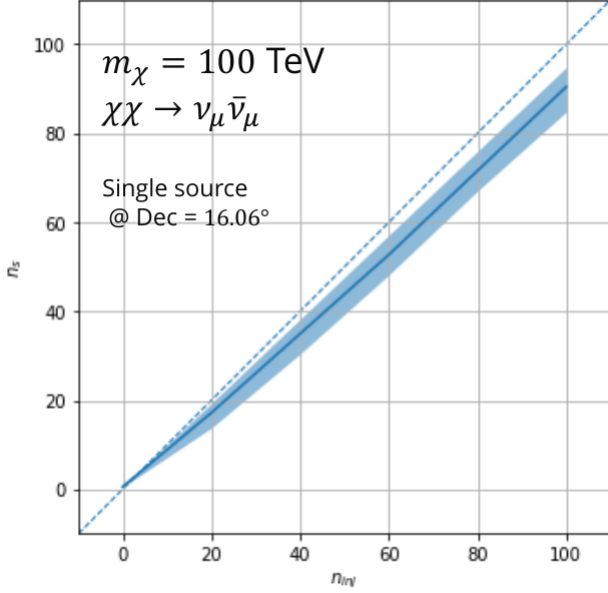


Figure 7.2 Signal recovery for 100 TeV DM annihilation into  $\nu_\mu \bar{\nu}_\mu$  for a source at Dec = 16.06°.  $n_{\text{inj}}$  is the number of injected signal events in simulation.  $n_s$  is the number of reconstructed signal events from the simulation. Although the uncertainties are small and tight, the reconstructed  $n_s$  are systematically underestimated.

### 7.3.1.1 Treatment of Neutrino Line Features

All leptonic DM annihilation channels  $\chi\chi \rightarrow [\nu_{e,\mu,\tau}, e, \mu, \tau]$  develop a prominent and narrow spectral line feature. For all neutrino flavors, this line is visible and prominent in all mass models studied for this analysis. For charged leptons, the feature only really shows up at the larger DM mass models. Examples for lines in both neutrinos and charged leptons annihilation are provided in Fig. 7.1. This line feature is so narrow relative the sampled energy range that the MC rarely samples within the neutrino line. As a result, often the best fit to simulation of background will always floor to TS = 0 and the signal recovery tends to be conservative.

To remedy this, a similar approach to the IceCube’s decay analysis [TODO: refer to Minjin’s page](#). 2 kernels were tested (Gaussian, uniform (flat)) to smooth out the line feature. The widths were tuned such that the signal recovery approached unity for DM mass 100 TeV to 1 PeV. Additionally, the tuning was performed only for a source at declination 16.06 (Segue 1). This is to avoid confusion loss in signal recovery from too narrow a line and from Earth’s attenuation of high energy neutrinos. The convolution also needed to as close as possible preserve the integrated counts of neutrinos. The optimized kernel window for all lines is summarized as:

- 1468 • Gaussian kernel w/ $2\sigma$  width =  $3.5E-3 \cdot m_\chi$
- 1469 • Minimum energy included in convolution =  $\text{MIN}[0.995 \cdot m_\chi, En(\nu_{line}) - 4\sigma]$
- 1470 • Maximum energy included in convolution =  $\text{MAX}[1.005 \cdot m_\chi, En(\nu_{line}) + 4\sigma]$

1471 where  $En(\nu_{line})$  is the neutrino energy where the neutrino line is at the maximum.

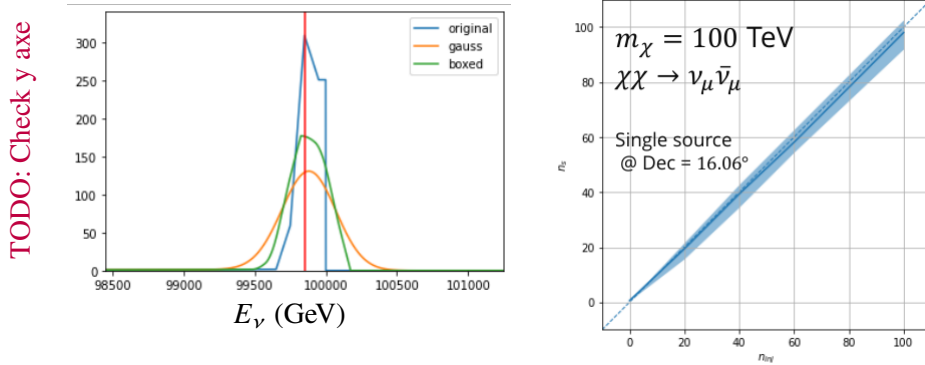


Figure 7.3 Top left panel shows the two kernels overlaid the original spectrum from Charon. delta I is the difference in the integral of the peaks with respect to the original spectrum. The vertical red line indicated where the original neutrino line is maximized. Lower right shows the signal recoveries of the DM model using the Gaussian kernel with parameters enumerated above.

1472 These parameters broadly improved the signal recovery of the line spectra. An example is  
1473 provided below. Signal recovery plots of the full analysis are provided much further down.

### 1474 7.3.1.2 Spline Fitting

1475 In an effort to reduce computational work, memory burden, and align with point source methods  
1476 used for NGC1068 and Seyfert analyses, spectral splines were created and adopted for estimating  
1477 the neutrino flux for the different annihilation. Software was written to generate, handle, and  
1478 calculate values on the splines. When using splines, one has to be careful of the goodness to fit.  
1479 There are critical caveats when testing the goodness to fit to MC generated above for all channels.

- 1480 • The splines must be Log10(\*) in Energy and dN/dE to account for the exponential nature of  
1481 the flux
- 1482 • The fidelity of the fit matters more at  $E_\nu \approx m_\chi$  where the model uncertainties are minimal  
1483 and physical considerations (like the cut-off) are most apparent.

- 1484 • The fidelity of the fit matters less at low  $E_\nu$  as the model uncertainties are large AND  
 1485 IceCube's sensitivity diminishes significantly below 500 GeV

- 1486 • Total integrated counts should be well preserved, however, the resolution of the MC is much  
 1487 higher than IceCube's energy resolution.

1488 – Meaning over several steps in E, the integral is preserved

1489 – the step size enters the cost function

1490 – Oscillating residuals, so long as they are very small and well centered, are not penalized  
 1491 as this gets averaged out.

1492 The resulting cost function to evaluate the goodness of fit was used to account for the above  
 1493 considerations.

$$e_i = x_i \cdot \left( \frac{dN_i}{dE_i} - 10^{\hat{e}_i} \right) \quad (7.3)$$

1494 Where  $\hat{e}_i$  is the spline estimator's value for  $x_i$ .  $x_i = E_{\nu_i}/m_\chi$ .  $\frac{dN_i}{dE_i}$  is the flux value from MC.

$$\text{err} = \sqrt{\frac{1}{x_{\max} - x_{\min}} \int_{x_{\min}}^{x_{\max}} e^2 dx} \quad (7.4)$$

1495 I then take the RMS of the error distribution and the resulting value (err) is used to evaluate  
 1496 the fidelity of the spectral spline. Each SM channel had different tolerances for 'err'. Channels  
 1497 with very hard cut-offs had looser tolerance for err because a lot of error would be generated from  
 1498 the cut-off being estimated to occur slightly early or late. Soft channels don't have this issue and  
 1499 therefore the tolerance is very strict. The table blow summarizes the tolerances for the SM channels.

### 1500 7.3.2 J- Astrophysical Component

1501

## **CHAPTER 8**

### **NU DUCK**

## MULTI-EXPERIMENT SUPPLEMENTARY FIGURES

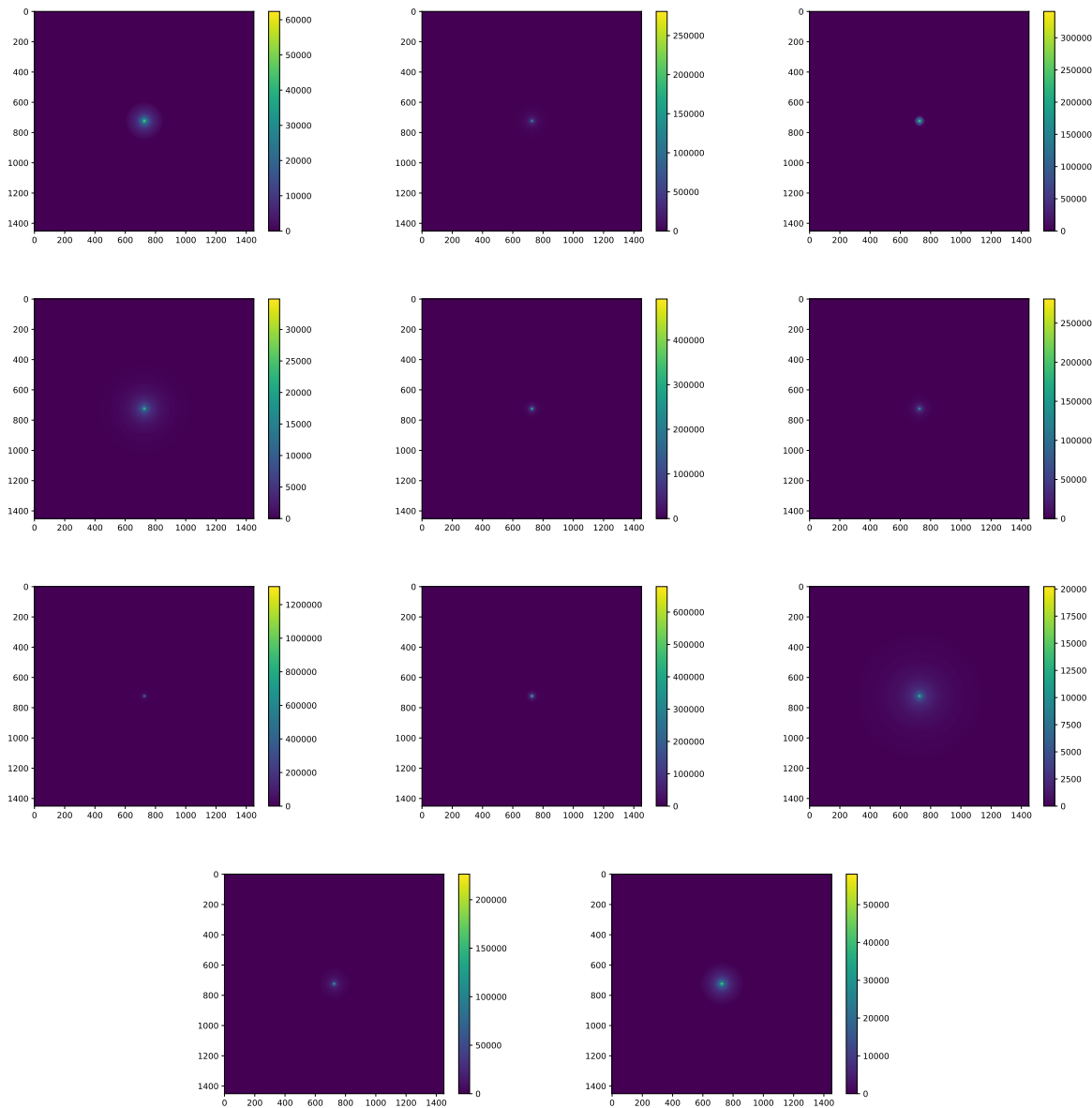


Figure A.1 Sister figure to Figure 5.3. Sources in the first row from left to right: Bootes I, Canes Venatici I, II. In second row: Draco, Hercules, Leo I. In the first row: Leo II, Leo IV, Sextans. In the final row: Ursa Major I, Ursa Major II.

## APPENDIX B

### 1503 MULTITHREADING DARK MATTER ANALYSES SUPPLEMENTARY MATERIAL

#### 1504 B.1 Remaining Spectral Models

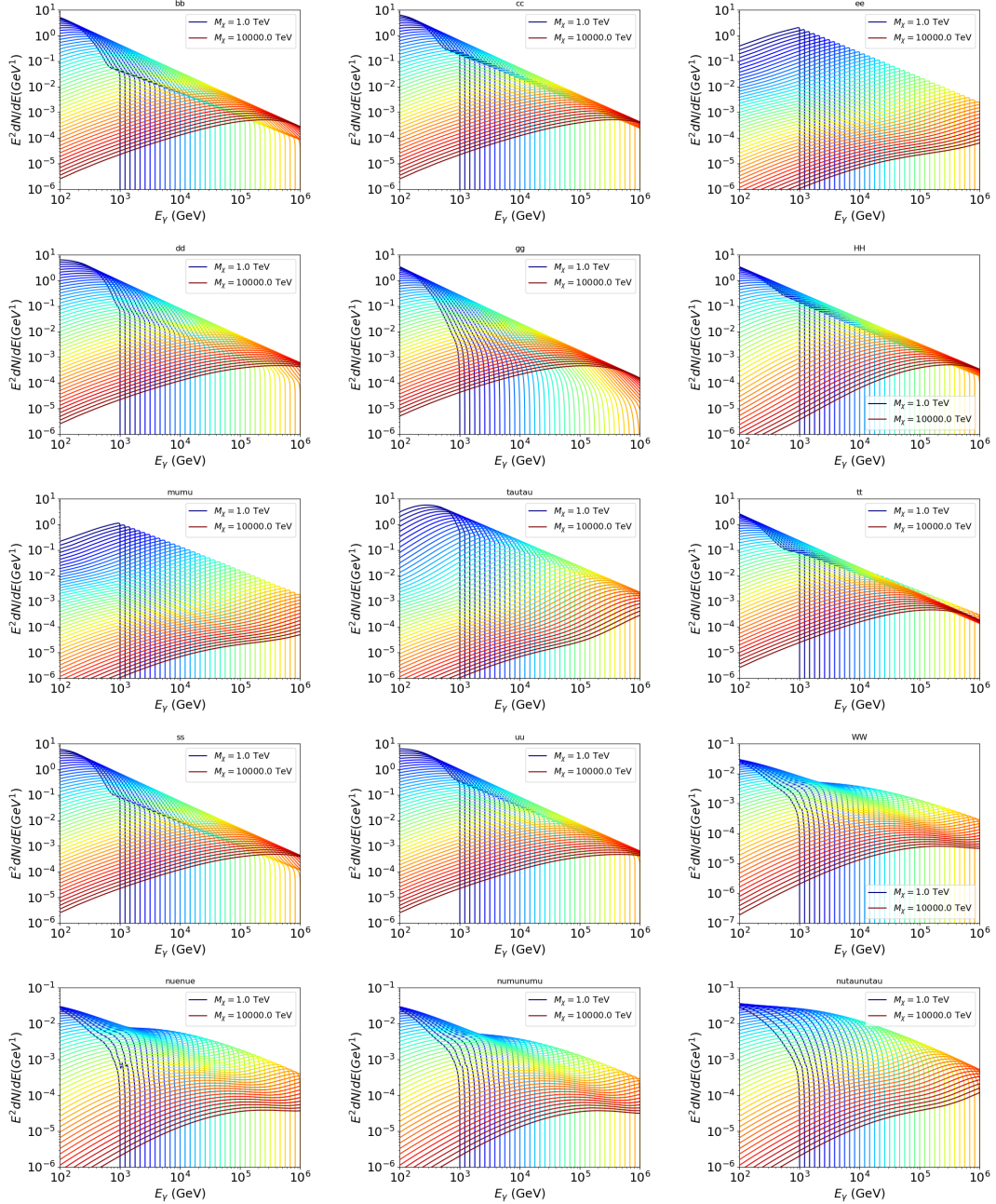


Figure B.1 Sister figure to Figure 6.2 for remaining SM primary annihilation channels studied for this thesis. These did not require any post generation smoothing and so are directly pulled from [64] with a binning scheme most helpful for a HAWC analysis.

## 1505 B.2 mpu\_analysis.py

```
15061 import warnings
15072 with warnings.catch_warnings():
15083     warnings.simplefilter("ignore")
15094 # Python base libraries
15105 import os
15116 import sys
15127 import time
15138 # Import general libraries with namespace
15149 import matplotlib
15150 # Necessary for computing on cluster
15161 matplotlib.use("agg")
15172 import numpy as np
15183 import multiprocessing as mp
15194 # Import HAWC software
15205 sys.path.insert(1, os.path.join(os.environ['HOME'], 'hawc_software', 'threeML-
1521     analysis-scripts', 'fitModel'))
15226 from analysis_modules import *
15237 from threeML import *
15248 from hawc_hal import HAL, HealpixConeROI
15259 from threeML.minimizer.minimization import FitFailed
15260 # Import Dark Matter HAWC Libraries
15271 import analysis_utils as au
15282 import spectra as spec
15293 import sources as srcs
15304
15315 #* READ ONLY PATHS This block will change eventually
15326 MASS_LIST = './plotting/studies/nd/masses.txt'
15337 CHAN_LIST = './plotting/studies/nd/chans.txt'
15348
15359 #* WRITE PATHS, default location is to scratch
15360 OUT_PATH = os.path.join(os.environ["SCRATCH"], os.environ["USER"], 'New_duck')
```

```

15371 print('Our out path is going to be {}'.format(OUT_PATH))
15382
15393 # Define parallel Function. Can also be run serially
15404 def some_mass_fit(sigVs, datalist, shape, dSph, jfactor, mass_chan,
15415                         progress=None, log_file='', queue=None, i_job=0):
15426
15437     if progress is None:
15448         progress = [0]
15459     else: # Create log files for each thread
15460         log_file = log_file.replace('.log', '_ThreadNo_')
15471         log_file = log_file + str(i_job) + ".log"
15482         sys.stdout = open(log_file, "w")
15493
15504     fits = []
15515
15526     try:
15537         for m_c in mass_chan:
15548             print(f'Mass chan tuple: {m_c}')
15559             mass = int(m_c[0])
15560             ch = m_c[1]
15571             # Build path to output files
15582             outPath = os.path.join(OUT_PATH, ch, dSph)
15593             au.ut.ensure_dir(outPath)
15604
15615             if progress[i_job] < 0:
15626                 # If the master gets a Keyboard interrupt, commit suicide.
15637                 break
15648
15659                 ### Start Model Building for DM mass and SM channel #####
15660                 spectrum = spec.DM_models.HDMSpectra()
15671                 spectrum.set_channel(ch)
15682
15693                 myDwarf = ExtendedSource(dSph, spatial_shape=shape,

```

```

15704                     spectral_shape=spectrum)
15715
15726             spectrum.J = jfactor * u.GeV**2 / u.cm**5
15737             spectrum.sigmav = 1e-24 * u.cm**3 / u.s
15748             spectrum.set_dm_mass(mass * u.GeV)
15759
15760             spectrum.sigmav.bounds = (1e-30, 1e-12)
15771             model = Model(myDwarf)
15782             ##### End model Building #####
15793
15804             jl = JointLikelihood(model, datalist, verbose=False)
15815
15826             try:
15837                 result, lhdf = jl.fit(compute_covariance=False)
15848                 ts = -2.* (jl.minus_log_like_profile(1e-30) - jl.
1585 _current_minimum)
15869                 # Also profile the LLH vs sv
15870                 ll = jl.get_contours(spectrum.sigmav, sigVs[0],
15881                               sigVs[-1], len(sigVs),
15892                               progress=False, log=['False'])
15903
15914                 sigv_ll = au.ut.calc_95_from_profile(ll[0], ll[2])
15925                 # Write results to file
15936                 outFileLL = outPath+f"/LL_{dSph}_{ch}_mass{int(mass)}_GD.txt"
15947                 np.savetxt(outFileLL, (sigVs, ll[2]),
15958                               delimiter='\t', header='sigV\tLL\n')
15969
15970                 with open(outPath+f"/results_{dSph}_{ch}_mass{int(mass)}_GD.
1598 txt", "w") as results_file:
15991                     results_file.write("mDM [GeV]\tsigV_95\tsigV_B.F.\n")
16002
16013                     results_file.write("%i\t%.5E\t%.5E\t%.5E"%(mass, sigv_ll,
16024                                         ts, result.value[0]))

```

```

16035         # End write to file
16046     except FitFailed: # Don't kill all threads if a fit fails
16057         print("Fit failed. Go back and calculate this spectral model
1606         later")
16078             fits.append((ch, mass, -1, -1))
16089             with open(log_file+'.fail', 'w') as f_file:
16090                 f_file.write(f'{ch}, {mass}\n')
16101
16112             progress[i_job] += 1
16123             matplotlib.pyplot.close() # Prevent leaky memory
16134
16145             fits.append((ch, mass, result.value[0], ts))
16156             progress[i_job] += 1
16167             matplotlib.pyplot.close()
16178     except KeyboardInterrupt:
16189         progress[i_job] = -1
16190
16201     fits = np.array(fits)
16212     if queue is None:
16223         return fits
16234     else:
16245         queue.put((i_job, fits))
16256
16267 def main(args):
16278     masses = np.loadtxt(MASS_LIST, dtype=int)
16289     chans = np.loadtxt(CHAN_LIST, delimiter=',', dtype=str)
16290     mass_chan = au.ut.permute_lists(chans, masses)
16301
16312     print(f"DM masses for this study are: {masses}")
16323     print(f"SM Channels for this study are XX -> {chans}")
16334     print(mass_chan)
16345
16356 # extract information from input argument

```

```

16367 dSph = args.dSph
16378 data_mngr = au.ut.Data_Selector('P5_NN_2D')
16389 dm_profile = srcts.Spatial_DM(args.catalog, dSph, args.sigma, args.decay)
16390
16401 ##### Extract Source Information #####
16412 if dm_profile.get_dec() < -22.0 or dm_profile.get_dec() > 62.0:
16423     raise ValueError("HAWC can't see this source D: Exitting now...")
16434
16445 print(f'{dSph} information')
16456 print(f'jfac: {dm_profile.get_factor()}\tRA: {dm_profile.get_ra()}\tDec: {dm_profile.get_dec()}\n')
16477
16488 shape = SpatialTemplate_2D(fits_file=dm_profile.get_src_fits())
16499 ##### Finish Extract Source Information #####
16500
16511 ##### LOAD HAWC DATA #####
16522 roi = HealpixConeROI(data_radius=2.0, model_radius=8.0,
16533                         ra=dm_profile.get_ra(), dec=dm_profile.get_dec())
16544 bins = choose_bins.analysis_bins(args, dec=dm_profile.get_dec())
16555
16566 hawc = HAL(dSph, data_mngr.get_datmap(), data_mngr.get_detres(), roi)
16577 hawc.set_active_measurements(bin_list=bins)
16588 datalist = DataList(hawc)
16599 ##### FINISH LOAD HAWC DATA #####
16600
16611 # set up SigV sampling. This sample is somewhat standardized
16622 sigVs = np.logspace(-28,-18, 1001, endpoint=True) # NOTE This will change
16633 whith HDM
16643
16654 if args.n_threads == 1:
16665     # No need to start || programming just iterate over the masses
16676     kw_arg = dict(sigVs=sigVs, datalist=datalist, shape=shape, dSph=dSph,
16687                     jfactor=dm_profile.get_factor(), mass_chan=mass_chan,

```

```

16698                 log_file=args.log)
16709             some_mass_fit(**kw_arg)
16710         else:
16711             # I Really want to suppress TQMD output
16712             from tqdm import tqdm
16713             from functools import partialmethod
16714             tqdm.__init__ = partialmethod(tqdm.__init__, disable=True)
16715
16716             x = np.array_split(mass_chan, args.n_threads)
16717             n_jobs = len(x)
16718
16719
16809             print("Thread jobs summary by mass and SM channel")
16810             for xi in x:
16811                 print(f'{xi}')
16812
16813             queue = mp.Queue()
16814             progress = mp.Array('i', np.zeros(n_jobs, dtype=int))
16815
16816             # Define task pool that will be split amongsts threads
16817             kw_args = [dict(sigVs=sigVs, datalist=datalist, shape=shape,
16818                           dSph=dSph, jfactor=dm_profile.get_factor(),
16819                           mass_chan=mass_chan, progress=progress,
16820                           queue=queue, i_job=i, log_file=args.log)
16821             for i, mass_chan in enumerate(x)]
16822
16823             # Define each process
16824             procs = [mp.Process(target=some_mass_fit, kwargs=kw_args[i]) \
16825                     for i in range(n_jobs)]
16826
16827             ### Start MASTER Thread only code block ###
16828             # Begin running all child threads
16829             for proc in procs: proc.start()
16830

```

```

17021     try:
17022
17023         # In this case, the master does nothing except monitor progress of
17024         the threads
17025
17026         # In an ideal world, the master thread also does some computation.
17027
17028         n_complete = np.sum(progress)
17029
17030         while_count = 0
17031
17032
17033         while n_complete < len(mass_chan):
17034
17035             if np.any(np.asarray(progress) < 0):
17036
17037                 # This was no threads are stranded when killing the script
17038
17039                 raise KeyboardInterrupt()
17040
17041             if while_count%1000 == 0:
17042
17043                 print(f'{np.sum(progress)} of {len(mass_chan)} finished')
17044
17045
17046             n_complete = np.sum(progress)
17047
17048             time.sleep(.25)
17049
17050             while_count += 1
17051
17052
17053         except KeyboardInterrupt:
17054
17055             # signal to jobs that it's time to stop
17056
17057             for i in range(n_jobs):
17058
17059                 progress[i] = -2
17060
17061                 print('\nKeyboardInterrupt: terminating early.')
17062
17063             ### End MASTER Thread only code block ###
17064
17065
17066             fitss = [queue.get() for proc in procs]
17067
17068             print(fitss)
17069
17070             print(f'Thread statuses: {progress[:]}')
17071
17072
17073             # putting results in a file
17074
17075
17076             print("QUACK! All Done!")

```

```

1735.3
1736.4
1737.5 if __name__ == '__main__':
1738.6     import argparse
1739.7
1740.8     p = argparse.ArgumentParser(description="Run a DM annihilation analysis on
1741.9         a dwarf spheroidal for a specific SM channel for DM masses [1 TeV to 10
1742.0             PeV]")
1743.1
1744.2     # Dwarf spatial modeling arguements
1745.3     p.add_argument("-ds", "--dSph", type=str,
1746.4             help="dwarf spheroidal galaxy to be studied", required=
1747.5             True)
1748.6     p.add_argument("-cat", "--catalog", type=str, choices=['GS15', 'LS20'],
1749.7             default='LS20', help="source catalog used")
1750.8     p.add_argument("-sig", "--sigma", type=int, choices=[-1, 0, 1], default=0,
1751.9             help="Spatial model uncertainty. 0 corresponds to the
1752.0                 median. +/-1 correspond to the +/-1sigma uncertainty respectively.")
1753.1
1754.2     # Arguements for the energy estimators
1755.3     p.add_argument("-e", "--estimator", type=str,
1756.4             choices=['P5_NHIT', 'P5_NN_2D'],
1757.5             default="P5_NN_2D", required=False,
1758.6             help="The energy estimator choice. Options are: P5_NHIT,
1759.7                 P5_NN_2D. GP not supported (yet).")
1760.8     p.add_argument("--use-bins", default=None, nargs="*",
1761.9             help="Bins to use for the analysis", dest="use_bins")
1762.0     p.add_argument('--select_bins_by_energy', default=None, nargs="*",
1763.1             help="Does nothing. May fill in later once better
1764.2                 understood")
1765.3     p.add_argument('--select_bins_by_fhit', default=None, nargs="*",
1766.4             help="Also does nothing see above")
1767.5     p.add_argument( '-ex', '--exclude', default=None, nargs="*",

```

```

17680         help="Exclude Bins", dest="exclude")

17691

17702 # Computing and logging arguements.

17713 p.add_argument('-nt', '--n_threads', type=int, default=1,
17724                         help='Maximum number of threads spawned by script. Default
1773      is 4')

17745 p.add_argument('-log', '--log', type=str, required=True,
17756                         help='Name for log files. Especially needed for threads')

17767

17778 p.add_argument('--decay', action="store_true",
17789                         help='Set spectral DM hypothesis to decay')

17790

17801 args = p.parse_args()

17812 print(args.decay)

17823 if args.exclude is None: # default exclude bins 0 and 1
17834     args.exclude = ['B0C0Ea', 'B0C0Eb', 'B0C0Ec', 'B0C0Ed', 'B0C0Ee']

17845

17856 if args.decay: OUT_PATH += '_dec'
17867 else: OUT_PATH += '_ann'

17878

17889 OUT_PATH = OUT_PATH + '_' + args.catalog
17890 if args.sigma != 0: OUT_PATH += f'_{args.sigma}sig'

17901

17912 main(args)

```

1792 B.3 Comparison with Glory Duck

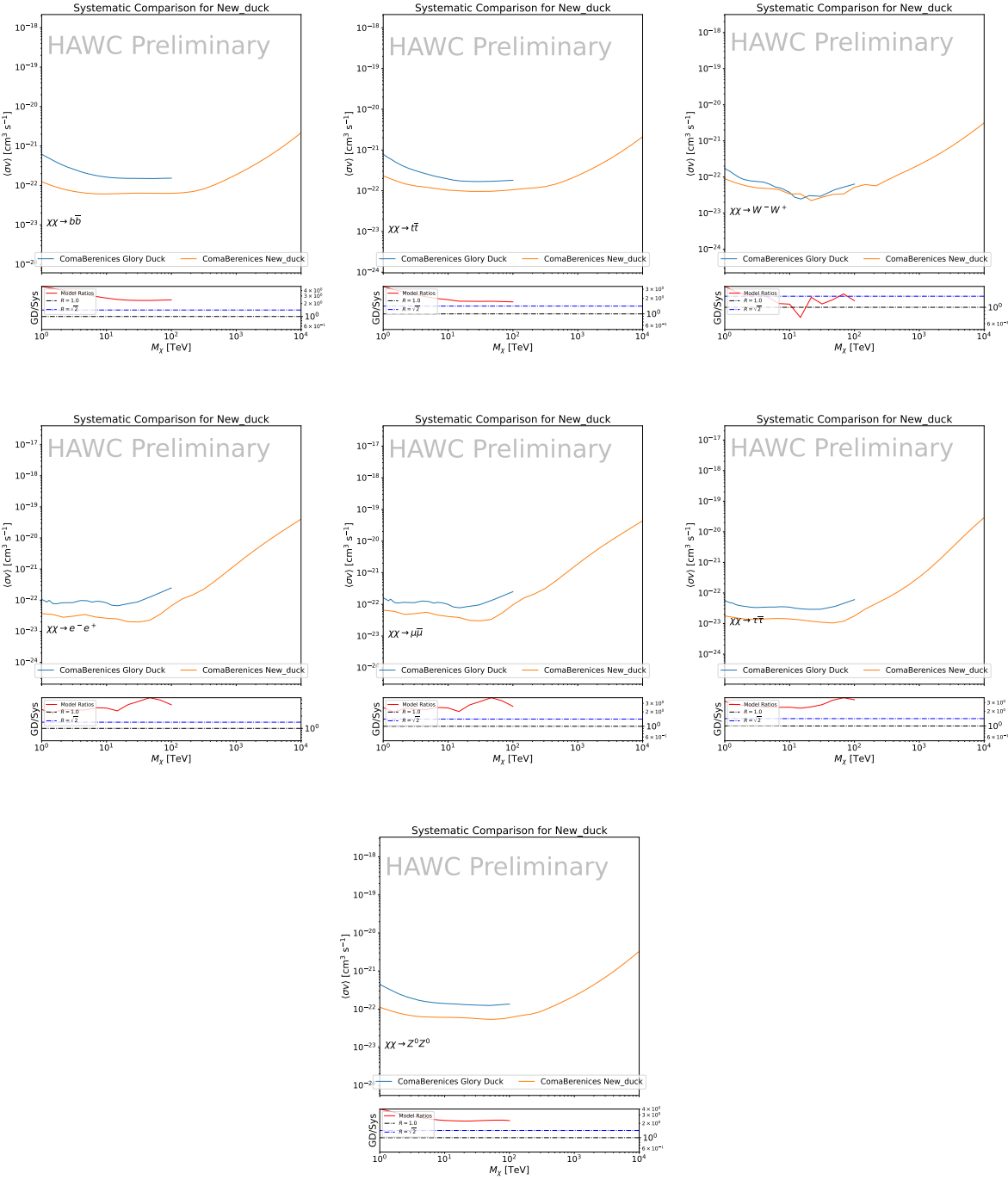


Figure B.2 TODO: fill this out

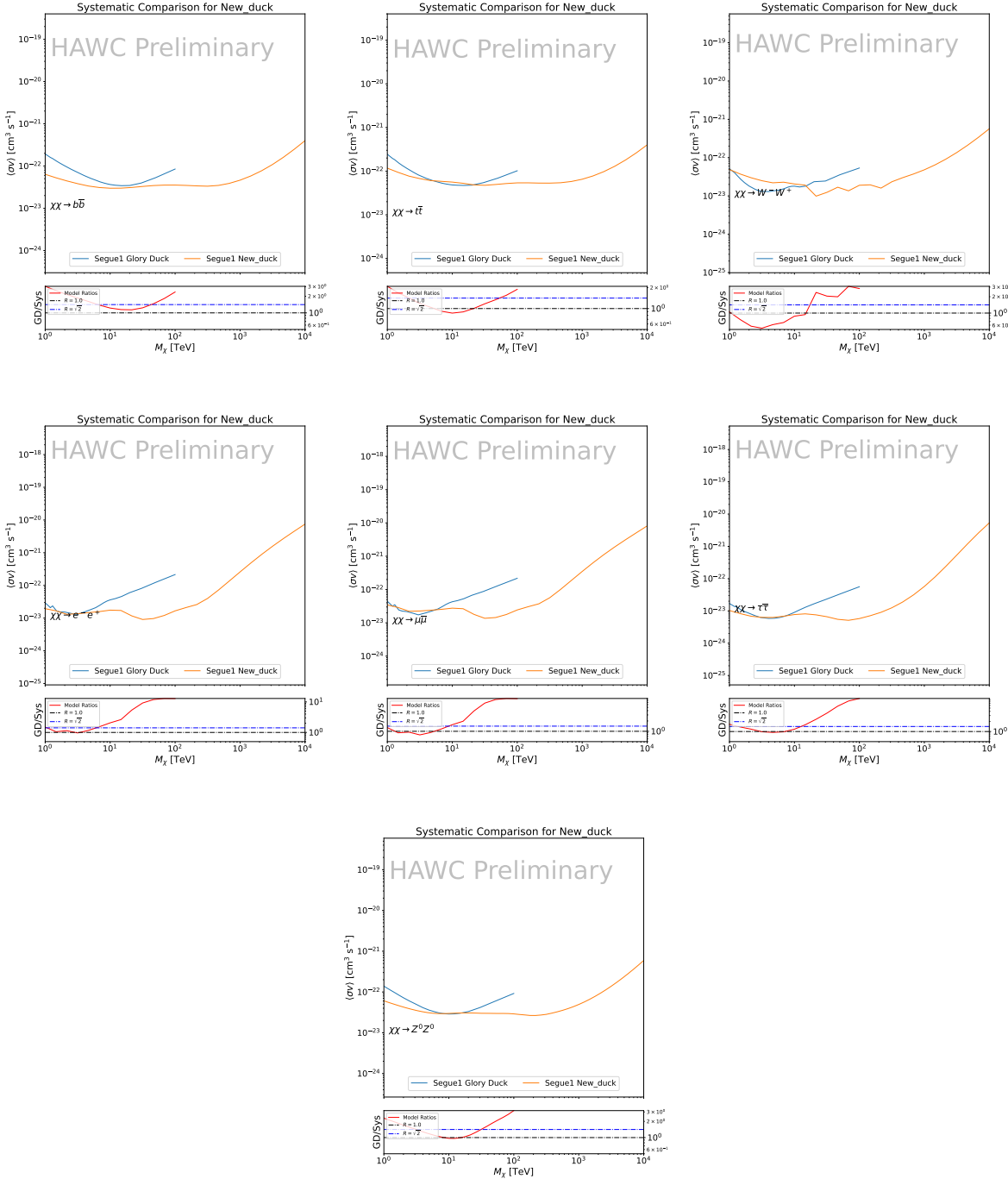


Figure B.3 TODO: fill this out

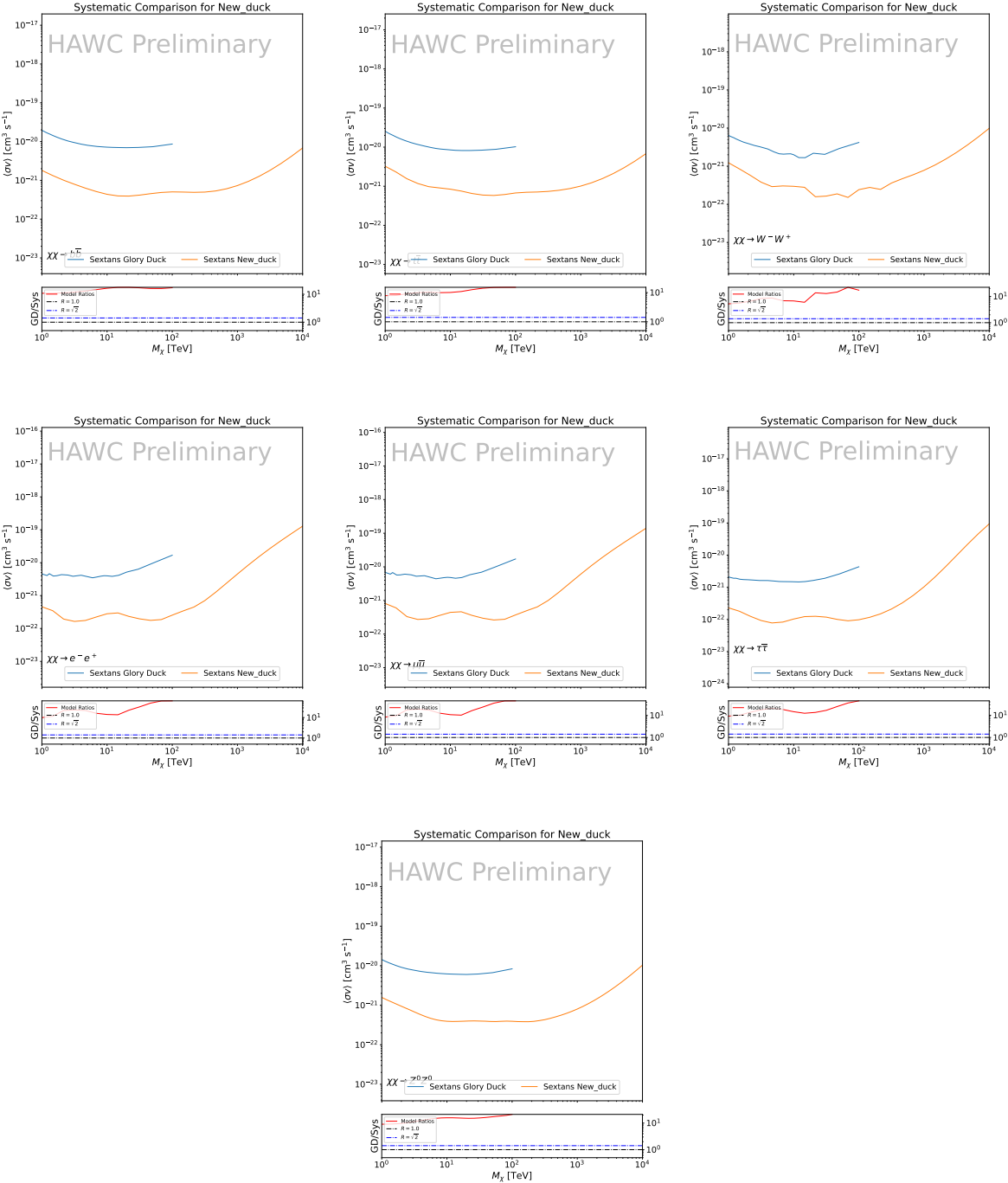


Figure B.4 TODO: fill this out

## APPENDIX C

### 1793 ICECUBE HEAVY DARK MATTER ANALYSIS SUPPLEMENTARY MATERIAL

#### 1794 C.1 Docker Image for Oscillating Neutrino Spectra

```
1795 1 FROM ubuntu:18.04
1796 2
1797 3 # Execute commands to install software packages
1798 4 RUN apt -y update
1799 5
1800 6     # Install utility programs
1801 7 RUN apt -y install vim wget git cmake
1802 8
1803 9 ARG DEBIAN_FRONTEND=noninteractive
1804 0
1805 1     # Install python
1806 2 RUN apt -y install python python-dev python-pip libjpeg-dev zlib1g-dev
1807 3
1808 4     # We need Python2 for installing Charon.
1809 5 RUN apt -y install python-numpy python-sympy python-matplotlib \
1810 6             python-sympy python-h5py python-astropy python-ipython
1811 7
1812 8     # Install dependencies of Charon : SQuIDS, NuSQuIDS
1813 9 RUN apt -y install libgsl-dev libgslcblas0 libgsl23 gsl-bin pkg-config
1814 0     # Install SQuIDS
1815 1 RUN mkdir /home/SQuIDS /home/SQuIDS_install
1816 2 WORKDIR /home/SQuIDS
1817 3 RUN git clone https://github.com/jsalvado/SQuIDS.git
1818 4 WORKDIR /home/SQuIDS/SQuIDS
1819 5 RUN git checkout 7ad9ba7c6ad06d1f0fa8418f937ebf1a403fef90
1820 6     # Before executing "make install" an environmental variable has to be set.
1821 7 ENV PKG_CONFIG_PATH=/home/SQuIDS/SQuIDS/lib
1822 8 RUN ./configure --prefix=../SQuIDS_install \
```

```

18239     && make
18240 RUN make install
18251
18262 # Set up an environmental variable that is required to install nuSQuIDS..
18273 ENV SQuIDS=/home/SQuIDS/SQuIDS
18284 ENV LD_LIBRARY_PATH=$SQuIDS/lib:$LD_LIBRARY_PATH
18295
18306 # Install NuSQuIDS
18317 RUN mkdir /home/nuSQuIDS
18328 WORKDIR /home/nuSQuIDS
18339 RUN git clone https://github.com/qrliu/nuSQuIDS.git
18340 WORKDIR /home/nuSQuIDS/nuSQuIDS
18351 RUN git checkout 072d8ef740e2fc7330f1fabaea94f0f4540c46f9
18362 RUN apt -y install libhdf5-dev hdf5-tools
18373 RUN apt -y install libboost1.65-all-dev
18384 RUN ./configure --with-squids=$SQuIDS --with-python-bindings --prefix=../
1839      nuSQuIDS_install \
18405     && make \
18416     && make install
18427
18438 # Set up an environmental variable for nuSQuIDS.
18449 ENV nuSQuIDS=/home/nuSQuIDS/nuSQuIDS
18450 ENV LD_LIBRARY_PATH=$nuSQuIDS/lib:$LD_LIBRARY_PATH
18461
18472 # Build the python bindings
18483 WORKDIR /home/nuSQuIDS/nuSQuIDS/resources/python/src
18494 RUN make
18505
18516 # Set up an environmental variable for the python bindings.
18527 ENV PYTHONPATH=$nuSQuIDS/resources/python/bindings/:$PYTHONPATH
18538
18549 # Install Charon in the /home/Charon/charon directory.
18550 RUN mkdir /home/Charon

```

```
18561 WORKDIR /home/Charon
18572 RUN git clone https://github.com/icecube/charon.git \
18583     && apt -y install unzip python-scipy
18594 WORKDIR charon
18605 RUN git checkout c531efe4e01dc364a60d1c83f950f04526ccd771
18616 RUN unzip ./charon/xsec/xsec.zip -d charon/xsec/ \
18627
18638 # Download neutrino spectra tables in the /home/Charon/charon/data directory
1864 .
18659     && mkdir ./charon/data
18660 WORKDIR ./charon/data
18671 RUN wget --no-check-certificate https://icecube.wisc.edu/~qliu/charon/
1868     SpectraEW.hdf5 \
18692     && wget --no-check-certificate https://icecube.wisc.edu/~qliu/charon/
1870     Spectra_PYTHIA.hdf5 \
18713     && wget --no-check-certificate https://icecube.wisc.edu/~qliu/charon/
1872     Spectra_noEW.hdf5
18734
18745 WORKDIR ../..
18756 RUN python setup.py install
18767 WORKDIR /home
```

## BIBLIOGRAPHY

- 1878 [1] Anne M. Green. “Dark matter in astrophysics/cosmology”. In: *SciPost Phys. Lect.*  
 1879 *Notes* (2022), p. 37. doi: [10.21468/SciPostPhysLectNotes.37](https://doi.org/10.21468/SciPostPhysLectNotes.37). URL: <https://scipost.org/10.21468/SciPostPhysLectNotes.37>.
- 1881 [2] Bing-Lin Young. “A survey of dark matter and related topics in cosmology”. In: *Frontiers*  
 1882 *of Physics* 12 (Oct. 2016). doi: <https://doi.org/10.1007/s11467-016-0583-4>.  
 1883 URL: <https://doi.org/10.1007/s11467-016-0583-4>.
- 1884 [3] Gianfranco Bertone, Dan Hooper, and Joseph Silk. “Particle dark matter: evidence,  
 1885 candidates and constraints”. In: *Physics Reports* 405.5 (2005), pp. 279–390. ISSN:  
 1886 0370-1573. doi: <https://doi.org/10.1016/j.physrep.2004.08.031>. URL:  
 1887 <https://www.sciencedirect.com/science/article/pii/S0370157304003515>.
- 1888 [4] Gianfranco Bertone and Dan Hooper. “History of dark matter”. In: *Rev. Mod. Phys.*  
 1889 90 (4 Aug. 2018), p. 045002. doi: [10.1103/RevModPhys.90.045002](https://doi.org/10.1103/RevModPhys.90.045002). URL: <https://link.aps.org/doi/10.1103/RevModPhys.90.045002>.
- 1891 [5] Fritz Zwicky. “The Redshift of Extragalactic Nebulae”. In: *Helvetica Physica Acta* 6.  
 1892 (1933), pp. 110–127. doi: [10.5169/seals-110267](https://doi.org/10.5169/seals-110267).
- 1893 [6] Vera C. Rubin and Jr. Ford W. Kent. “Rotation of the Andromeda Nebula from a  
 1894 Spectroscopic Survey of Emission Regions”. In: *ApJ* 159 (Feb. 1970), p. 379. doi:  
 1895 [10.1086/150317](https://doi.org/10.1086/150317).
- 1896 [7] K. G. Begeman, A. H. Broeils, and R. H. Sanders. “Extended rotation curves of spiral galax-  
 1897 ies: dark haloes and modified dynamics”. In: *Monthly Notices of the Royal Astronomical So-*  
 1898 *ciety* 249.3 (Apr. 1991), pp. 523–537. ISSN: 0035-8711. doi: [10.1093/mnras/249.3.523](https://doi.org/10.1093/mnras/249.3.523).  
 1899 eprint: <https://academic.oup.com/mnras/article-pdf/249/3/523/18160929/mnras249-0523.pdf>. URL: <https://doi.org/10.1093/mnras/249.3.523>.
- 1901 [8] *Different types of gravitational lenses*. website. Feb. 2004. URL: <https://esahubble.org/images/heic0404b/>.
- 1903 [9] Douglas Clowe et al. “A Direct Empirical Proof of the Existence of Dark Matter”. In: *apjl*  
 1904 648.2 (Sept. 2006), pp. L109–L113. doi: [10.1086/508162](https://doi.org/10.1086/508162). arXiv: [astro-ph/0608407](https://arxiv.org/abs/astro-ph/0608407)  
 1905 [[astro-ph](https://arxiv.org/abs/astro-ph/0608407)].
- 1906 [10] Planck Collaboration and N. et. al. Aghanim. “Planck 2018 results I. Overview and the  
 1907 cosmological legacy of Planck”. In: *A&A* 641 (2020). doi: [10.1051/0004-6361/201833880](https://doi.org/10.1051/0004-6361/201833880). URL: <https://doi.org/10.1051/0004-6361/201833880>.
- 1909 [11] Wayne Hu. *Matter Density Animation*. web. 2024. URL: <http://background.uchicago.edu/~whu/animbut/anim2.html>.

- 1911 [12] Wenlong Yuan et al. “A First Look at Cepheids in a Type Ia Supernova Host with JWST”. in:  
1912     *The Astrophysical Journal Letters* 940.1 (Nov. 2022). doi: [10.3847/2041-8213/ac9b27](https://doi.org/10.3847/2041-8213/ac9b27).  
1913     URL: <https://dx.doi.org/10.3847/2041-8213/ac9b27>.
- 1914 [13] Wendy L. Freedman. “Measurements of the Hubble Constant: Tensions in Perspective”. In:  
1915     *The Astrophysical Journal* 919.1 (Sept. 2021), p. 16. doi: [10.3847/1538-4357/ac0e95](https://doi.org/10.3847/1538-4357/ac0e95).  
1916     URL: <https://dx.doi.org/10.3847/1538-4357/ac0e95>.
- 1917 [14] Jodi Cooley. “Dark Matter direct detection of classical WIMPs”. In: *SciPost Phys. Lect.*  
1918     *Notes* (2022), p. 55. doi: [10.21468/SciPostPhysLectNotes.55](https://doi.org/10.21468/SciPostPhysLectNotes.55). URL: <https://scipost.org/10.21468/SciPostPhysLectNotes.55>.
- 1920 [15] “Search for new phenomena in events with an energetic jet and missing transverse momentum  
1921     in  $pp$  collisions at  $\sqrt{s} = 13$  TeV with the ATLAS detector”. In: *Phys. Rev. D* 103  
1922     (11 July 2021), p. 112006. doi: [10.1103/PhysRevD.103.112006](https://doi.org/10.1103/PhysRevD.103.112006). URL: <https://link.aps.org/doi/10.1103/PhysRevD.103.112006>.
- 1924 [16] *Jetting into the dark side: a precision search for dark matter*. website. July 2020. URL:  
1925     <https://atlas.cern/updates/briefing/precision-search-dark-matter>.
- 1926 [17] Celine Armand et. al. “Combined dark matter searches towards dwarf spheroidal galaxies  
1927     with Fermi-LAT, HAWC, H.E.S.S., MAGIC, and VERITAS”. in: *Proceedings of Science*.  
1928     Vol. 395. Mar. 2022. doi: <https://doi.org/10.22323/1.395.0528>.
- 1929 [18] Tracy R. Slatyer. “Les Houches Lectures on Indirect Detection of Dark Matter”. In: *SciPost*  
1930     *Phys. Lect. Notes* (2022), p. 53. doi: [10.21468/SciPostPhysLectNotes.53](https://doi.org/10.21468/SciPostPhysLectNotes.53). URL:  
1931     <https://scipost.org/10.21468/SciPostPhysLectNotes.53>.
- 1932 [19] Christian W Bauer, Nicholas L. Rodd, and Bryan R. Webber. “Dark matter spectra from  
1933     the electroweak to the Planck scale”. In: *Journal of High Energy Physics* 2021.1029-8479  
1934     (June 2021). doi: [https://doi.org/10.1007/JHEP06\(2021\)121](https://doi.org/10.1007/JHEP06(2021)121).
- 1935 [20] Riccardo Catena and Piero Ullio. “A novel determination of the local dark matter density”.  
1936     In: *Journal of Cosmology and Astroparticle Physics* 2010.08 (Aug. 2010), p. 004. doi:  
1937     [10.1088/1475-7516/2010/08/004](https://doi.org/10.1088/1475-7516/2010/08/004). URL: <https://dx.doi.org/10.1088/1475-7516/2010/08/004>.
- 1939 [21] B. P. Abbott et al. “Observation of Gravitational Waves from a Binary Black Hole Merger”.  
1940     In: *Phys. Rev. Lett.* 116 (6 Feb. 2016), p. 061102. doi: [10.1103/PhysRevLett.116.061102](https://doi.org/10.1103/PhysRevLett.116.061102). URL: <https://link.aps.org/doi/10.1103/PhysRevLett.116.061102>.
- 1942 [22] R. Abbasi et. al. “Observation of high-energy neutrinos from the Galactic plane”. In: *Science*  
1943     380.6652 (June 2023), pp. 1338–1343.
- 1944 [23] NASA Goddard Space Flight Center. *Fermi’s 12-year view of the gamma-ray sky*. website.

- 1945 2022. URL: <https://svs.gsfc.nasa.gov/14090>.
- 1946 [24] Marco Cirelli et al. “PPPC 4 DM ID: a poor particle physicist cookbook for dark matter  
1947 indirect detection”. In: *Journal of Cosmology and Astroparticle Physics* 2011.03 (Mar.  
1948 2011), p. 051. doi: [10.1088/1475-7516/2011/03/051](https://doi.org/10.1088/1475-7516/2011/03/051). URL: <https://dx.doi.org/10.1088/1475-7516/2011/03/051>.
- 1950 [25] Javier Rico. “Gamma-Ray Dark Matter Searches in Milky Way Satellites—A Comparative  
1951 Review of Data Analysis Methods and Current Results”. In: *Galaxies* 8.1 (Mar. 2020), p. 25.  
1952 doi: [10.3390/galaxies8010025](https://doi.org/10.3390/galaxies8010025). arXiv: [2003.13482 \[astro-ph.HE\]](https://arxiv.org/abs/2003.13482).
- 1953 [26] W. B. Atwood et al. “The Large Area Telescope on the Fermi Gamma-Ray Space Telescope  
1954 Mission”. In: *apj* 697.2 (June 2009), pp. 1071–1102. doi: [10.1088/0004-637X/697/2/1071](https://doi.org/10.1088/0004-637X/697/2/1071). arXiv: [0902.1089 \[astro-ph.IM\]](https://arxiv.org/abs/0902.1089).
- 1956 [27] M. Ackermann et al. “Searching for Dark Matter Annihilation from Milky Way Dwarf  
1957 Spheroidal Galaxies with Six Years of Fermi Large Area Telescope Data”. In: *prl* 115.23,  
1958 231301 (Dec. 2015), p. 231301. doi: [10.1103/PhysRevLett.115.231301](https://doi.org/10.1103/PhysRevLett.115.231301). arXiv:  
1959 [1503.02641 \[astro-ph.HE\]](https://arxiv.org/abs/1503.02641).
- 1960 [28] Mattia Di Mauro, Martin Stref, and Francesca Calore. “Investigating the effect of Milky  
1961 Way dwarf spheroidal galaxies extension on dark matter searches with Fermi-LAT data”.  
1962 In: *Phys. Rev. D* 106 (12 Dec. 2022), p. 123032. doi: [10.1103/PhysRevD.106.123032](https://doi.org/10.1103/PhysRevD.106.123032).  
1963 URL: <https://link.aps.org/doi/10.1103/PhysRevD.106.123032>.
- 1964 [29] F. et al. Aharonian. “Observations of the Crab Nebula with H.E.S.S.”. In: *Astron. Astrophys.*  
1965 457 (2006), pp. 899–915. doi: [10.1051/0004-6361:20065351](https://doi.org/10.1051/0004-6361:20065351). arXiv: [astro-ph/0607333](https://arxiv.org/abs/astro-ph/0607333).
- 1967 [30] J. Albert et al. “VHE  $\gamma$ -Ray Observation of the Crab Nebula and its Pulsar with the MAGIC  
1968 Telescope”. In: *The Astrophysical Journal* 674.2 (Feb. 2008), p. 1037. doi: [10.1086/525270](https://doi.org/10.1086/525270). URL: <https://dx.doi.org/10.1086/525270>.
- 1970 [31] N. Park. “Performance of the VERITAS experiment”. In: *Proceedings, 34th International  
1971 Cosmic Ray Conference (ICRC2015): The Hague, The Netherlands, July, 30th July - 6th  
1972 August*. Vol. 34. 2015, p. 771. arXiv: [1508.07070 \[astro-ph.IM\]](https://arxiv.org/abs/1508.07070).
- 1973 [32] A. Abramowski et al. “H.E.S.S. constraints on Dark Matter annihilations towards the Sculptor  
1974 and Carina Dwarf Galaxies”. In: *Astropart. Phys.* 34 (2011), pp. 608–616. doi: [10.1016/j.astropartphys.2010.12.006](https://doi.org/10.1016/j.astropartphys.2010.12.006). arXiv: [1012.5602 \[astro-ph.HE\]](https://arxiv.org/abs/1012.5602).
- 1976 [33] A. Abramowski et al. “Search for dark matter annihilation signatures in H.E.S.S. observations  
1977 of Dwarf Spheroidal Galaxies”. In: *Phys. Rev. D* 90 (2014), p. 112012. doi: [10.1103/PhysRevD.90.112012](https://doi.org/10.1103/PhysRevD.90.112012). arXiv: [1410.2589 \[astro-ph.HE\]](https://arxiv.org/abs/1410.2589).

- 1979 [34] H. Abdalla et al. “Searches for gamma-ray lines and ‘pure WIMP’ spectra from Dark  
1980 Matter annihilations in dwarf galaxies with H.E.S.S”. in: *JCAP* 11 (2018), p. 037. doi:  
1981 [10.1088/1475-7516/2018/11/037](https://doi.org/10.1088/1475-7516/2018/11/037). arXiv: [1810.00995 \[astro-ph.HE\]](https://arxiv.org/abs/1810.00995).
- 1982 [35] J. Aleksić et al. “Optimized dark matter searches in deep observations of Segue 1 with  
1983 MAGIC”. in: *JCAP* 1402 (2014), p. 008. doi: [10.1088/1475-7516/2014/02/008](https://doi.org/10.1088/1475-7516/2014/02/008).  
1984 arXiv: [1312.1535 \[hep-ph\]](https://arxiv.org/abs/1312.1535).
- 1985 [36] V.A. Acciari et al. “Combined searches for dark matter in dwarf spheroidal galaxies observed  
1986 with the MAGIC telescopes, including new data from Coma Berenices and Draco”. In: *Physics of the Dark Universe* (2021), p. 100912. issn: 2212-6864. doi: <https://doi.org/10.1016/j.dark.2021.100912>. URL: <https://www.sciencedirect.com/science/article/pii/S2212686421001370>.
- 1990 [37] M. L. Ahnen et al. “Indirect dark matter searches in the dwarf satellite galaxy Ursa Major II  
1991 with the MAGIC Telescopes”. In: *JCAP* 1803.03 (2018), p. 009. doi: [10.1088/1475-7516/2018/03/009](https://doi.org/10.1088/1475-7516/2018/03/009). arXiv: [1712.03095 \[astro-ph.HE\]](https://arxiv.org/abs/1712.03095).
- 1993 [38] S. et al. Archambault. “Dark matter constraints from a joint analysis of dwarf Spheroidal  
1994 galaxy observations with VERITAS”. in: *prd* 95.8 (Apr. 2017). doi: [10.1103/PhysRevD.95.082001](https://doi.org/10.1103/PhysRevD.95.082001). arXiv: [1703.04937 \[astro-ph.HE\]](https://arxiv.org/abs/1703.04937).
- 1996 [39] Louise Oakes et al. “Combined Dark Matter searches towards dwarf spheroidal galaxies with  
1997 Fermi-LAT, HAWC, HESS, MAGIC and VERITAS”. in: *Proceedings of Science*. 2019.
- 1998 [40] Celine Armand et al. on behalf of the Fermi-LAT, HAWC, HESS, MAGIC, VERITAS.  
1999 “Combined Dark Matter searches towards dwarf spheroidal galaxies with Fermi-LAT,  
2000 HAWC, HESS, MAGIC and VERITAS”. in: *Proceedings of Science*. 2021.
- 2001 [41] Daniel Kerszberg et al. on behalf of the Fermi-LAT, HAWC, HESS, MAGIC, and VER-  
2002 TIAS collaborations. “Search for dark matter annihilation with a combined analysis of  
2003 dwarf spheroidal galaxies from Fermi-LAT, HAWC, H.E.S.S., MAGIC and VERITAS”. in:  
2004 *Proceedings of Science*. 2023.
- 2005 [42] A. U. Abeysekara et al. “Observation of the Crab Nebula with the HAWC Gamma-Ray  
2006 Observatory”. In: *The Astrophysical Journal* 843.1 (June 2017), p. 39. doi: [10.3847/1538-4357/aa7555](https://doi.org/10.3847/1538-4357/aa7555). URL: <https://doi.org/10.3847/1538-4357/aa7555>.
- 2008 [43] Giacomo Vianello et al. *The Multi-Mission Maximum Likelihood framework (3ML)*. 2015.  
2009 arXiv: [1507.08343 \[astro-ph.HE\]](https://arxiv.org/abs/1507.08343).
- 2010 [44] Marco Cirelli et al. “PPPC 4 DM ID: a poor particle physicist cookbook for dark matter  
2011 indirect detection”. In: *Journal of Cosmology and Astroparticle Physics* 2011.03 (Mar.  
2012 2011). issn: 1475-7516. doi: [10.1088/1475-7516/2011/03/051](https://doi.org/10.1088/1475-7516/2011/03/051). URL: <http://dx.doi.org/10.1088/1475-7516/2011/03/051>.

- 2014 [45] Alex Geringer-Sameth, Savvas M. Koushiappas, and Matthew Walker. “DWARF GALAXY  
2015 ANNIHILATION AND DECAY EMISSION PROFILES FOR DARK MATTER EXPERI-  
2016 MENTS”. in: *The Astrophysical Journal* 801.2 (Mar. 2015), p. 74. ISSN: 1538-4357. doi:  
2017 [10.1088/0004-637X/801/2/74](https://doi.org/10.1088/0004-637X/801/2/74). URL: <http://dx.doi.org/10.1088/0004-637X/801/2/74>.
- 2019 [46] A. Albert et al. “Dark Matter Limits from Dwarf Spheroidal Galaxies with the HAWC  
2020 Gamma-Ray Observatory”. In: *The Astrophysical Journal* 853.2 (Feb. 2018), p. 154. ISSN:  
2021 1538-4357. doi: [10.3847/1538-4357/aaa6d8](https://doi.org/10.3847/1538-4357/aaa6d8). URL: <http://dx.doi.org/10.3847/1538-4357/aaa6d8>.
- 2023 [47] V. Bonnivard et al. “Spherical Jeans analysis for dark matter indirect detection in dwarf  
2024 spheroidal galaxies - Impact of physical parameters and triaxiality”. In: *Mon. Not. Roy.  
2025 Astron. Soc.* 446 (2015), pp. 3002–3021. doi: [10.1093/mnras/stu2296](https://doi.org/10.1093/mnras/stu2296). arXiv:  
2026 [1407.7822 \[astro-ph.HE\]](https://arxiv.org/abs/1407.7822).
- 2027 [48] M. Ackermann et al. “Searching for Dark Matter Annihilation from Milky Way Dwarf  
2028 Spheroidal Galaxies with Six Years of Fermi Large Area Telescope Data”. In: *prl* 115.23,  
2029 231301 (Dec. 2015), p. 231301. doi: [10.1103/PhysRevLett.115.231301](https://doi.org/10.1103/PhysRevLett.115.231301). arXiv:  
2030 [1503.02641 \[astro-ph.HE\]](https://arxiv.org/abs/1503.02641).
- 2031 [49] M. L. Ahnen et al. “Limits to Dark Matter Annihilation Cross-Section from a Combined  
2032 Analysis of MAGIC and Fermi-LAT Observations of Dwarf Satellite Galaxies”. In: *JCAP*  
2033 1602.02 (2016), p. 039. doi: [10.1088/1475-7516/2016/02/039](https://doi.org/10.1088/1475-7516/2016/02/039). arXiv: [1601.06590](https://arxiv.org/abs/1601.06590)  
2034 [astro-ph.HE].
- 2035 [50] Javier Rico et al. *gLike: numerical maximization of heterogeneous joint  
2036 likelihood functions of a common free parameter plus nuisance parameters*.  
2037 <https://doi.org/10.5281/zenodo.4601451>. Version v0.09.03. Mar. 2021. doi: [10.5281/zenodo.4601451](https://doi.org/10.5281/zenodo.4601451). URL: <https://doi.org/10.5281/zenodo.4601451>.
- 2039 [51] Tjark Miener and Daniel Nieto. *LklCom: Combining likelihoods from different experiments*.  
2040 <https://doi.org/10.5281/zenodo.4597500>. Version v0.5.3. Mar. 2021. doi: [10.5281/zenodo.4597500](https://doi.org/10.5281/zenodo.4597500). URL: <https://doi.org/10.5281/zenodo.4597500>.
- 2042 [52] T. Miener et al. “Open-source Analysis Tools for Multi-instrument Dark Matter Searches”.  
2043 In: *arXiv e-prints*, arXiv:2112.01818 (Dec. 2021), arXiv:2112.01818. arXiv: [2112.01818](https://arxiv.org/abs/2112.01818)  
2044 [astro-ph.IM].
- 2045 [53] Alex Geringer-Sameth and Matthew Koushiappas Savvas M. and Walker. “Dwarf galaxy  
2046 annihilation and decay emission profiles for dark matter experiments”. In: *Astrophys.  
2047 J.* 801.2 (2015), p. 74. doi: [10.1088/0004-637X/801/2/74](https://doi.org/10.1088/0004-637X/801/2/74). arXiv: [1408.0002](https://arxiv.org/abs/1408.0002)  
2048 [astro-ph.CO].
- 2049 [54] Gianfranco Bertone, Dan Hooper, and Joseph Silk. “Particle dark matter: evidence, can-

- 2050 didates and constraints”. In: *Physics Reports* 405.5-6 (Jan. 2005), pp. 279–390. ISSN:  
2051 0370-1573. doi: [10.1016/j.physrep.2004.08.031](https://doi.org/10.1016/j.physrep.2004.08.031). URL: <http://dx.doi.org/10.1016/j.physrep.2004.08.031>.
- 2053 [55] V. Bonnivard et al. “Dark matter annihilation and decay in dwarf spheroidal galaxies: The  
2054 classical and ultrafaint dSphs”. In: *Mon. Not. Roy. Astron. Soc.* 453.1 (2015), pp. 849–867.  
2055 doi: [10.1093/mnras/stv1601](https://doi.org/10.1093/mnras/stv1601). arXiv: [1504.02048 \[astro-ph.HE\]](https://arxiv.org/abs/1504.02048).
- 2056 [56] A. et al. Albert. “Searching for Dark Matter Annihilation in Recently Discovered Milky Way  
2057 Satellites with Fermi-LAT”. in: *Astrophys. J.* 834.2 (2017), p. 110. doi: [10.3847/1538-4357/834/2/110](https://doi.org/10.3847/1538-4357/834/2/110). arXiv: [1611.03184 \[astro-ph.HE\]](https://arxiv.org/abs/1611.03184).
- 2059 [57] Mattia Di Mauro and Martin Wolfgang Winkler. “Multimessenger constraints on the dark  
2060 matter interpretation of the Fermi-LAT Galactic Center excess”. In: *prd* 103.12, 123005  
2061 (June 2021), p. 123005. doi: [10.1103/PhysRevD.103.123005](https://doi.org/10.1103/PhysRevD.103.123005). arXiv: [2101.11027 \[astro-ph.HE\]](https://arxiv.org/abs/2101.11027).
- 2063 [58] HongSheng Zhao. “Analytical models for galactic nuclei”. In: *Mon. Not. Roy. Astron. Soc.*  
2064 278 (1996), pp. 488–496. doi: [10.1093/mnras/278.2.488](https://doi.org/10.1093/mnras/278.2.488). arXiv: [astro-ph/9509122 \[astro-ph\]](https://arxiv.org/abs/astro-ph/9509122).
- 2066 [59] H. C. Plummer. “On the Problem of Distribution in Globular Star Clusters: (Plate 8.)”  
2067 In: *Monthly Notices of the Royal Astronomical Society* 71.5 (Mar. 1911), pp. 460–470.  
2068 ISSN: 0035-8711. doi: [10.1093/mnras/71.5.460](https://doi.org/10.1093/mnras/71.5.460). eprint: <https://academic.oup.com/mnras/article-pdf/71/5/460/2937497/mnras71-0460.pdf>. URL:  
2069 <https://doi.org/10.1093/mnras/71.5.460>.
- 2071 [60] Daniel R. Hunter. “Derivation of the anisotropy profile, constraints on the local velocity  
2072 dispersion, and implications for direct detection”. In: *JCAP* 02 (2014), p. 023. doi:  
2073 [10.1088/1475-7516/2014/02/023](https://doi.org/10.1088/1475-7516/2014/02/023). arXiv: [1311.0256 \[astro-ph.CO\]](https://arxiv.org/abs/1311.0256).
- 2074 [61] Barun Kumar Dhar and Liliya L. R. Williams. “Surface mass density of the Einasto family  
2075 of dark matter haloes: are they Sersic-like?” In: *Mon. Not. Roy. Astron. Soc.* (2010). doi:  
2076 [10.1111/j.1365-2966.2010.16446.x](https://doi.org/10.1111/j.1365-2966.2010.16446.x).
- 2077 [62] M. Baes and E. Van Hese. “Dynamical models with a general anisotropy profile”. In:  
2078 *Astron. Astrophys.* 471 (2007), p. 419. doi: [10.1051/0004-6361:20077672](https://doi.org/10.1051/0004-6361:20077672). arXiv:  
2079 [0705.4109 \[astro-ph\]](https://arxiv.org/abs/0705.4109).
- 2080 [63] Matthew G. Walker, Edward W. Olszewski, and Mario Mateo. “Bayesian analysis of re-  
2081 solved stellar spectra: application to MMT/Hectochelle observations of the Draco dwarf  
2082 spheroidal”. In: *mnras* 448.3 (Apr. 2015), pp. 2717–2732. doi: [10.1093/mnras/stv099](https://doi.org/10.1093/mnras/stv099).  
2083 arXiv: [1503.02589 \[astro-ph.GA\]](https://arxiv.org/abs/1503.02589).
- 2084 [64] Nicholas L. Rodd et al. “Dark matter spectra from the electroweak to the Planck scale”. In:

- 2085            *J. High Energy Physics* 121.10.1007 (June 2021).
- 2086 [65] Pace, Andrew B and Strigari, Louis E. “Scaling relations for dark matter annihilation and  
2087 decay profiles in dwarf spheroidal galaxies”. In: *Monthly Notices of the Royal Astronomical  
2088 Society* 482.3 (Oct. 2018), pp. 3480–3496. ISSN: 0035-8711. doi: [10.1093/mnras/sty2839](https://doi.org/10.1093/mnras/sty2839).
- 2090 [66] Albert, A. et al. “Search for gamma-ray spectral lines from dark matter annihilation in  
2091 dwarf galaxies with the High-Altitude Water Cherenkov observatory”. In: *Phys. Rev. D* 101 (10 May 2020), p. 103001. doi: [10.1103/PhysRevD.101.103001](https://doi.org/10.1103/PhysRevD.101.103001). URL:  
2093 <https://link.aps.org/doi/10.1103/PhysRevD.101.103001>.
- 2094 [67] Victor Eijkhout and Edmund Show and Robert van de Geijn. *The Science of Computing.  
2095 The Art of High Performance Computing*. Vol. 3. Open Copy published under CC-BY 4.0  
2096 license, 2023, pp. 63–66.
- 2097 [68] Qinrui Liu and Jeffrey Lazar and Carlos A. Argüelles and Ali Kheirandish. “ $\chi$ aro: a tool  
2098 for neutrino flux generation from WIMPs”. In: *Journal of Cosmology and Astroparticle  
2099 Physics* 2020.10 (Oct. 2020), p. 043. doi: [10.1088/1475-7516/2020/10/043](https://doi.org/10.1088/1475-7516/2020/10/043). URL:  
2100 <https://dx.doi.org/10.1088/1475-7516/2020/10/043>.